

ALL-ORDER POLARIZATION MODE DISPERSION COMPENSATION

A Dissertation

Submitted to the Faculty

of

Purdue University

by

Houxun Miao

In Partial Fulfillment of the

Requirements for the Degree

of

Doctor of Philosophy

August 2008

Purdue University

West Lafayette, Indiana

I dedicate this thesis to my wife, Yanzhu Lin and our whole family.

ACKNOWLEDGMENTS

Prof. A. M. Weiner for his guidance, support and encouragement...

Dr. D. E. Leaird for the special lab issues...

All my lab mates who have helped me in many ways throughout my Ph. D. study...

TABLE OF CONTENTS

	Page
LIST OF FIGURES.....	vi
LIST OF ABBREVIATIONS	xii
ABSTRACT.....	xiii
1. INTRODUCTION.....	1
2. POLARIZATION AND PMD	4
2.1 Polarization.....	4
2.2 PMD Fundamentals	6
2.3 PMD Measurement Techniques.....	8
2.4 PMD Mitigation.....	10
3. PMD COMPENSATION BASED ON THE PREVIOUS IDEA	22
3.1 Previous PMD Compensation Idea and Results	22
3.2 PMD Vectors, Output SOP and Common Spectral Phase.....	24
3.3 Ultralow-Power SHG FROG for Characterization of All-Order PMD Distorted Femtosecond Waveforms.....	25
3.4 Polarization Insensitive Ultralow-Power SHG FROG.....	28
3.5 All-Order PMD Compensation with Polarization Insensitive SHG FROG.....	30
4. ALL-ORDER PMD COMPENSATION VIA WAVELENGTH-PARALLEL JONES MATRIX SENSING AND CORRECTION.....	55
4.1 All-Order PMD Compensation Idea	55
4.2 Numerical Simulations of the New All-Order PMD Compensation Idea.....	56
4.3 Broadband All-Order PMD Compensation Experiments with a Specified Input SOP	58
4.4 Broadband All-Order PMD Compensation Experiments with an Arbitrary Input SOP	59

	Page
5. ALL-ORDER PMD COMPENSATION VIA A VIPA BASED PULSE SHAPER.....	85
6. SUMMARY AND FUTURE DIRECTIONS.....	96
LIST OF REFERENCES.....	97
VITA.....	102

LIST OF FIGURES

Figure	Page
2.1 Poincarè Sphere (adapted from [30]).....	12
2.2 a) Internal and b) External perturbations (adapted from [1]).....	13
2.3 Polarization evolution in a fiber (adapted from [1])	14
2.4 DGD for a short section of fiber (adapted from [1]).....	15
2.5 Polarization mode coupling	16
2.6 Jones matrix characterization (adapted from [31])	17
2.7 PMD Vector measurement results using MMM method (adapted from [13])	18
2.8 Fiber PMD coefficient vs year of installation (adapted from[30])	19
2.9 PMD limited reach vs fiber PMD-coefficient (adapted from [30])	20
2.10 Diagram for PMD vector compensation (adapted from [33]).....	21
3.1 Ultrafast pulse shaping apparatus (adapted from [18]).....	32
3.2 SOP correction setup (adapted from [20]).....	33
3.3 SOP correction algorithm (adapted from [33]).....	34
3.4 Wavelength-parallel polarimeter (adapted from [19]).....	35
3.5 SOP correction examples (adapted from [16])	36
3.6 PMD compensation setup (adapted from [33]).....	37
3.7 Iterated Gerchberg-Saxton algorithm for spectral phase correction	38
3.8 PMD compensation examples (adapted from [16]).....	39

Figure	Page
3.9 Schematic diagram of SHG FROG using an A-PPLN waveguide. MI: Michelson interferometer. OSA: optical spectrum analyzer. I-CCD: Intensified CCD camera (adapted from [42])	40
3.10 FROG data of nearly bandwidth-limited pulses with free-space-coupled A-PPLN. (A) Measured, and (B) retrieved FROG traces at 9.5 fJ. (C) Measured , and (D) retrieved FROG traces at 124 aJ. Retrieved pulse illustrated in: (E) frequency domain, and (F) time domain for both 9.5-fJ and 124-aJ coupled pulse energies. Dotted curve in (E) represents the independently measured power spectrum (adapted from [42])	41
3.11 FROG data for bandwidth-limited optical pulses with a fiber-pigtailed A-PPLN. (A) Measured FROG trace. (B) Retrieved FROG trace. (C) Retrieved spectral intensity (solid) and phase (dashed) profiles together with the spectrum recorded by OSA (dotted). (D) Retrieved temporal intensity profile.....	42
3.12 Experimental setup for sensing and compensation of PMD induced pulse distortion at selected polarization slices controlled via SHG FROG. PC: polarization Controller	43
3.13 FROG data of chromatic dispersion and all-order PMD distorted pulses at a selected polarization slice. (A) Measured FROG trace. (B) Retrieved FROG trace. (C) Retrieved spectral intensity (solid) and phase (dashed) profiles. (D) Retrieved temporal intensity profile.....	44
3.14 FROG data after spectral phase correction. (A) Measured FROG trace. (B) Retrieved FROG trace. (C) Retrieved spectral intensity (solid) and phase (dashed) profiles. (D) Retrieved temporal intensity profile	45
3.15 Temporal intensity profiles of the distorted (A) and restored (B) pulses.....	46
3.16 Polarization insensitive ultralow-power SHG FROG setup	47
3.17 FROG data with time-varying polarization fluctuations intentionally introduced, and scrambler off. (A) Measured FROG trace. (B) Retrieved FROG trace. (C) Retrieved spectral intensity and phase profiles. (D) Retrieved temporal intensity profile. Dashed line (in C): spectral phase profile; dotted line (in C): spectrum recorded by OSA.....	48

Figure	Page
3.18 FROG data with time-varying polarization fluctuations intentionally introduced, and scrambler on. (A) Measured FROG trace. (B) Retrieved FROG trace. (C) Retrieved spectral intensity and phase profiles. (D) Retrieved temporal intensity profile. Dashed line (in C): spectral phase profile; dotted line (in C): spectrum recorded by OSA.....	49
3.19 Experimental setup for all-order PMD compensation	50
3.20 Spectra before (A) and after (B) SOP correction. Solid: with PMD; dotted: without PMD.....	51
3.21 FROG data of optical pulses after SOP correction but before spectral phase correction. (A) Measured FROG trace. (B) Retrieved FROG trace. (C) Retrieved spectral intensity (solid) and phase (dashed) profiles. (D) Retrieved temporal intensity profile	52
3.22 FROG data of optical pulses after SOP and spectral phase correction. (A) Measured FROG trace. (B) Retrieved FROG trace. (C) Retrieved spectral intensity (solid) and phase (dashed) profiles. (D) Retrieved temporary intensity profile	53
3.23 Pulses before (A) and after (B) spectral phase correction.....	54
4.1 Scheme for numerical simulations of all-order PMD compensation.....	63
4.2 Output SOPs corresponding to 0° (left) and 45° (right) linear input SOPs. Curves connected with red lines are calculated SOPs and curves connected with black lines are SOPs with random Gaussian noise	64
4.3 Left: initial (blue), PMD distorted (black) and the restored after PMD compensation (red) optical pulses. Right: the wavelength dependent DGD profile.....	65
4.4 Left: initial (blue), PMD distorted (black) and the restored after PMD compensation (red) optical pulses. Right: the wavelength dependent DGD profile.....	66
4.5 Left: initial (blue), PMD distorted (black) and the restored after PMD compensation (red) optical pulses. Right: the wavelength dependent DGD profile.....	67

Figure	Page
4.6 Output SOPs corresponding to 0° (left) and 45° (right) linear input SOPs. Curves connected with red lines are calculated SOPs and curves connected with black lines are SOPs with random Gaussian noise	68
4.7 Left: initial (blue), PMD distorted (black) and the restored after PMD compensation (red) optical pulses. Right: the wavelength dependent DGD profile.....	69
4.8 Left: initial (blue), PMD distorted (black) and the restored after PMD compensation (red) optical pulses. Right: the wavelength dependent DGD profile.....	70
4.9 Left: initial (blue), PMD distorted (black) and the restored after PMD compensation (red) optical pulses. Right: the wavelength dependent DGD profile.....	71
4.10 Experimental setup for broadband all-order PMD compensation with a specified input SOP. PC: polarization controller; FLC: ferroelectric liquid crystal; NPBS: non-polarizing beam splitter; LCM: liquid crystal modulator	72
4.11 (A) Output SOP spectrum for horizontally linear input SOP; (B) output SOP spectrum for RHC input. Each point corresponds to a measured SOP vector at a specified wavelength. Solid lines are used to connect SOP vectors at adjacent wavelength.....	73
4.12 (A) Distorted pulses measured at orthogonal polarization states. (B) Restored pulses after PMD compensation	74
4.13 Restored pulse (corresponding to Fig. 4. 12. (B)) measured via polarization insensitive cross-correlation while keeping the input SOP switching	75
4.14 Left Column: distorted pulses measured at orthogonal polarization states. Right column: Restored pulses after PMD compensation	76
4.15 Left Column: distorted pulses measured at orthogonal polarization states. Right column: Restored pulses after PMD compensation	77
4.16 Experimental setup for all-order PMD compensation with an arbitrary input SOP. PC: polarization controller, FLC: ferroelectric liquid crystal, NPBS: non-polarizing beam splitter, LCM: liquid crystal modulator	78

Figure	Page
4.17 Output SOP spectra corresponding to the 4 FLC states 00, 01, 10 and 11. Each point corresponds to a measured SOP vector at a specified wavelength, SOP vectors at adjacent wavelength are connected via solid lines.....	79
4.18 (A) and (B) Distorted and restored pulses when 00-01 states are selected for PMD compensation process. (C) and (D) Distorted and restored pulses when 10-11 states are selected for PMD compensation process	80
4.19 Distorted and restored pulses	81
4.20 Left Column: distorted pulses measured at orthogonal polarization states. Right column: Restored pulses after PMD compensation	82
4.21 Left Column: distorted pulses measured at orthogonal polarization states. Right column: Restored pulses after PMD compensation	83
4.22 Restored pulses corresponding to Fig. 4.18 (B) and Fig. 4.19 (B), measured with polarization insensitive cross correlation while the FLC retarders kept switching.....	84
5.1 Experimental setup for PMD compensation via a VIPA based pulse shaper. PC: polarization controller; FLC: ferroelectric liquid crystal; VIPA: virtually imaged phased-array; LCM: liquid crystal modulator. The polarimeter consists of a pair of FLC retarders, a polarizer and a 256-pixel linear InGaAs detector array. The block arrows indicate the direction of the signal flow	88
5.2 Output SOP spectra corresponding to the 4 FLC states: 00, 01, 10, 11. Each point corresponds to a measured SOP vector at a specified pixel of the detector array (corresponding to a wavelength component)	89
5.3 PMD compensation results. (A) Distorted pulse; (B) restored and initial pulses.....	90
5.4 PMD compensation result with 10-11 FLC states selected	91
5.5 Distorted (A) and restored pulses (B)	92
5.6 Left Column: distorted pulses. Right column: Restored pulses after PMD compensation	93
5.7 Left Column: distorted pulses. Right column: Restored pulses after PMD compensation	94

Figure	Page
5.8 Persistent traces of the initial pulse (A), PMD distorted pulse with the FLC retarders switching at a rate of 20 Hz (B), distorted pulse with the FLC retarders switching at 2 kHz (C) and the restored pulse with the FLC retarders switching at 2 kHz (D).....	95

LIST OF ABBREVIATIONS

A-PPLN	Aperiodically Poled Lithium Niobate
DCF	Dispersion Compensating Fiber
DGD	Differential Group Delay
FH	Fundamental Harmonic
FLC	Ferroelectric Liquid Crystal
FROG	Frequency-Resolved Optical Gating
FSR	Free Spectral Range
FWHM	Full Width at Half Maximum
JME	Jones Matrix Eigenanalysis
LCM	Liquid Crystal Modulator
LHC	Left Hand Circular
MMM	Muller Matrix Method
OSA	Optical Spectrum Analyzer
PC	Polarization Controller
PDG	Polarization Dependent Gain
PDL	Polarization Dependent Loss
PM	Polarization Maintaining
PMD	Polarization Mode Dispersion
PSP	Principle State of Polarization
QPM	Quasi-Phase Matched
RHC	Right Hand Circular
RPE	Reverse-Proton-Exchanged
SHG	Second Harmonic Generation
SLM	Spatial Light Modulator
SMF	Single Mode Fiber
SOP	State of Polarization
SPIDER	Spectral Phase Interferometry for Direct Electric-field Reconstruction
VIPA	Virtual-Imaged Phased Array

ABSTRACT

Miao, Houxun. Ph.D., Purdue University, August 2008. All-Order Polarization Mode Dispersion Compensation. Major Professor: Andrew M. Weiner.

Polarization mode dispersion (PMD) is one of the key factors limiting the upgrade of current optical fiber communication systems. Traditional PMD compensators typically work in the low-order PMD approximation. However, as the bandwidth of telecommunication systems increases, all-order PMD effects become increasingly important. In previous work, our group proposed and experimentally demonstrated all-order PMD compensation by sensing and compensating the PMD induced SOP distortion first and then measuring and correcting the resulted spectral phase. Due to the limit of the spectral phase measurement technique, we can not achieve full compensation for some PMD profiles.

In this work, we first improve the previous PMD compensation system with an advanced optical pulse measurement technique – frequency-resolved optical gating. Then we propose a new and much more robust PMD compensation idea, which is based on wavelength-parallel sensing and correction of the frequency dependent Jones matrix of a fiber link. We experimentally demonstrate all-order PMD compensation of subpicosecond optical pulses distorted by a PMD module with an estimated mean differential group delay (DGD) of ~ 5.5 ps with grating-based wavelength-parallel polarimeter and transmission pulse shaper. The PMD compensation system is suitable for PMD compensation of future Tb/s telecommunication systems. We scale the all-order PMD compensation concept to the optical bandwidth consistent with near-term lightwave communications rates by using virtually-imaged phased array based wavelength-parallel polarimeter and transmission pulse shaper, where we demonstrate all-order PMD compensation of ~ 15 ps optical pulses distorted by all-order PMD with mean DGD of ~ 42 ps.

1. INTRODUCTION

As the bit rates and distance continue to increase, polarization mode dispersion (PMD) has emerged as a key factor limiting high-speed transmission in optical fiber links [1, 2]. Great efforts have been made to understand, measure, emulate and compensate PMD effects since late 1980's [3-14]. Currently, there are several mature PMD measurement techniques such as fixed analyzer method, Jones matrix eigenanalysis (JME) method [12] and Muller matrix method (MMM) [13]. However, most of the PMD compensation efforts have been limited to low-order (first- and second-order) approximation, which is only valid for narrow-bandwidth operation [2]. Phua et. al., proposed an all-order PMD compensation scheme based on the correction of the frequency dependent PMD vectors with the assumption of precisely known information of PMD vectors [15]. However, accurate characterization of frequency dependent PMD vectors itself remains a challenge. As a result, no experiment has been carried out based on this idea. Up to now, there is still no all-order PMD compensation technique available for real application.

In the previous work of our group, M. Akbulut experimentally demonstrated for the first time broadband all-order PMD compensation [16, 17] by applying pulse shaping techniques [18]. PMD effects were treated as arbitrary variations of states of polarization (SOPs) and spectral phase versus wavelength. Two pulse shapers were implemented in a serial manner to compensate for the polarization and the phase spectra independently. The distorted SOP spectrum was first measured by a home-made wavelength-parallel polarimeter [19] and corrected to a fixed single polarization state with a specially designed SOP pulse shaper [20]. Then the spectral phase of the resulted single polarization spectrum was measured and corrected via a phase only pulse shaper. The spectral phase was obtained by measuring the temporal intensity via cross-correlation, the spectrum via optical spectrum analyzer (OSA) and then applying Gerchberg-Saxton algorithm. However, due to the complexity of the all-order PMD induced pulse distortion and due the limits of the Gerchberg-Saxton algorithm, an iterative measure-compensate-measure procedure was necessary, which lacked the robustness that will be needed for

real applications. Furthermore, for some PMD profiles, even after several measure-compensate-measure iterations, clean pulses were still not achievable.

In this work, we first introduce ultralow-power second harmonic generation (SHG) frequency-resolved optical gating (FROG) technique [21-24] to improve the measurement of the PMD induced spectral phase, which eventually improves the performance of the previous PMD compensation system. We then notice that the old PMD compensation idea itself has several drawbacks. Firstly, the phase measurement takes several minutes and the measurement accuracy depends strongly on the complexity of the distorted pulses, which lacked the robustness that will be needed for real application. Secondly, the compensation is dependent on the input SOP, which means that fluctuations of the input SOP will result in pulse distortion after the compensator is set, even the system PMD remains the same.

Motivated by creating a much more robust PMD compensation system, we propose a completely new PMD compensation idea, which is based on wavelength-parallel sensing and correction of the frequency dependent Jones matrix of the fiber link. Instead of studying the PMD vectors of a fiber link, we directly study the frequency dependent Jones matrix, which consists of more information than PMD vectors. For Jones matrix sensing, we propose a method to characterize the frequency dependence of the Jones matrix with an arbitrary input SOP. For Jones matrix correction, we disclose an algorithm to decompose the inverse of the PMD-related Jones matrix to the product of three elementary rotation matrices, which can be applied via a transmission pulse shaper employing a four-layer liquid crystal modulator (LCM) array.

We experimentally demonstrated all-order PMD compensation of subpicosecond optical pulses distorted by a PMD module with an estimated mean differential group delay (DGD) of ~ 5.5 ps with grating-based broadband wavelength-parallel polarimeter and transmission pulse shaper [25]. The PMD compensation system is ideally suitable for PMD compensation of future Tb/s telecommunication systems. We scaled our all-order PMD compensation concept to the optical bandwidth consistent with near-term lightwave communications rates by using a virtually-imaged phase array (VIPA) [26-27] based wavelength-parallel polarimeter and transmission pulse shaper, where we demonstrated all-order PMD compensation of ~ 15 ps optical pulses distorted by all-order PMD with mean DGD of ~ 42 ps [28].

The thesis is organized as follows: Chapter 2 covers the fundamentals of PMD, PMD measurement techniques and some traditional PMD compensation methods. Chapter 3 includes the previous PMD compensation work and the improved PMD

compensation results with SHG FROG. Chapter 4 describes the new PMD compensation idea, experimental setup and results for broadband all-order PMD compensation with grating-based wavelength-parallel polarimeter and pulse shaper. Chapter 5 reports PMD compensation work with VIPA-based wavelength-parallel polarimeter and pulse shaper. Finally, Chapter 6 gives suggestions on future directions for the PMD compensation team.

2. POLARIZATION AND PMD

This chapter is dedicated to clarify the fundamental concepts of polarization and PMD. It is simplified summaries of many papers and book chapters.

2.1 Polarization

Polarization of a monochromatic light represents the oscillation direction of its electric field. There are several different presentations of polarization. Here we only introduce the two most popular ones, Jones vector and Stokes vector in the Jones space [29] and the Stokes space [30].

For a beam propagating in the $+z$ direction, at any point z , the electric field lies in the x - y plane, and can be written in terms of its horizontal x and orthogonal y components in the Jones space.

$$\bar{E} = (\hat{x}E_x e^{j\phi_x} + \hat{y}E_y e^{j\phi_y}) e^{j(\omega_0 t - \beta z)}, \quad (2.1)$$

where \hat{x} and \hat{y} are unit vectors in x and y directions; E_x , ϕ_x and E_y , ϕ_y are the magnitudes and phases of the x and y components; ω_0 is the angular carrier frequency and β is the propagation constant. Eq. (2.1) can be written in vector form as:

$$\bar{E} = e|s\rangle e^{j(\omega_0 t - \beta z)}, \quad (2.2)$$

where e is the complex electric field and $|s\rangle = \begin{bmatrix} s_x \\ s_y \end{bmatrix}$, satisfying $\langle s|s\rangle = s_x^* s_x + s_y^* s_y = 1$. $|s\rangle$

is called the complex 2-D Jones ket vector.

In the Jones space, a polarization device is represented by a 2x2 Jones matrix ($J = e^{i\varphi}U$, where φ is common phase). The transformation of the input SOP (s) to the output SOP (t) is described as:

$$|t\rangle = U|s\rangle. \quad (2.3)$$

For example, the Jones matrix of a horizontally oriented polarizer is $\begin{bmatrix} 1 & 0 \\ 0 & 0 \end{bmatrix}$. The Jones matrix of a lossless medium can be written in the Cayley/Klein form [5]:

$$U = \begin{bmatrix} \alpha & \beta \\ -\beta^* & \alpha^* \end{bmatrix}, \quad (2.4)$$

where, $\alpha\alpha^* + \beta\beta^* = 1$.

In the Stokes space, the SOP is described by a 4x1 vector:

$$\mathbf{S} = \begin{bmatrix} S_0 \\ S_1 \\ S_2 \\ S_3 \end{bmatrix}, \quad (2.5)$$

where, S_0 is the total power, S_1 is the power difference between 0° linear and 90° linear polarization states, S_2 is the power difference between 45° linear and 135° linear states and S_3 is the power difference between right hand circular (RHC) and left hand circular (LHC) states. In parallel with the Jones space, a polarization component is represented by a 4x4 Muller matrix (M). And the output SOP is related to the input SOP as:

$$\mathbf{T} = M\mathbf{S}. \quad (2.6)$$

For a completely polarized light, $S_1^2 + S_2^2 + S_3^2 = S_0^2$. The Stokes vector can be simplified to a 3x1 vector, by dividing the four Stokes component in Eq. (2.5) by S_0 and taking the last 3 components (the first component is always 1):

$$\hat{\mathbf{s}} = \begin{bmatrix} s_1 \\ s_2 \\ s_3 \end{bmatrix}. \quad (2.7)$$

Since for fully polarized light, $s_1^2 + s_2^2 + s_3^2 = 1$, the 3-D Stokes vector enables graphical visualization of SOP on a spherical surface (Fig. 2.1). The surface is called Poincare Sphere. Linear polarizations lie on the equator, right hand elliptical polarization on the lower hemisphere, and left hand elliptical polarization on the upper hemisphere, with circularly polarized lights on the poles.

The Muller matrix of a lossless medium can be written as a 3x3 rotation matrix R satisfying $R^T R = I$. For example, the Muller matrix of a linear retarder oriented along the x

axis is
$$\begin{bmatrix} 1 & 0 & 0 \\ 0 & \cos \varphi & -\sin \varphi \\ 0 & \sin \varphi & \cos \varphi \end{bmatrix}.$$

The Pauli spin vector is used to connect the Jones space with the Stokes space.

The Pauli spin vector is defined as,

$$\vec{\sigma} = [\sigma_1 \quad \sigma_2 \quad \sigma_3], \quad (2.8)$$

where, $\sigma_1 = \begin{bmatrix} 1 & 0 \\ 0 & -1 \end{bmatrix}$, $\sigma_2 = \begin{bmatrix} 0 & 1 \\ 1 & 0 \end{bmatrix}$, $\sigma_3 = \begin{bmatrix} 0 & -j \\ j & 0 \end{bmatrix}$. For polarized light, the Stokes vector is related to the Jones vector by,

$$\hat{s} = \langle s | \vec{\sigma} | s \rangle. \quad (2.9)$$

For a lossless medium, the Muller matrix is connected with the Jones matrix by,

$$R\vec{\sigma} = U^\dagger \vec{\sigma} U. \quad (2.10)$$

2.2 PMD Fundamentals

PMD arises from the optical birefringence in optical fibers due to the asymmetries in the fiber core [1, 2]. Theoretically, in a single mode fiber (SMF) with an ideal circular symmetry, the group velocities of the two orthogonal modes are the same. In reality, there is always some amount of birefringence in the fiber due to imperfections in the manufacturing process and/or mechanical stress on the fiber after manufacture (as shown in Fig. 2.2), resulting in different group delays of the two orthogonal modes. The following analysis will be under lossless linearly birefringence assumption, which is valid for SMF.

For a short section of SMF, the birefringence can be considered constant. The amount of birefringence can be described by the difference between the slow and fast modes:

$$\Delta\beta = \frac{\omega n_s}{c} - \frac{\omega n_f}{c} = \frac{\omega \Delta n}{c}, \quad (2.11)$$

where c is the speed of light and $\Delta n = n_s - n_f$ is the differential effective refractive index between the slow and fast modes. When an input light not aligned to the birefringence axes is launched into a short fiber, the light goes through a variety of polarization states along the length of the fiber, returning to the original input state after a characteristic ‘‘Beat Length’’ (Fig 2.3). The beat length is given by:

$$L_b = \frac{\lambda}{\Delta n}. \quad (2.12)$$

In the time domain, for a short section of fiber, the DGD, $\Delta\tau$, is defined as the group-delay difference between the slow and fast mode (Fig. 2.4). The DGD can be found from the frequency derivative of the birefringence:

$$\frac{\Delta\tau}{L} = \frac{d}{d\omega}(\Delta\beta) = \frac{\Delta n}{c} - \frac{\omega}{c} \frac{d\Delta n}{d\omega}. \quad (2.13)$$

Normally the second term in the above equation is 0 because the dispersion of Δn can be ignored. The DGD of a short section of fiber is linearly dependent on the fiber length.

In the long fiber regime, the birefringent axes are randomly oriented along the fiber length, causing polarization-mode coupling: the slow and fast polarization modes from one segment each decompose into both the slow and fast modes of the next segment (Fig. 2.5). Due to the mode coupling, the birefringence of each section may either add to or subtract from the total birefringence, and therefore, the DGD does not accumulate linearly with the fiber length. Experiments show that the mean DGD of a long fiber increases linearly with the square root of the fiber length.

Due to the random polarization mode coupling, the propagation of a pulse through a long-length fiber is extremely complicated. However, in the case of narrow bandwidth input signal, even for long fibers, one can still find two special orthogonal polarization states at the fiber input that result in an output pulse undistorted to the first order. These two orthogonal SOPs are called principle states of polarization (PSPs). In the frequency domain, a PSP is defined as that input polarization for which the output SOP is independent of frequency to the first order, i. e., over a small frequency range. With the definition of DGD and PSP, PMD can be characterized by a 3x1 vector:

$$\vec{\tau} = \Delta\tau\hat{p}, \quad (2.14)$$

where \hat{p} is a unit vector in the Stokes space and points in the direction of the slow PSP. The detailed mathematical definition of PMD will be given in the section of PMD measurement techniques.

The most important features of PMD are that PMD of long SMFs is time stochastic and frequency dependent. Since the birefringence of a fiber changes as environment changes (temperature, stress and so on), the resulted PMD vector changes temporally. Experiments show that the DGD follows a Maxwellian distribution as:

$$p_{\Delta\tau}(x) = \frac{8}{\pi^2\tau} \left(\frac{2x}{\tau}\right)^2 e^{-(2x/\tau)^2/\pi}; x \geq 0, \quad (2.15)$$

where τ is the mean DGD. Also, both the DGD and the PSP vary with frequency quickly. The polarization-mode coupling results in the frequency dependent feature of PMD, which is traditionally categorized in a Taylor series framework in terms of first-order PMD, second-order PMD, etc. However, in our work, we do not use this all-order PMD model. We treat the PMD effects as frequency dependent polarization rotations and delays in our previous PMD compensation idea and as frequency dependent Jones matrix in the new PMD compensation concept.

2.3 PMD Measurement Techniques

Numerous methods have been proposed for the measurement of PMD. Some methods (for example: optical time-domain reflectometry method) operate in the time domain by sensing the pulse delay, whereas others operate in the frequency domain by detecting changes of polarization with frequency (such as Poincaré sphere arc method, JME and MMM). The JME and MMM are now two mature PMD measurement techniques that allow measurement of the instantaneous PMD vectors as a function of frequency.

Poincaré Sphere Arc Method

Poincaré sphere arc method is one of the most popular PMD sensing technologies. Here we show that it is unreliable to estimate PMD from a single SOP string.

Provided that the input SOP is frequency independent, the basis equation for Poincaré arc method is written as,

$$\hat{s}_\omega = \vec{\tau} \times \hat{s}, \quad (2.16)$$

where \hat{s} is the output SOP, $\vec{\tau}$ is the PMD vector of the fiber link, subscript ω indicates differentiation. The information given by Eq. (2.16) is that, $\vec{\tau}$ is in the plane perpendicular to \hat{s}_ω and $|\vec{\tau}| \sin \alpha = |\hat{s}_\omega|$, where α is the angle between $\vec{\tau}$ and \hat{s} .

By performing differential operation to both sides of Eq. (2.16), one gets,

$$\hat{s}_{\omega\omega} = \vec{\tau}_\omega \times \hat{s} + \vec{\tau} \times \hat{s}_\omega. \quad (2.17)$$

From Eqs. (2.16) and (2.17), one gets,

$$\vec{\tau} = (\hat{s}_\omega \times \hat{s}_{\omega\omega}) / \hat{s}_\omega^2 + \hat{s} (\vec{\tau}_\omega \cdot \hat{s}_\omega) / \hat{s}_\omega^2 = \vec{\Omega} - \hat{s} (\vec{\tau} \cdot \hat{s}_{\omega\omega}) / \hat{s}_\omega^2. \quad (2.18)$$

In traditional Poincaré arc method, $\vec{\tau}_\omega$ is assumed to be small enough and $\vec{\Omega}$ is used to approach $\vec{\tau}$. However, this approximation is not valid when all-order PMD effects must be taken into account.

Jones Matrix Eigenanalysis (JME)

JME is first developed by Heffner in 1992 [11, 12]. PMD vector is related to the Jones matrix via:

$$\frac{1}{2} \begin{pmatrix} \tau_1 & \tau_2 - j\tau_3 \\ \tau_2 + j\tau_3 & -\tau_1 \end{pmatrix} = jU_\omega U^\dagger, \quad (2.19)$$

where, τ_1 , τ_2 and τ_3 are the 3 components of the PMD vector and U is the Jones matrix. The procedure for Jones matrix measurement [31] is shown in Fig. 2.6. By measuring the response ($\begin{bmatrix} X_1 \\ Y_1 \end{bmatrix}$, $\begin{bmatrix} X_2 \\ Y_2 \end{bmatrix}$, $\begin{bmatrix} X_3 \\ Y_3 \end{bmatrix}$ in Fig. 2.6 are the output Jones vectors) of the device under test to the three known input SOPs, the coefficients of the Jones Matrix can be calculated for each frequency except a constant. This constant is not related to polarization transformation and PMD calculations, and is usually ignored. By writing the Jones matrix in the form of (for a single frequency):

$$T = \begin{bmatrix} a & b \\ c & d \end{bmatrix}, \quad (2.20)$$

one gets,

$$T = d \begin{bmatrix} k_1 k_4 & k_2 \\ k_4 & 1 \end{bmatrix}, \quad (2.21)$$

where,

$$k_1 = \frac{X_1}{Y_1} = \frac{a}{c}, \quad k_2 = \frac{X_2}{Y_2} = \frac{b}{d}, \quad k_3 = \frac{X_3}{Y_3} = \frac{a+b}{c+d}, \quad k_4 = \frac{c}{d} = \frac{k_3 - k_2}{k_1 - k_3} \quad (2.22)$$

For a lossless linear medium, $d=a^*$, $c=-b^*$, therefore the Jones matrix can simply be characterized by measuring the response of the device to two known input SOPs, such as 0° and 45° .

By scanning the wavelength of the input signal with some specified resolution and measuring the Jones matrix at each frequency, one can obtain the frequency dependent Jones matrix. Thus one can calculate the frequency dependent PMD vectors for a wide spectral range by using Eq. 2.19. Current available PMD vector measurement instruments based on JME normally use a tunable laser as the light source, use polarization controllers (PCs) to generate the known input SOPs and use a polarimeter for the output SOP measurement. The PMD measurement errors are typically less than 10% the mean DGD.

Müller Matrix Method (MMM)

MMM was developed [13] in 1999 by Jopson et. al. The PMD vector is related to the Muller matrix R via:

$$\vec{\tau} \times = R_\omega R^\dagger. \quad (2.23)$$

MMM algorithm requires the launch of two arbitrary SOPs with angle sufficiently close to 90° . The first linear input SOP s_I gives the output Stokes Vector t_I , and the second input SOP s_a results in t_a . The Muller matrix is calculated by:

$$R_{ij}^T = (t_i)_j, \quad (2.24)$$

where,

$$t_3 = k t_1 \times t_a, t_2 = t_3 \times t_1. \quad (2.25)$$

In Eq. 2. 24, $i=1, 2, 3; j=1, 2, 3$. The constant k is to make sure that t_3 remains unit vector. The PMD vector can be extracted from the Muller matrix by using Eq. 2. 23. Figure 2.7 shows an example of the measured PMD vectors vs. wavelength of a fiber with mean DGD of ~ 40 ps.

2.4 PMD Mitigation

The simplest and currently adopted way of reducing PMD impairment is to deploy fibers having very low PMD. Fig. 2.8 shows the different PMD coefficients of fibers installed at different time [32]. Typically, the PMD coefficient of today's fiber is <0.05 ps/km^{1/2}. Fig. 2.9 shows the PMD limited reach for different transmission systems [32]. From the figure, PMD impairments are significantly improved with low PMD fibers. Also, different modulation formats may be more or less sensitive to the pulse distortion caused by PMD.

PMD compensation techniques aim to reduce the PMD impairment in the fiber cable with high PMD. Numerous techniques have been proposed. Due to the time stochastic feature of PMD, PMD compensator normally consists of an adaptive counter-element, a feedback signal and a control algorithm. Here, we will summarize some of these compensators.

In a first kind of PMD compensator, the SOP of the input signal is aligned with the input PSP. A device monitors the signal at the output, and sends feedback to the input side to rotate the polarization until minimum PMD distortion is detected. This technique can only operate in a narrow bandwidth.

Another typical PMD compensator employs electronic equalization at the receiver. This method involves electrical delay lines and complicated algorithms. Since all the polarization information is lost after the optical-to-electrical conversion at the photodetector, this kind of method works in some case. But the algorithms may break down for high bit-rate WDM communication systems.

A third method is to null the PMD vector. A typical scheme is shown in Fig 2.10 [33]. The first PC aims to rotate the PSP of the fiber link to the PSP of the differential delay segment, and the differential delay element introduces the DGD that is opposite to the system DGD. To avoid the complexity of the PSP measurement, the system typically works with an adaptive feedback algorithm. Like PSP launching method, this kind of PMD compensator can only operate in the narrow bandwidth limit.

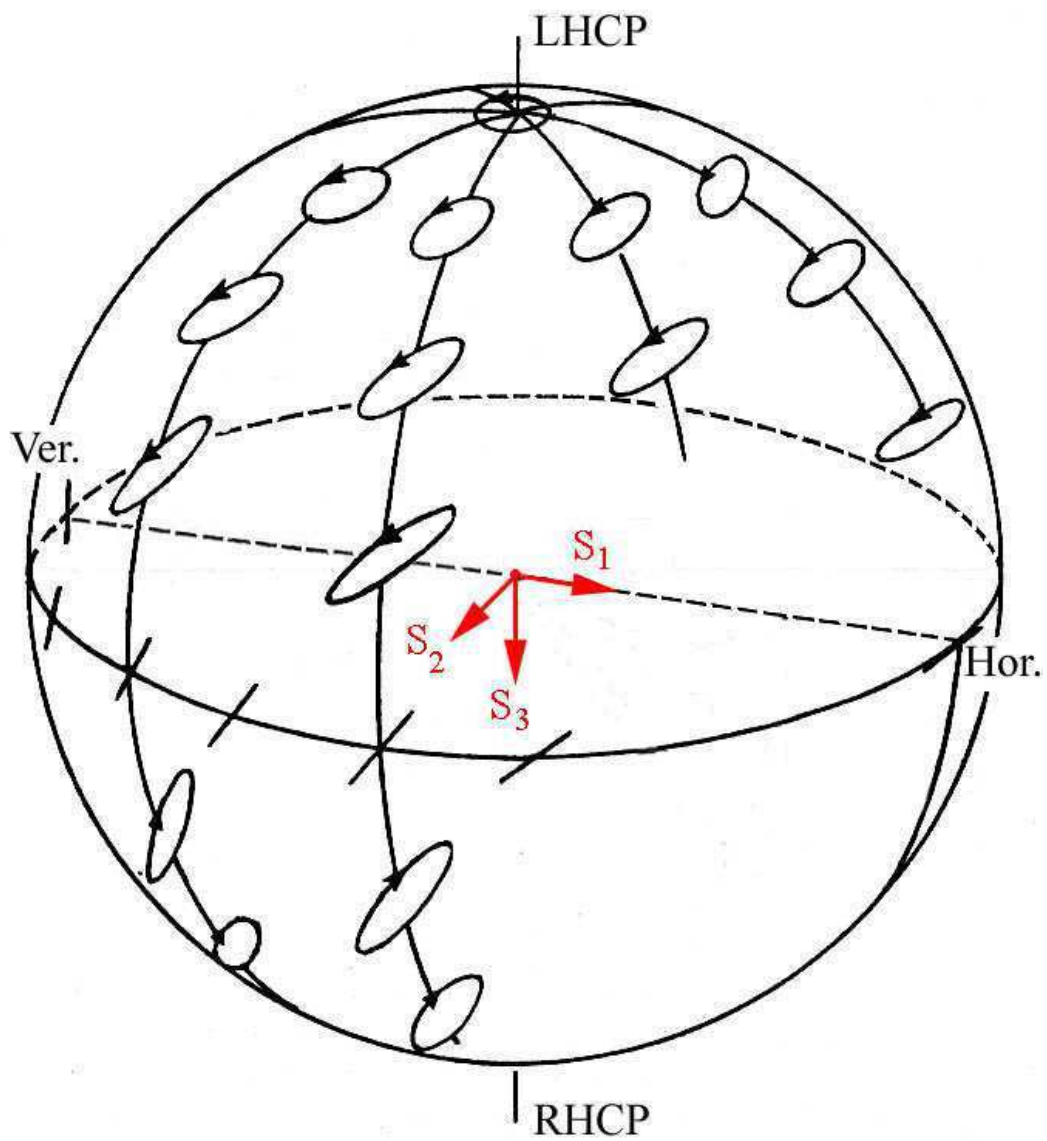


Fig. 2.1 Poincarè Sphere (adapted from [30]).

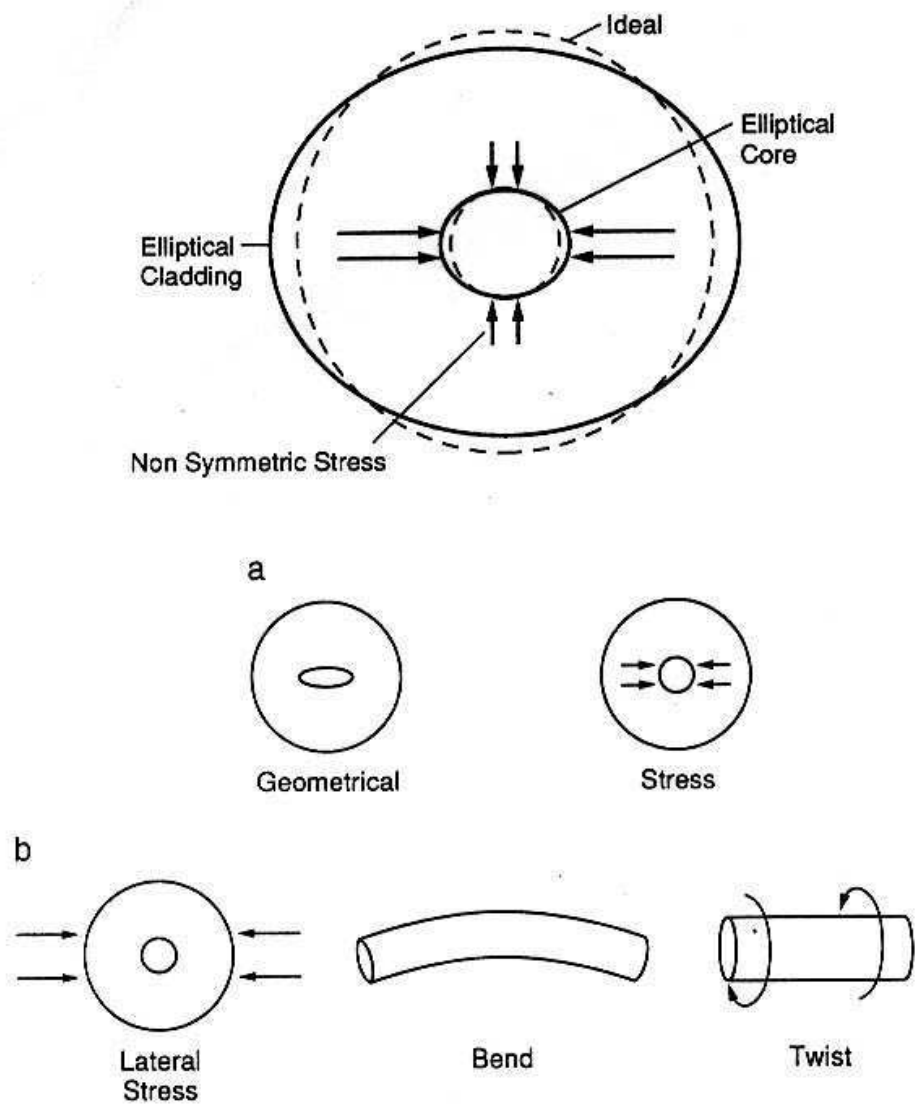


Fig. 2.2 a) Internal and b) External perturbations (adapted from [1]).

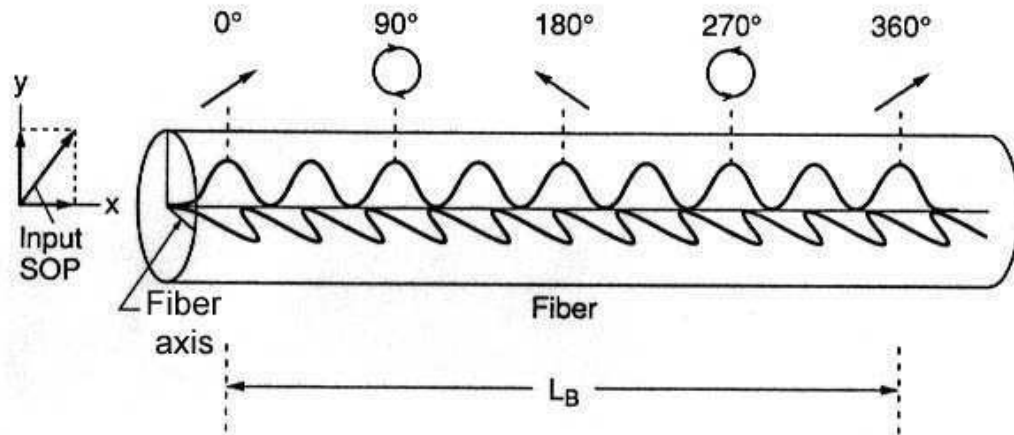


Fig. 2.3 Polarization evolution in a fiber (adapted from [1]).

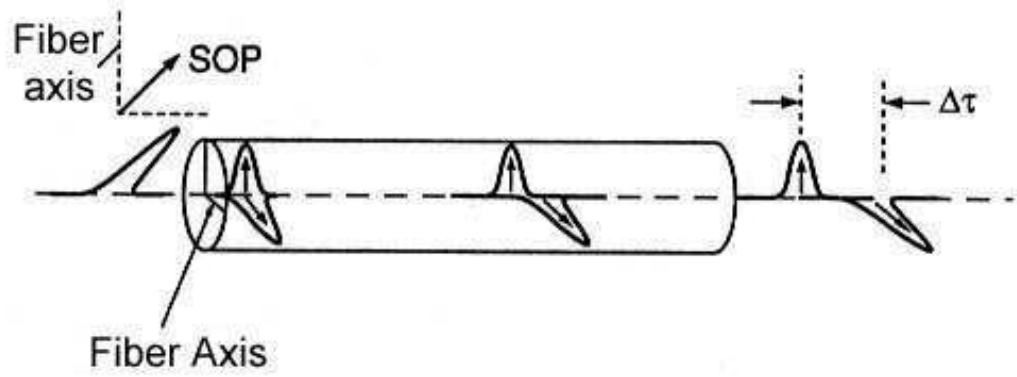


Fig. 2.4 DGD for a short section of fiber (adapted from [1]).

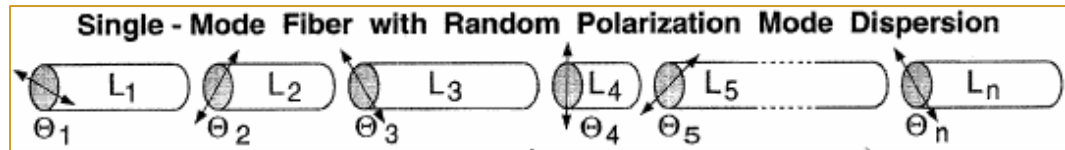


Fig. 2.5 Polarization mode coupling.

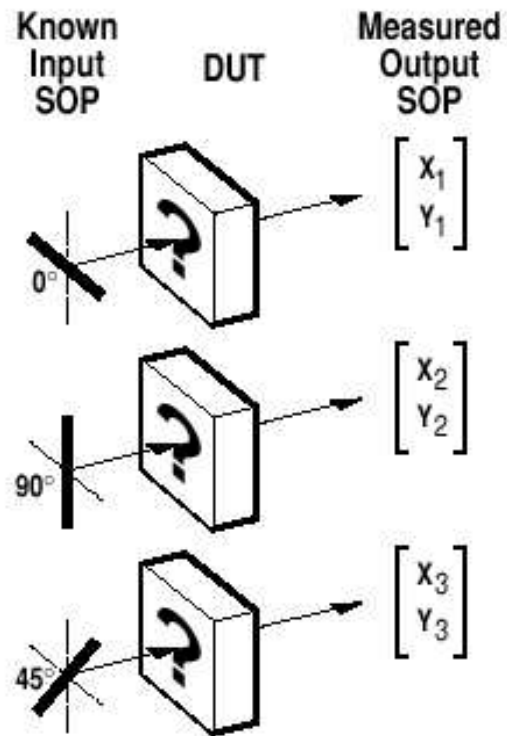


Fig. 2.6 Jones matrix characterization (adapted from [31]).

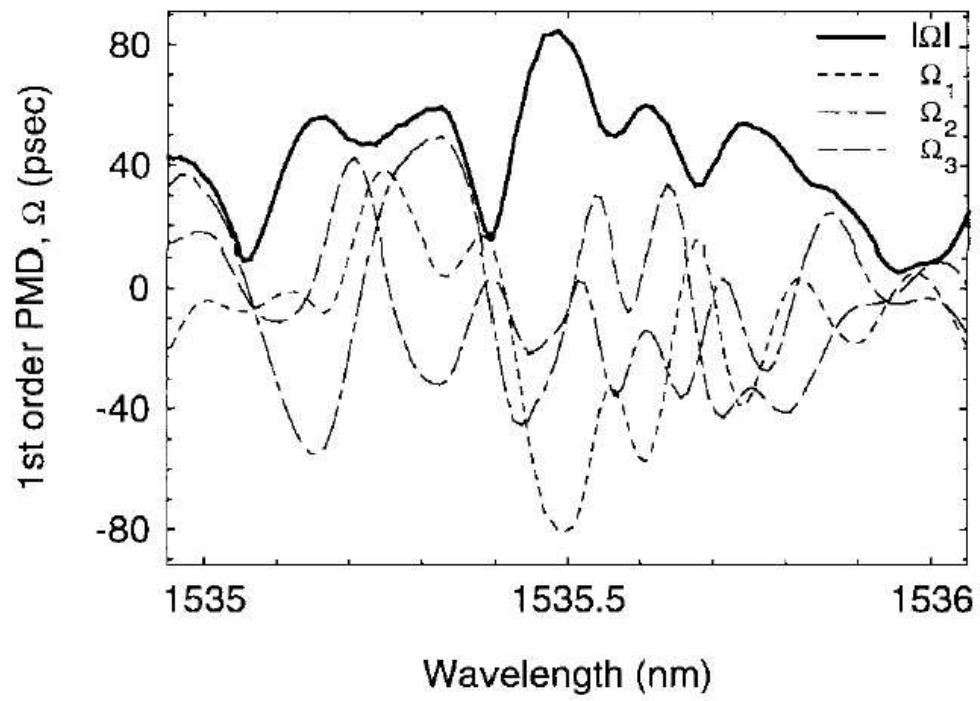


Fig. 2.7 PMD Vector measurement results using MMM method (adapted from [13]).

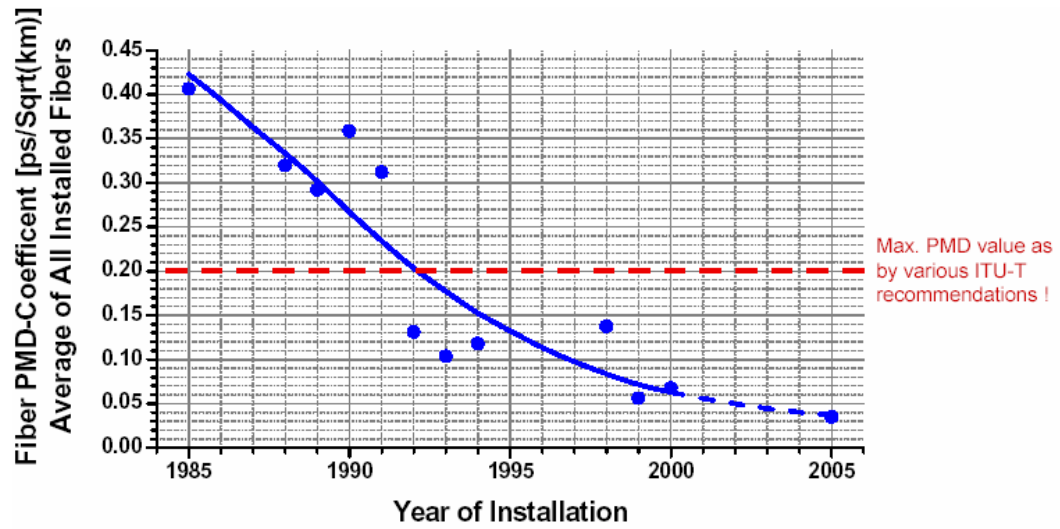


Fig. 2.8 Fiber PMD coefficient vs year of installation (adapted from[30]).

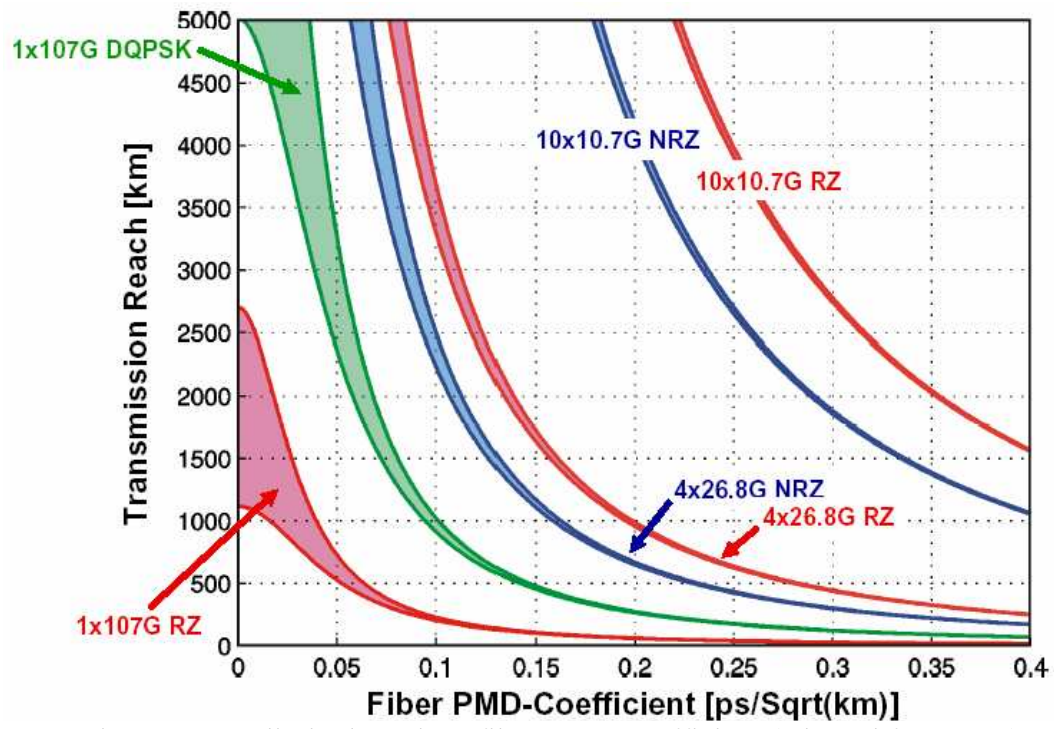


Fig. 2.9 PMD limited reach vs fiber PMD-coefficient (adapted from [30]).

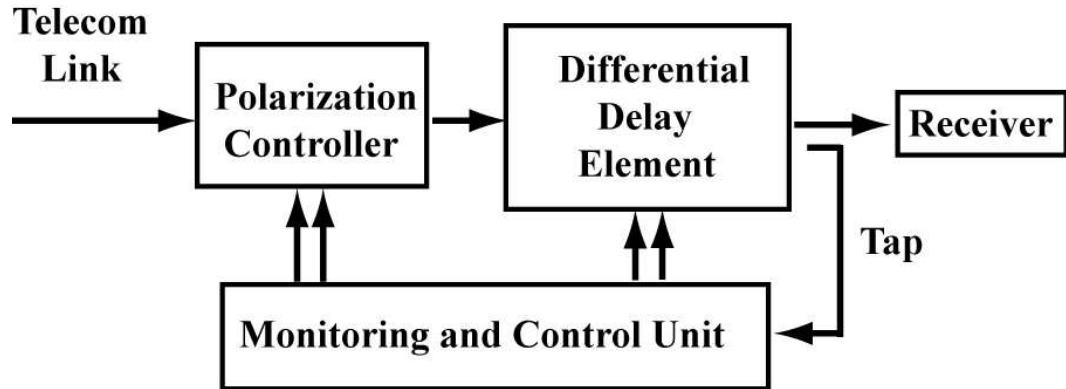


Fig. 2.10 Diagram for PMD vector compensation (adapted from [33]).

3. PMD COMPENSATION BASED ON THE PREVIOUS IDEA

In this chapter, we first summarize the previous work on PMD compensation finished by M. Akbulut [16, 17, 20, 33]. Then we focus on the efforts made to improve the performance of the previous PMD compensation system.

3.1 Previous PMD Compensation Idea and Results

In the previous PMD compensation algorithm, the all-order PMD effects are treated as frequency dependent polarization rotations and delays. Consequently, the PMD compensation idea consists of two parts: “broadband polarization correction”, and “broadband delay correction”. The key technology employed is the ultrafast pulse-shaping technique pioneered by Weiner et. al.. A pulse shaper typically consists of a disperser (for example, a grating), imaging elements (lenses), and a spatial light modulator (SLM) to manipulate the amplitude and/or phase of the incident signal as shown in Fig. 3. 1. The pulse is first dispersed spatially by the grating. Then the first lens images individual frequency components to individual spatial positions at the image plane. The SLM placed at the image plane modulated the signal on a wavelength-parallel basis. After that, another pair of lens and grating bring the frequency components back together. The components are arranged in a $4f$ scheme, which results in zero dispersion. The spatial Fourier Transforms of the input and output pulses are related by the spatial amplitude and phase transfer function of the SLM.

The most popular SLM devices are LCM arrays. An LCM device may consist of multiple layers. Each layer functions as an array of linear retarders with fixed fast axis and arbitrary adjustable retardance. For example, the most popular geometry (orientations of the fast axes) of a two-layer LCM is 45° - (-45°) . Commercially available LCM arrays might have 128 or 640 independent pixels per layer. The retardance of each pixel can be independently controlled by applying desired voltage. The responding time of each layer is ~ 100 ms. If the SOP of the input light is not aligned with the birefringence axis of an LCM layer, the LCM functions as a polarization rotation element, otherwise, it works as a

pure phase element. The LCM may also function as an amplitude modulator with the aid of polarizers.

In the previous system, all-order PMD compensation is achieved in two steps. In a first step, the PMD distorted SOP spectra are corrected to a single polarization state via a specially designed SOP pulse shaper (Fig. 3. 2). The SOP shaper incorporates a two-layer LCM array with a $90^\circ - (-45^\circ)$ (orientations of fast axes) geometry. For an arbitrary wavelength component at a corresponding pixel, the SOP correction process is shown in Fig. 3. 3. The SOP is first rotated around the birefringence axis of the first LCM layer to the plane containing the 90° axis and the RHC axis. Then the resulted SOP is rotated around the birefringence axis of the second LCM layer to the 90° axis. After the parallel operation of all the pixels, the distorted SOP spectra are corrected to a single polarization spectrum. A broadband polarimeter (Fig. 3. 4) is employed to measure the distorted SOP spectrum. The details of the polarimeter are described in [19]. The principle is to disperse different frequency components of the light under detection spatially, to select four polarization components (0° , 45° , 90° linear and RHC) with a pair of FLC retarders and a polarizer, and to measure the spectral intensities of those components with an arrayed detector (Sensor's Unlimited, SU256LX-17T1-0500-A/H in our experiments). The polarimeter data are used to control the SOP pulse shaper. Fig. 3.5 shows some examples of the SOP correction.

In a second step, the spectral phase of the corrected SOP spectrum is measured and corrected by a phase only pulse shaper. The overall experimental setup is shown in Fig. 3. 6. The second pulse shaper incorporates a two-layer LCM array with $45^\circ - (-45^\circ)$ geometry. The two LCM layers are operated in common mode which results in a phase only functionality [34]. In the previous work, the spectral phase was measured by measuring the temporal intensity profile via cross correlation, the power spectrum via OSA, then applying the Gerchberg-Saxton algorithm. The details of Gerchberg-Saxton algorithm are shown in Fig. 3. 7. Fig. 3. 8 shows some phase correction results. The problem of Gerchberg-Saxton algorithm is that it does not always work. Sometimes one needs to run iteratively the measure-compensate-measure process (as shown in Fig. 3.7) to achieve a clean pulse. And for some PMD profile, one can not get clean pulse even after the iterative measure-compensate-measure process.

3.2 PMD Vectors, Output SOP and Common Spectral Phase

In the previous work [33], Dr. Akbulut mentioned that it might be possible to derive all the required information for all-order PMD compensation from the PMD vectors, provided that the wavelength dependent PMD vectors can be accurately measured. In this section, we show how this can be done analytically. The chromatic dispersion, nonlinearity and PDL are neglected in the following analysis.

The output signal from a fiber link is related to the input signal by the Jones matrix of the fiber as,

$$\vec{E}_{out} = U\vec{E}_{in}, \quad (3.1)$$

where U is the frequency dependent Jones matrix of the fiber link. The polarization state of the incident signal is frequency independent, $\vec{E}_{in} = A(\omega)|s\rangle$, where $A(\omega)$ is the input power spectrum and $|s\rangle$ is the uniform Jones vector. The output signal can be written as $\vec{E}_{out} = A(\omega)U|s\rangle = A(\omega)|t\rangle$, where $|t\rangle$ is the output Jones vector. The relation between the output and input Jones vectors can be written as,

$$|t\rangle = U|s\rangle. \quad (3.2)$$

The output Jones vector can be written as, $|t\rangle = e^{j\psi} [\cos\theta \quad \sin\theta e^{j\varphi}]^T$, where ψ is defined as the common phase. The parameters θ and φ can be easily determined by measuring the Stokes vector of the output SOP, $\hat{t} = [\cos 2\theta \quad \sin 2\theta \cos \varphi \quad \sin 2\theta \sin \varphi]^T$.

By performing differential operation to both sides of Eq. (3.2) and eliminating $|s\rangle$, one get,

$$|t\rangle_{\omega} = U_{\omega}U^{\dagger}|t\rangle, \quad (3.3)$$

where the dagger denotes the Hermitian conjugate.

The Jones matrix is related to the PMD vector $\vec{\tau} = [\tau_1 \quad \tau_2 \quad \tau_3]^T$ through the following equation,

$$jU_{\omega}U^{\dagger} = \frac{1}{2} \begin{pmatrix} \tau_1 & \tau_2 - j\tau_3 \\ \tau_2 + j\tau_3 & -\tau_1 \end{pmatrix}. \quad (3.4)$$

From Eqs. (3.3) and (3.4), the relation between the common spectral phase and the output SOP (in the Stokes space), PMD vector can be derived as,

$$\psi_{\omega} = -\left[(\tau_1 + \vec{\tau} \cdot \hat{t}) / 2 \right] / (1 + t_1), \quad (3.5)$$

where t_1 is the first component of \hat{t} .

From the above analysis, one can conclude that all the required information for all-order PMD compensation based on the previous idea can be found provided that the output SOP and the PMD vector of the fiber link can be accurately measured. However, accurate measurement of the frequency-dependent PMD vectors itself remains a challenge. Therefore, we did not do experiments based on the above analysis.

3.3 Ultralow-Power SHG FROG for Characterization of All-Order PMD Distorted Femtosecond Waveforms

Although one can get some spectral phase information from Gerchberg-Saxton algorithm, it is not a popular technique for full pulse characterization. Currently, the two most popular pulse measurement techniques are FROG [21-24] and spectral phase interferometry for direct electric-field reconstruction (SPIDER) [35-39]. Here we explore SHG FROG for the characterization of the PMD induced spectral phase.

FROG is a powerful technique for measurement of ultrashort optical pulses [21-24]. In our previous work [40-45], by using aperiodically poled lithium niobate (A-PPLN) waveguides [46-48] as the nonlinear medium, we demonstrated ultralow-power multi-shot SHG FROG in the telecommunication band with a measurement sensitivity of $2.0 \times 10^{-6} \text{ mW}^2$, an 8 orders of magnitude improvement over SHG FROG using bulk crystals and 5 orders of magnitude better than previously reported for any FROG measurement modality [42]. This improved sensitivity allowed high quality pulse measurements at nanowatt to tens of nanowatt average power of subpicosecond pulses with a 50-MHz repetition rate. The reverse-proton-exchanged (RPE) waveguides fabricated on a z-cut PPLN substrate used in our experiments only guide light polarized along the crystal's z-axis (i.e. TM). While this in general requires proper polarization state preparation of the coupled waves, access to the largest nonlinear coefficient in lithium niobate (d_{33}) allows for efficient nonlinear mixing; the next largest nonlinear coefficient that involves the nonlinear mixing of TE and TM modes (d_{31}) is approximately six times smaller. Nonlinear conversion efficiencies in excess of 100%/W-cm² have been achieved for SHG of fundamental harmonic (FH) inputs in the telecommunications C-band, while FH propagation losses below 0.1 dB/cm are common for RPE waveguides. Since waveguides with 6-cm-long quasi-phase-matched (QPM) gratings are easily fabricated, overall conversion efficiencies as large as 3.6%/mW are achievable. Furthermore, by applying appropriately designed aperiodic poling patterns,

one can broaden the phase matching bandwidth more than one hundred fold to ~ 25 nm, which is needed for measurement of subpicosecond pulses.

The first ultralow-power SHG FROG experiment was carried out in our group by S.-D. Yang. The experimental setup is shown in Fig. 3. 9, where a free-space-coupled A-PPLN waveguide with a 25-nm-wide phase-matching bandwidth centered at 1538 nm is used for SHG. We employ a passively mode-locked fiber ring laser and a band-pass filter to generate a 50-MHz, ~ 280 -fs pulse train at 1538-nm center wavelength. The pulse train is sent into a modified collinear Michelson interferometer, where the unwanted interferometric fringes are removed by fast dithering of the “fixed” arm of the interferometer using a piezoelectric transducer [43]. The output SH power spectrum from the A-PPLN waveguide is recorded by a spectrometer and an intensified CCD camera for each delay, giving rise to a fringe-suppressed raw FROG trace, which has a nonzero background and is spectrally distorted by the somewhat uneven phase-matching spectrum of the A-PPLN waveguide. Subsequent software processing deals with: (i) background subtraction, (ii) frequency marginal correction [21] (with the aid of the fundamental power spectrum taken by an optical spectrum analyzer), and (iii) intensity and phase reconstruction by a commercial software (Femtosoft FROG 3).

Fig. 3.10 illustrates measured (after background subtraction and marginal correction) and retrieved FROG traces at coupled pulse energies of 9.5 fJ (A-B) and 124 aJ (C-D), respectively [40]. Even with a 19-dB input power difference (38 dB difference in SHG powers), these FROG traces agree well with one another. The FROG errors are 0.0022 and 0.0032, respectively. Fig. 3.10 also shows the retrieved pulses in (E) frequency, and (F) time domains for both input power levels. An independently measured input power spectrum is plotted as a dotted curve in Fig. 3.10 (E) for comparison. The retrieved spectral intensities closely approach this curve. The retrieved temporal profiles also overlap well with each other, where the intensity full width at half maximum (FWHM) values are essentially identical: 279 fs and 278 fs, respectively. The low-power measurement is equivalent to 0.44-mW peak power, and 6.2-nW average power, corresponding to a measurement sensitivity of 2.7×10^{-6} mW².

The performance of the FROG setup using a free-space-coupled A-PPLN waveguide is mainly limited by the time-dependent free-space-to-waveguide coupling efficiency induced by mechanical drifts. As a result, it was not successful to use the setup to characterize PMD distorted optical pulses.

The simplest and most robust way to eliminate coupling efficiency fluctuations is to use a fiber-pigtailed A-PPLN waveguide. The FROG setup is the same as that shown

in Fig. 3.9., except that the free-space-coupled A-PPLN waveguide is replaced by a fiber-pigtailed one. (We retain free-space coupling for the output end of the waveguide.) The center wavelength of the phase-matching curve of the fiber-pigtailed A-PPLN waveguide is 1550 nm at room temperature and the bandwidth is ~ 25 nm. We use a tunable bandpass filter (FWHM ~ 10 nm) to select ~ 360 -fs optical pulses with a 1550-nm center wavelength from a passively mode-locked fiber ring laser operating at a 50-MHz repetition rate. We performed FROG measurements of nearly bandwidth-limited pulses with a coupled average power of 6 nW, corresponding to a measurement sensitivity of 2.0×10^{-6} mW² with the 360-fs pulse width. Fig. 3.11 shows the measurement results, where a flat spectral phase is retrieved.

We first demonstrate full characterization of femtosecond pulse distortion induced by all-order PMD effects at selected polarization states via the ultralow-power SHG FROG setup with the fiber-pigtailed A-PPLN waveguide, which proves that the technique has the capability of retrieving extremely complicated waveforms resulting from all-order PMD-induced distortions [44]. The experimental setup is shown in Fig. 3.12. A passively mode-locked fiber ring laser followed by a bandpass filter are used to produce ~ 360 femtosecond optical pulses with ~ 50 MHz repetition rate and 1550 nm center wavelength. The pulses are relayed into a fiber-coupled reflective Fourier-transform pulse shaper, which incorporates a two-layer, 128-element liquid crystal modulator array to apply spectral phase. The two layers of the liquid crystal modulator are programmed in common-mode, resulting in a polarization-insensitive phase-only modulation functionality. The output of the pulse shaper is launched into a home-made PMD emulator consisting of 8 sections of polarization maintaining (PM) fibers spliced at various angles. The distorted pulses are then transmitted through a polarizer into the measurement setup. Since the mean DGD (~ 1.3 picoseconds) of the PMD module is much greater than the pulse width, strong all-order PMD effects are present which cause complicated variation of SOP with frequency. This leads to reshaping of the spectrum after the polarizer. With two PCs placed before and after the PMD module respectively, we can select arbitrary polarization slices for spectral phase characterization and correction. In our initial experiment the chromatic dispersion of the PMD module is not pre-compensated. The phase correction is run in pre-compensation mode. The same results can be achieved in post-compensation mode.

Fig. 3.13 shows the FROG data of the chromatic dispersion and PMD-distorted pulse at a selected polarization slice. The quadratic spectral phase is mainly caused by the chromatic dispersion, while the complexity of the pulse in the time domain is due to all-

order PMD. Fig. 3.14 shows the FROG data after applying the inverse of the measured spectral phase via the pulse shaper. The pulse is compressed from more than 3 ps (at 10% intensity level) in duration to 484 fs (FWHM), which is close to the bandwidth limit. Both PMD and chromatic-dispersion-induced distortions are almost completely compensated.

We kept the applied spectral phase with the phase-only pulse shaper and adjusted the input and output PCs to select another polarization slice. In this case, the chromatic dispersion had been fully compensated in the previous trial. The observed pulse distortion was caused by the difference between the PMD induced spectral phases (PMD induced pulse distortion are polarization dependent) of the two experimental trials. The temporal intensity profiles of the distorted and restored pulses are shown in Fig. 3.15. The pulse is stretched to about 2 ps by PMD and compensated to a bandwidth-limited pulse of 400 fs.

It is worth noting that PMD-induced spectral reshaping after the polarizer accounts for the small pulse-width differences between the initial pulse and the pulses after correction, while the FROG retrieval algorithm accounts for the slight differences of the spectra before and after phase compensation. Since spectral phase plays the primary role in pulse distortion, the slight difference in retrieved spectra is not a significant problem.

By adjusting the PCs before and after the PMD module, we carried out the experiments several times. Each time, after correcting the PMD-induced spectral phase, we were able to obtain nearly bandwidth-limited pulses, which demonstrates the applicability of FROG measurements of PMD-distorted pulses.

3.4 Polarization Insensitive Ultralow-Power SHG FROG

Before demonstrating all-order PMD compensation with SHG FROG, we first introduce polarization insensitive ultralow-power SHG FROG. As introduced in the previous section, the waveguide in our FROG setup only supports a single polarization state (vertical), random fluctuations of the input SOP arising from small birefringences of the optical fibers in the measurement loop will seriously degrade the FROG measurements. We overcome this serious polarization sensitivity by scrambling the input SOP at a rate much faster than the measurement integration time [45]. This is important for our PMD compensation work because the two pulse shapers (the SOP pulse shaper and the spectral phase pulse shaper) are on different optical tables and the airflow in the

room will introduce some random polarization fluctuations through the unsecured fibers connecting the two pulse shapers.

Figure 3.16 shows the scheme of the polarization insensitive FROG setup. We use a passively mode-locked fiber ring laser together with a bandpass filter to produce ~ 360 fs pulses with 50 MHz repetition rate and 1550 nm central wavelength. The SOP of the pulses is then scrambled uniformly on the Poincare sphere with a wideband fiber-pigtailed polarization scrambler (General Photonics Corporation, PCD-104), with more than 100 nm operating range centered at 1550 nm, and 700 KHz scrambling frequency. The scrambled pulses are then launched into a Michelson interferometer to produce pulse pairs with various delays. One of the interferometer arms is dithered over a few optical cycles at a rate of 160 Hz to wash out the interference fringes. The pulse pairs are coupled into the A-PPLN waveguide with a fiber-pigtailed collimator to produce SHG signals. The dispersion of the fiber link is compensated with dispersion compensating fiber (DCF). The SHG spectrum for each delay is recorded by a spectrometer and an intensified CCD camera with 800 ms exposure time, which yields the raw FROG data. To get a background-free FROG trace, a spectrum taken at a large delay is subtracted from the raw data. The spectrum of the FH pulses is recorded separately by an OSA for frequency marginal correction. We use commercial software (Femtisoft FROG) to completely retrieve the intensity and phase information of the pulses.

Polarization scrambling will result in the desired polarization-insensitive FROG measurement functionality when three key assumptions are satisfied: (1) the polarization scrambler is slow compared to the pulse duration; (2) the polarization scrambler is sufficiently fast compared to the detector integration time that measurements yield ensemble average results corresponding to an input SOP distributed uniformly on the Poincare sphere; (3) the input SOP is frequency-independent.

We first test the FH power coupled through the A-PPLN waveguide and the generated SHG power with the polarization scrambler on and with the scrambler off and the input SOP aligned for maximum coupling. We use a power meter to measure the FH power and a PMT together with a lock-in amplifier to measure the SHG power. The measurement integration time is tens of milliseconds in both cases, which is much greater than the scrambling period. The scrambled SOP can be treated as a uniform distribution on the Poincare sphere, where SOP is described by a 3×1 vector $[s_1 \ s_2 \ s_3]^T$. Since the waveguide only supports vertical polarization, the ratio of the coupled FH power with scrambler on and off (but with optimized input SOP) can be written as $\frac{1}{4\pi} \oint_S \frac{1-s_1}{2} dS$,

which results in $1/2$. The ratio of the SHG power can be calculated with $\frac{1}{4\pi} \oint_s \left(\frac{1-s_1}{2}\right)^2 dS$, which is $1/3$. The same results can be obtained in the Jones space. The normalized Jones vector of the scrambled electrical field is $|s\rangle = [a \ b]^T$, where $|a|^2$ and $|b|^2$ both follow uniform distribution within range $[0, 1]$. The ratio of the coupled FH power with scrambler on and off (but with optimized input SOP) can be written as $\int_0^1 |b|^2 d|b|^2 = 1/2$. The ratio of the SHG power is $\int_0^1 |b|^4 d|b|^2 = 1/3$. The measurement yields coefficients of 0.505 ± 0.004 and 0.341 ± 0.005 , respectively, which is very close to the calculation.

To check the performance of our setup, we characterize nearly bandwidth limited, ~ 360 fs pulses at 50 MHz repetition rate and 1550 nm centre wavelength. To enhance the polarization fluctuation effects, we randomly adjust the SOP from the source by hand with a PC. We first perform the FROG measurement with the scrambler off using a maximum of 19 nW FH power coupled through the guide. Fig. 3.17 shows the experimental results. The measured FROG trace exhibits random power fluctuation with time, and the retrieved FROG trace is totally different from the measured one. Furthermore, the retrieved spectrum is far away from the spectrum measured by the OSA. All of these indicate a bad measurement.

Then we repeat this experiment with the scrambler on, while continuing to randomly adjust the input SOP. The measurement is performed at an average of 5.2 nW FH power coupled through the guide, which corresponds to the same SHG power as the measurement in [41]. Fig. 3.18 shows the measurement results. The measured pulse FWHM is 352 fsec, very close to that of the input pulses. The retrieved spectrum is very close to that measured by the OSA, and the FROG error is 0.0047. All of these points indicate a high quality waveform retrieval. We have also performed additional measurements which show that our polarization-insensitive FROG scheme does not introduce additional FROG error compared to FROG measurements with a fixed, optimized input SOP, provided that the average SHG output is held constant.

3.5 All-Order PMD Compensation with Polarization Insensitive SHG FROG

In this section, we demonstrate all-order PMD compensation using polarization insensitive ultralow-power SHG FROG for spectral-phase sensing. Fig. 3.19 shows the experimental setup. The SOP pulse shaper (shaper 1) and the spectral-phase pulse shaper

(shaper2) are located on different optical tables. We use a pulse source (different from the previously used) located on the same table as the SOP shaper to produce ~ 600 -fs optical pulses (~ 5 -nm FWHM in the spectral domain) with ~ 50 -MHz repetition rate and 1550-nm center wavelength. The pulses are launched into the homemade PMD emulator (same as previous used). The SOP of the output spectrum is measured with a broadband polarimeter. We use a specially designed SOP pulse shaper to correct the output SOP spectrum to a fixed polarization state on a wavelength-parallel basis (as described in details in section 3.1). The pulses after SOP correction are then input into a second phase-only pulse shaper. Since a 20-m-long SMF is used to connect the two pulse shapers, we applied the polarization insensitive FROG technique to measure the pulses after the second shaper. By using the FROG data to control the phase-only shaper, we achieved full PMD compensation.

To check the performance of the SOP correction, we placed a polarizer after pulse shaper 1 and measured the spectra after the polarizer with and without SOP correction and compared them with the initial spectrum without PMD. Fig. 3.20 shows one of the measurement results. The spectrum is heavily distorted by PMD and is corrected to close to the initial spectrum after SOP correction, which signifies good accuracy of the SOP measurement and correction. Note, the peak intensity of each spectrum has been normalized to 1.

Fig. 3.21 shows FROG data of the optical pulses after SOP correction but before spectral phase correction of one of the experimental trials. The pulses are spread to more than 3 ps (full width at 10% intensity). By applying the inverse of the measured spectral phase, the pulses are compressed to near-bandwidth-limited 642-fs pulses as shown in Fig. 3.22. This is evident from the FROG traces, which are now essentially without structure, and from the flat measured spectral phase profile, as well as from the profile in the time domain. By adjusting the input SOP to the PMD emulator with a PC, we carried out the PMD compensation experiments several times. Each time we were able to compensate the pulses to similar near-bandwidth-limited ~ 600 -fs pulses immediately after the SOP and phase-correction process. Fig. 3.23 shows the temporal intensity profiles of the distorted (after SOP correction but before phase correction) and restored (after phase correction) pulses of another experimental trial, where the pulse is compressed to 622 fs after PMD compensation. The experimental results indicate that the proposed polarization insensitive SHG FROG technique is robust in retrieving PMD distorted waveforms.

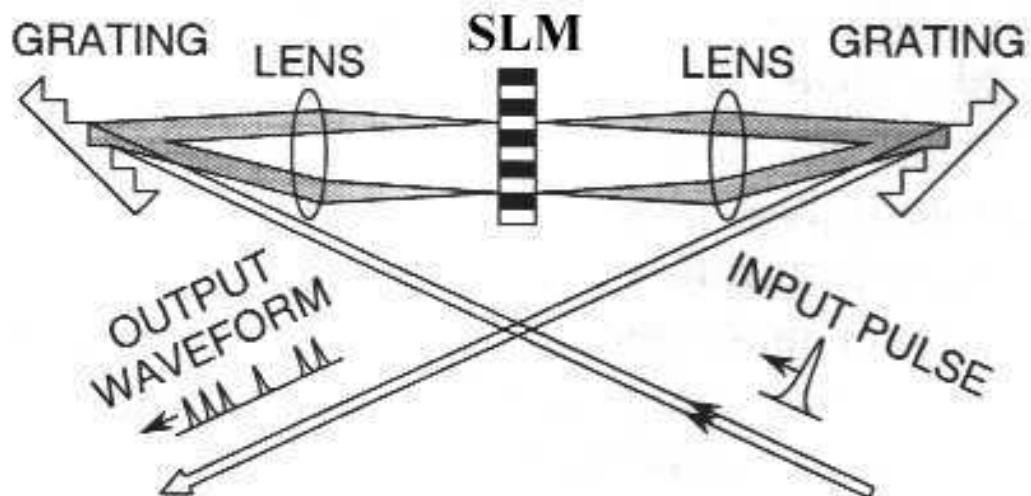


Fig. 3.1 Ultrafast pulse shaping apparatus (adapted from [18]).

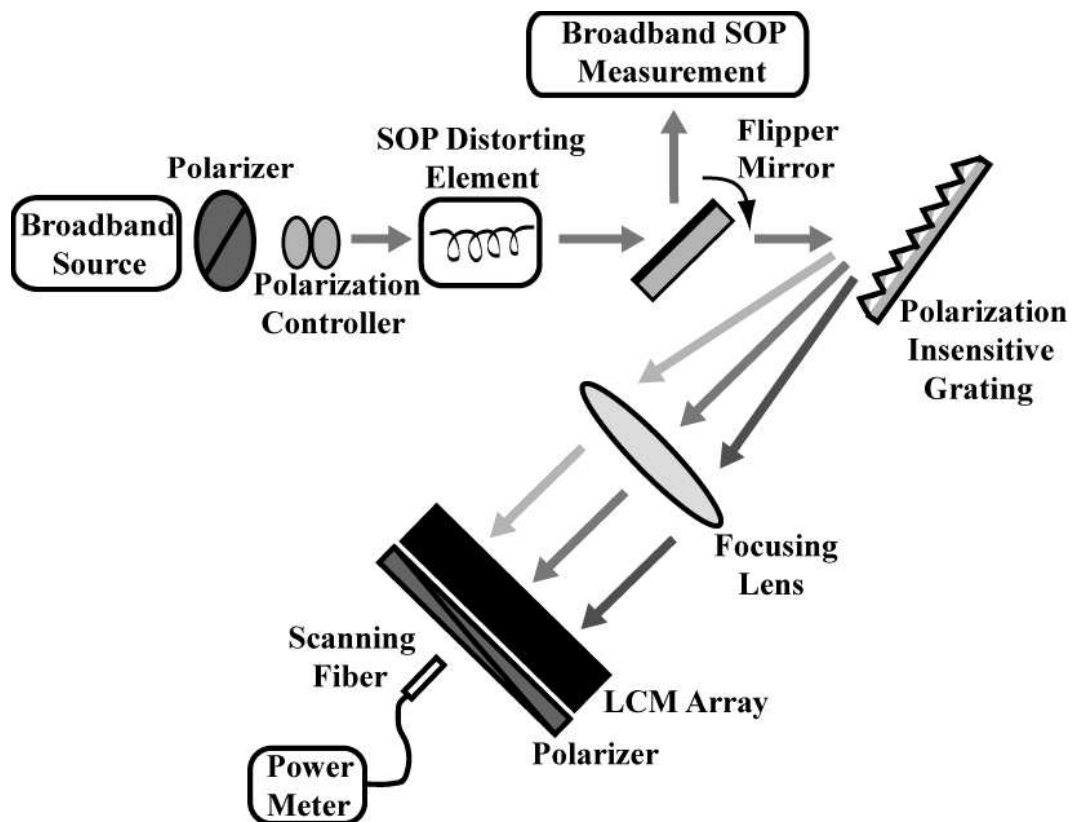


Fig. 3.2 SOP correction setup (adapted from [20]).

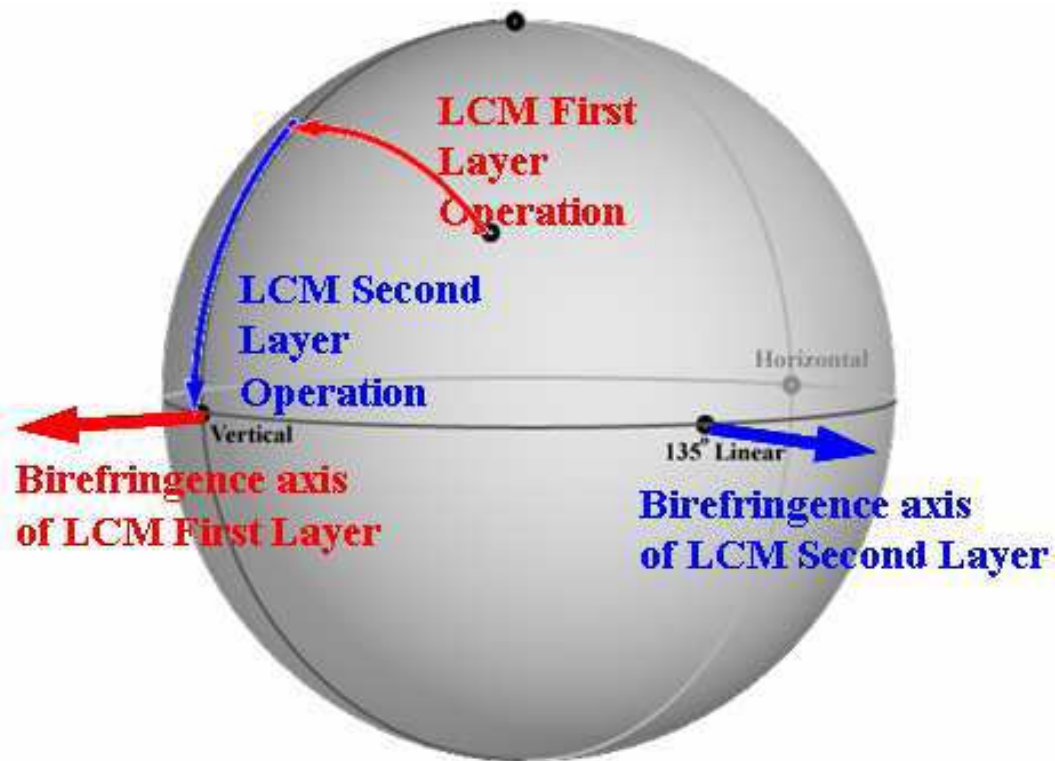


Fig. 3.3 SOP correction algorithm (adapted from [33]).

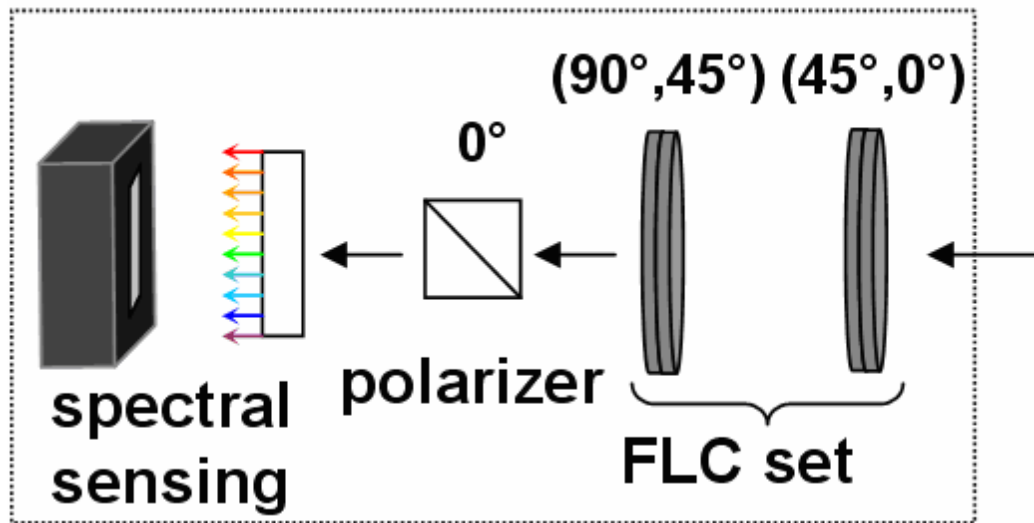


Fig. 3.4 Wavelength-parallel polarimeter (adapted from [19]).

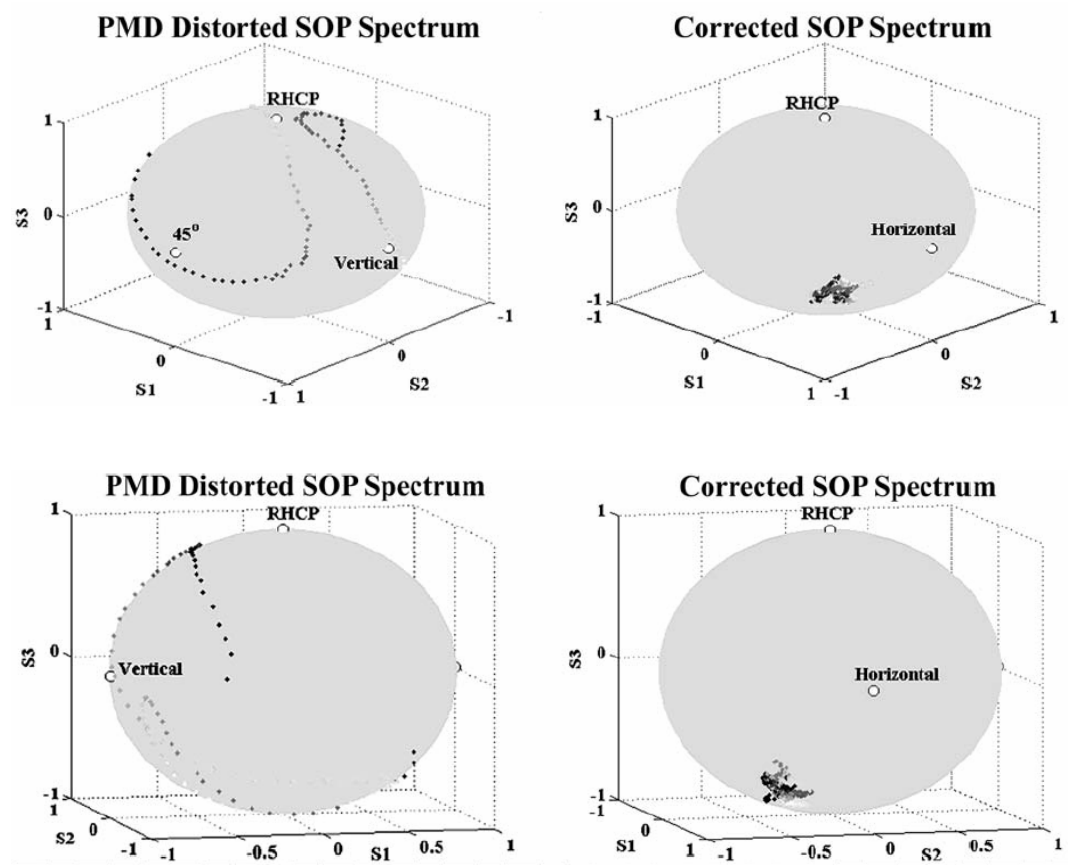


Fig. 3.5 SOP correction examples (adapted from [16]).

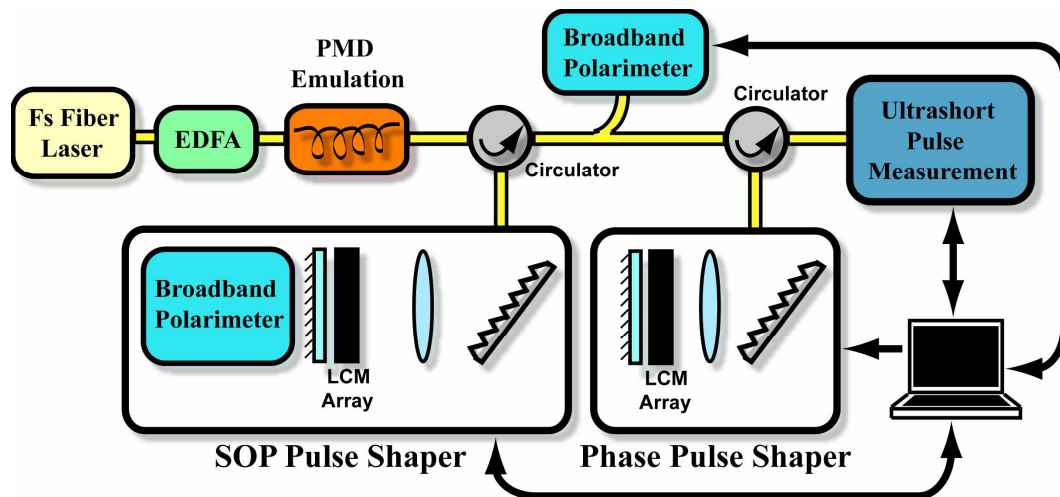


Fig. 3.6 PMD compensation setup (adapted from [33]).

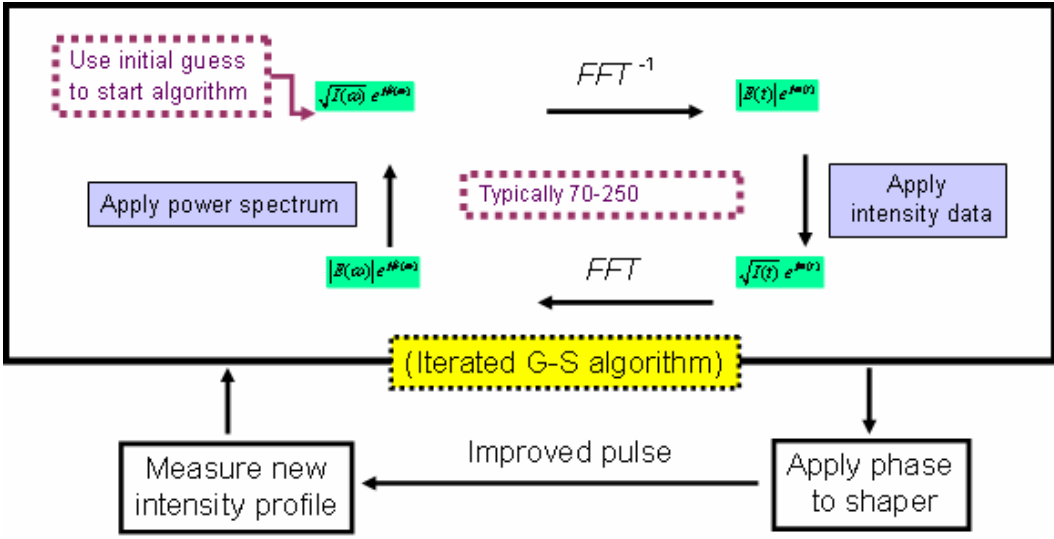


Fig. 3.7 Iterated Gerchberg-Saxton algorithm for spectral phase correction.

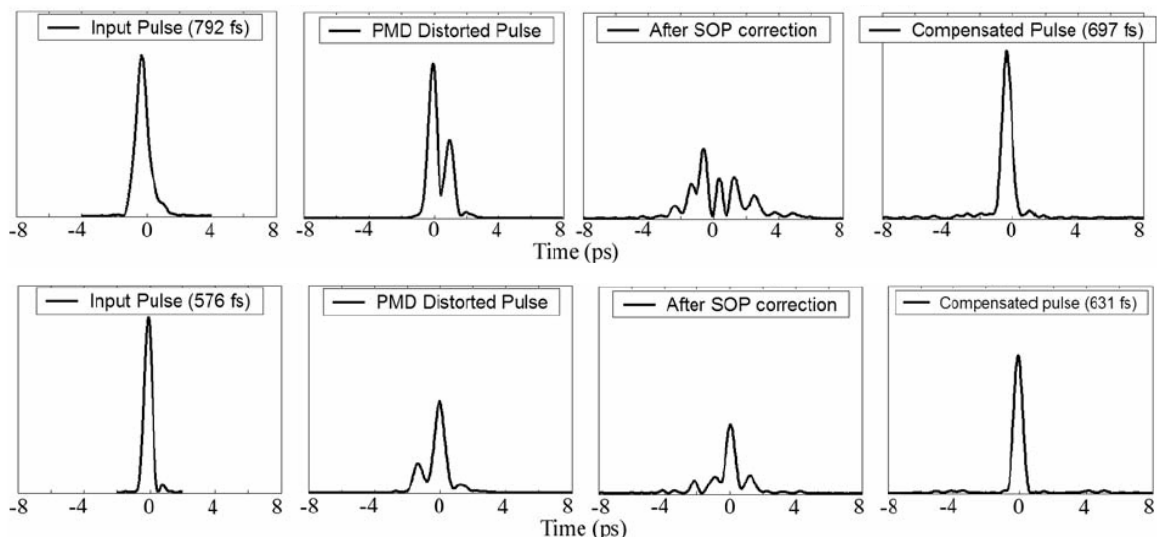


Fig. 3.8 PMD compensation examples (adapted from [16]).

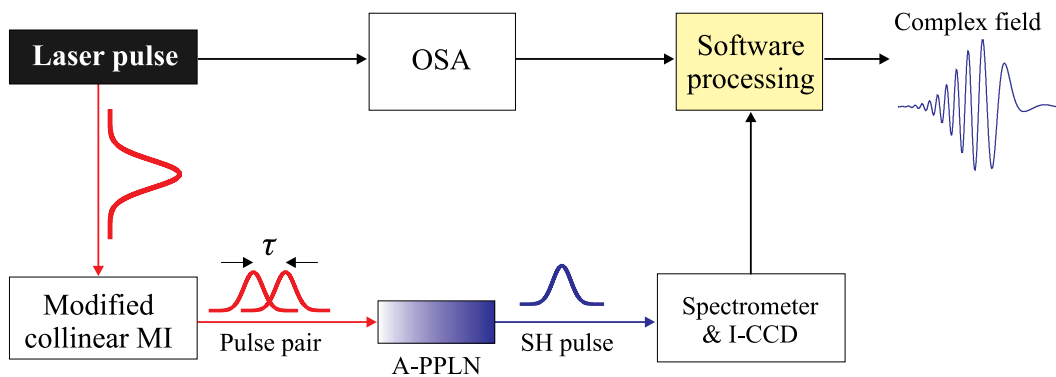


Fig. 3.9 Schematic diagram of SHG FROG using an A-PPLN waveguide. MI: Michelson interferometer. OSA: optical spectrum analyzer. I-CCD: Intensified CCD camera (adapted from [42]).

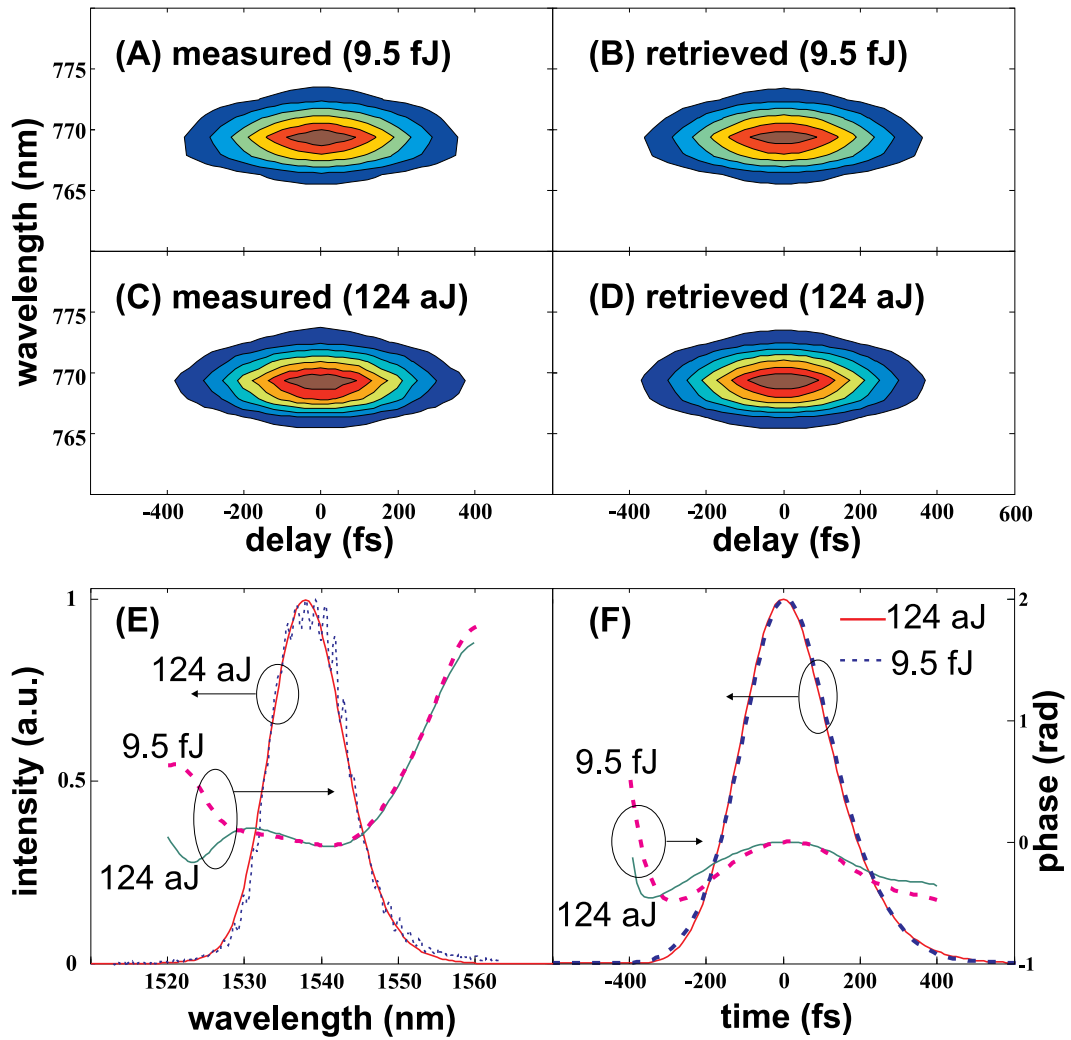


Fig. 3.10 FROG data of nearly bandwidth-limited pulses with free-space-coupled A-PPLN. (A) Measured, and (B) retrieved FROG traces at 9.5 fJ. (C) Measured, and (D) retrieved FROG traces at 124 aJ. Retrieved pulse illustrated in: (E) frequency domain, and (F) time domain for both 9.5-fJ and 124-aJ coupled pulse energies. Dotted curve in (E) represents the independently measured power spectrum (adapted from [42]).

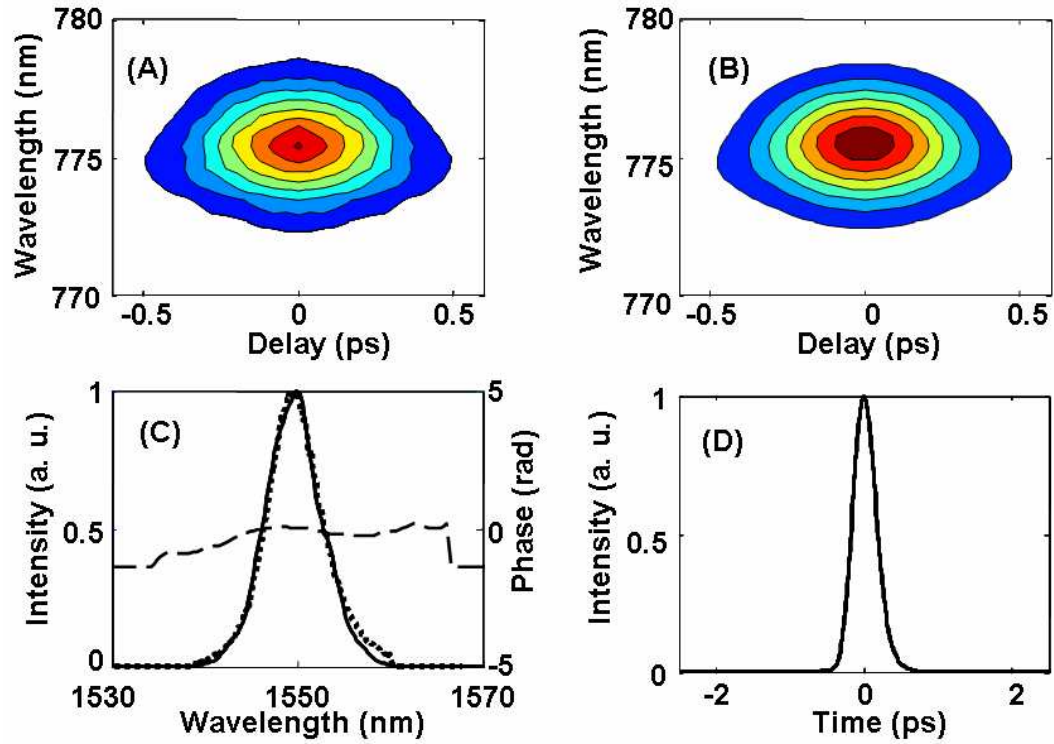


Fig. 3.11 FROG data for bandwidth-limited optical pulses with a fiber-pigtailed A-PPLN. (A) Measured FROG trace. (B) Retrieved FROG trace. (C) Retrieved spectral intensity (solid) and phase (dashed) profiles together with the spectrum recorded by OSA (dotted). (D) Retrieved temporal intensity profile.

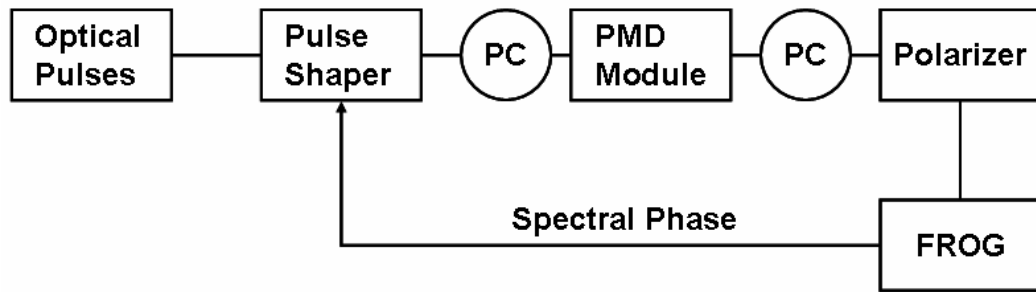


Fig. 3.12 Experimental setup for sensing and compensation of PMD induced pulse distortion at selected polarization slices controlled via SHG FROG. PC: polarization Controller.

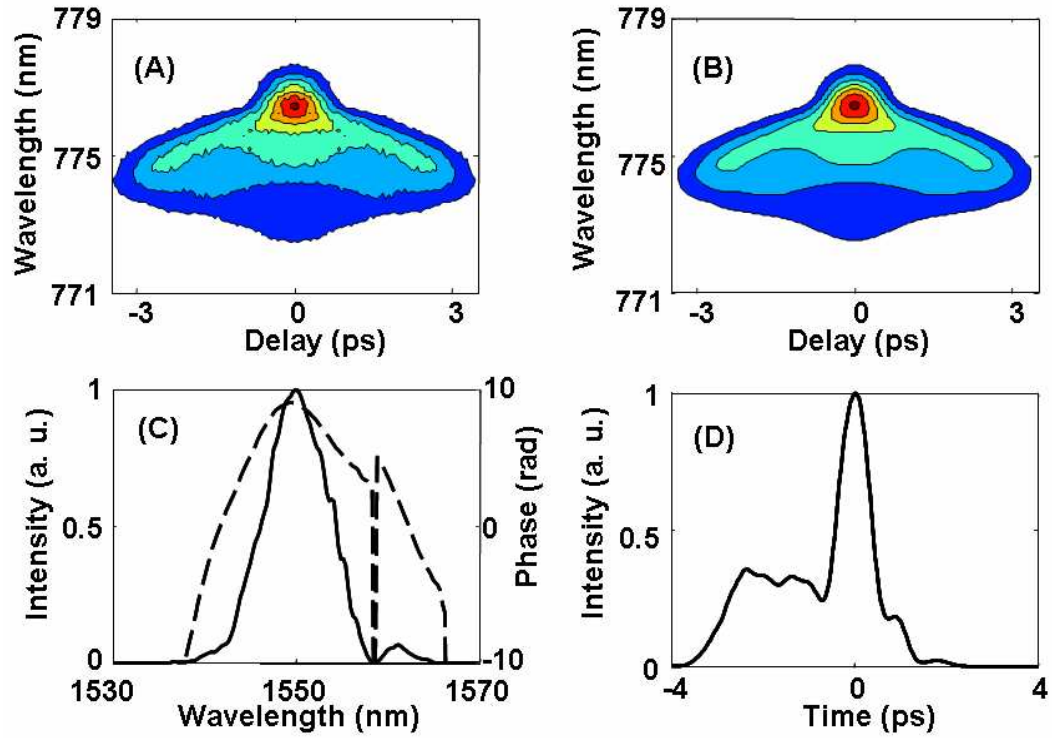


Fig. 3.13 FROG data of chromatic dispersion and all-order PMD distorted pulses at a selected polarization slice. (A) Measured FROG trace. (B) Retrieved FROG trace. (C) Retrieved spectral intensity (solid) and phase (dashed) profiles. (D) Retrieved temporal intensity profile.

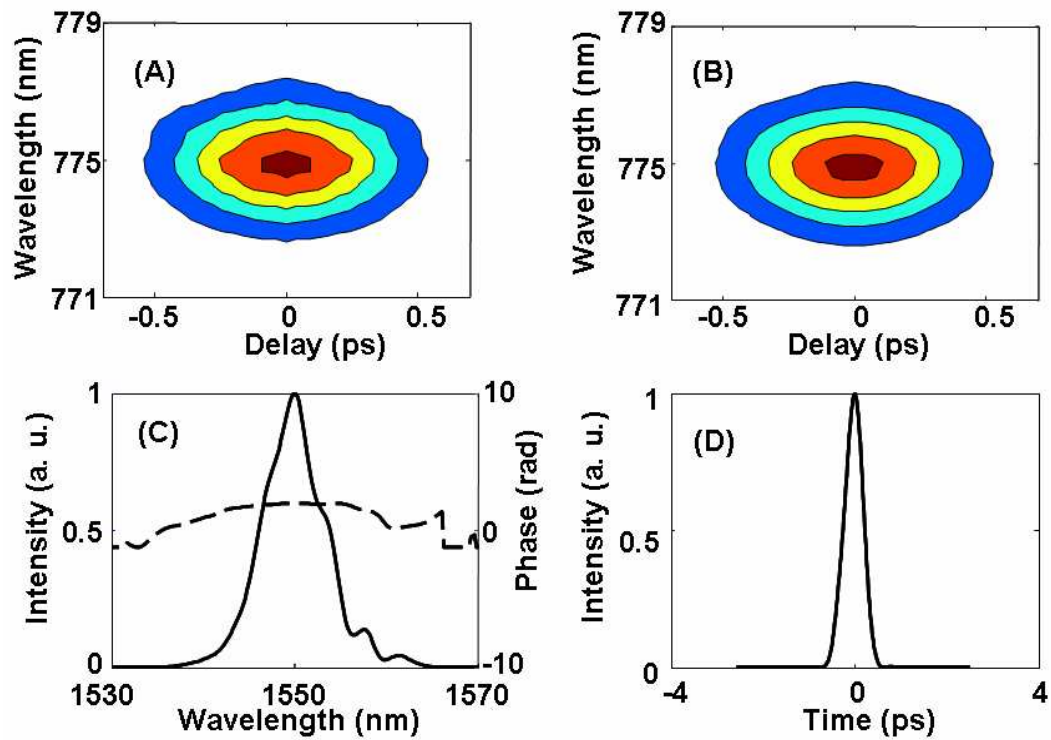


Fig. 3.14 FROG data after spectral phase correction. (A) Measured FROG trace. (B) Retrieved FROG trace. (C) Retrieved spectral intensity (solid) and phase (dashed) profiles. (D) Retrieved temporal intensity profile.

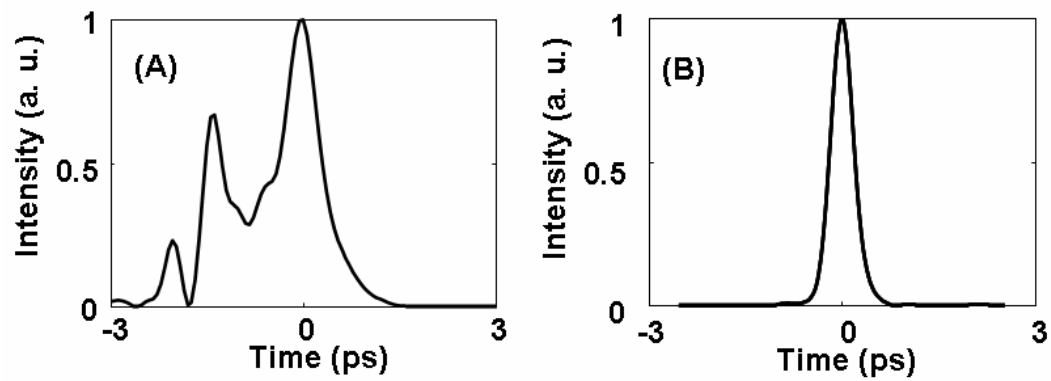


Fig. 3.15 Temporal intensity profiles of the distorted (A) and restored (B) pulses.

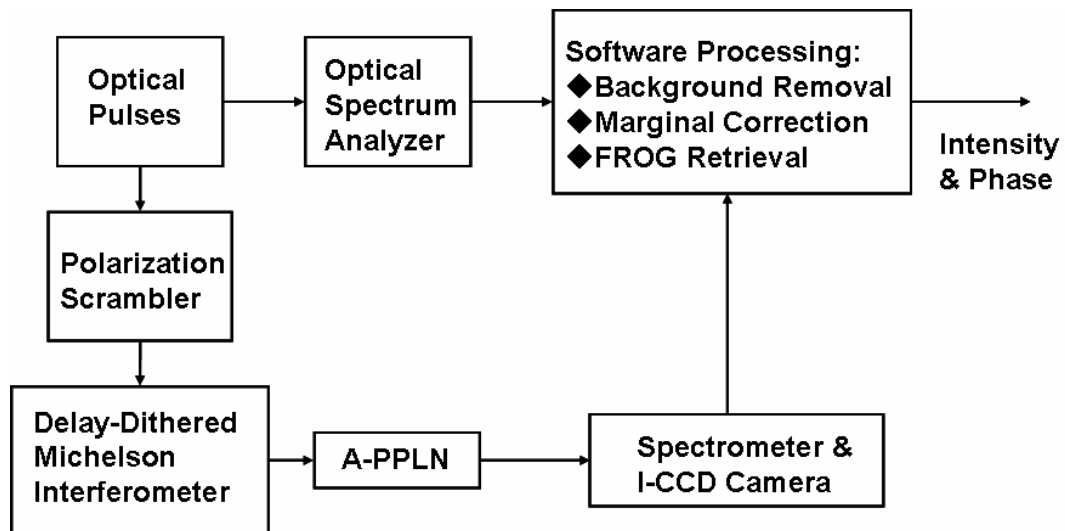


Fig. 3.16 Polarization insensitive ultralow-power SHG FROG setup.

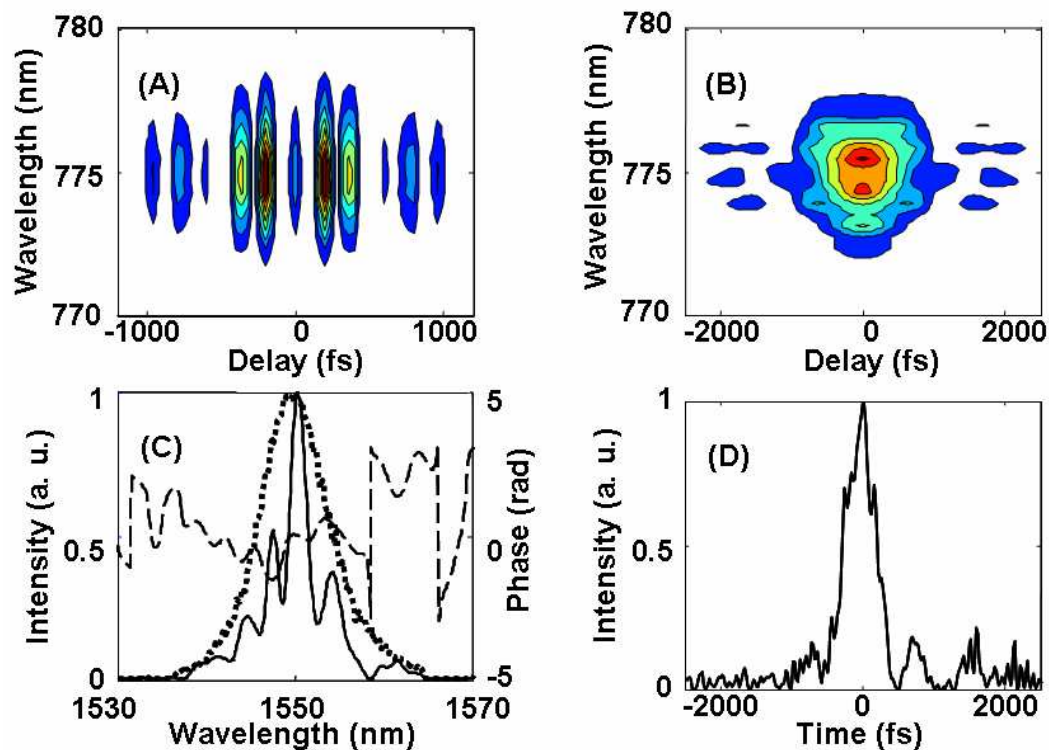


Fig. 3.17 FROG data with time-varying polarization fluctuations intentionally introduced, and scrambler off. (A) Measured FROG trace. (B) Retrieved FROG trace. (C) Retrieved spectral intensity and phase profiles. (D) Retrieved temporal intensity profile. Dashed line (in C): spectral phase profile; dotted line (in C): spectrum recorded by OSA.

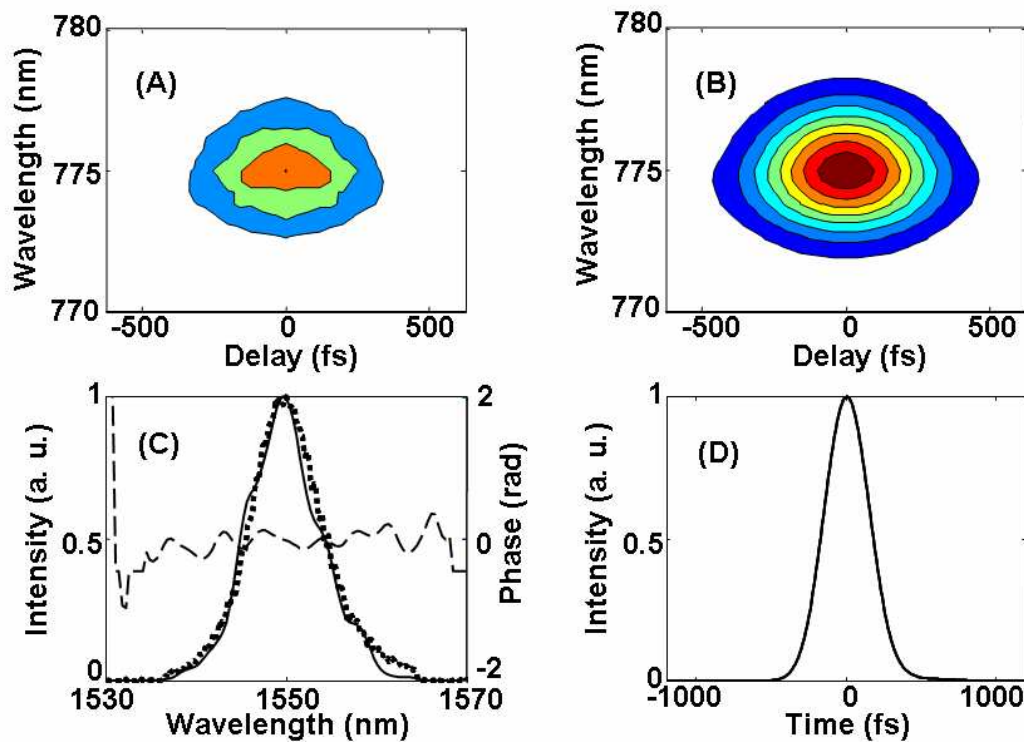


Fig. 3.18 FROG data with time-varying polarization fluctuations intentionally introduced, and scrambler on. (A) Measured FROG trace. (B) Retrieved FROG trace. (C) Retrieved spectral intensity and phase profiles. (D) Retrieved temporal intensity profile. Dashed line (in C): spectral phase profile; dotted line (in C): spectrum recorded by OSA.

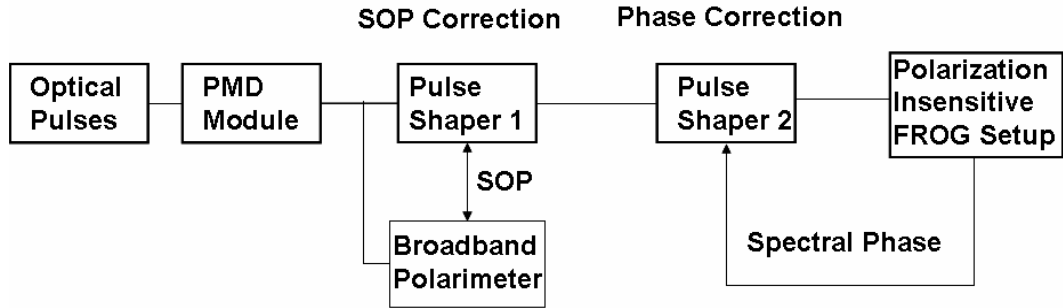


Fig. 3.19 Experimental setup for all-order PMD compensation.

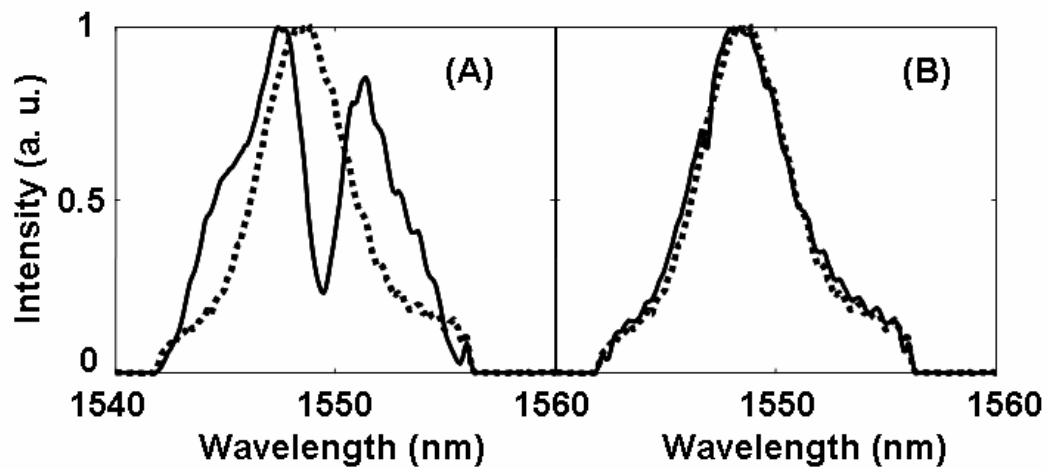


Fig. 3.20 Spectra before (A) and after (B) SOP correction. Solid: with PMD; dotted: without PMD.

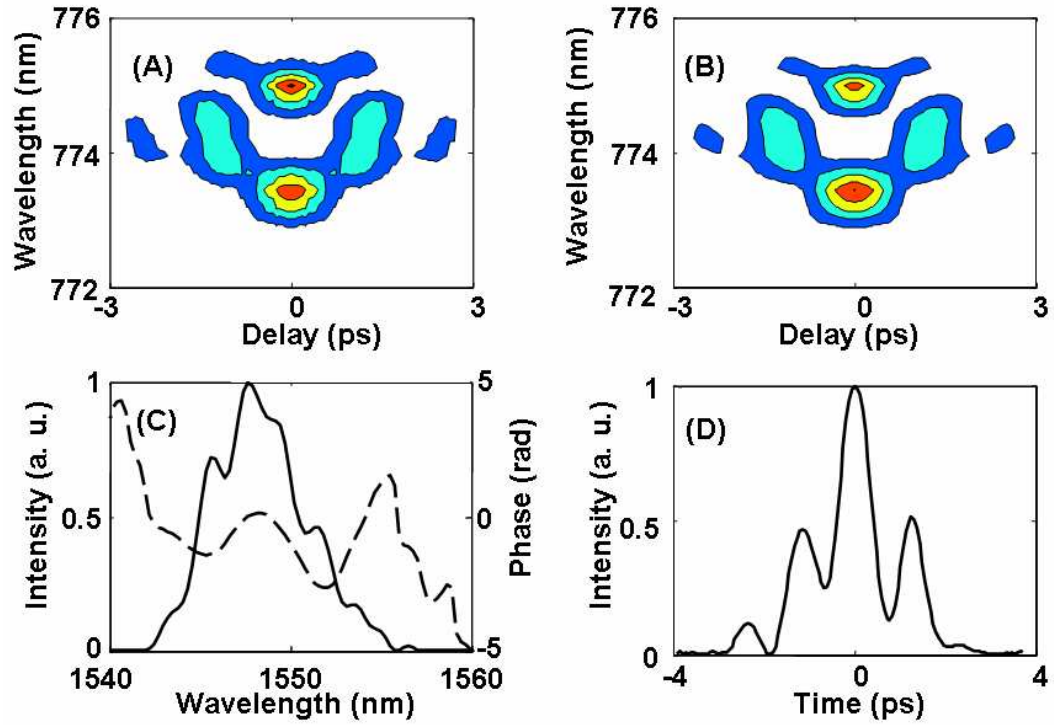


Fig. 3.21 FROG data of optical pulses after SOP correction but before spectral phase correction. (A) Measured FROG trace. (B) Retrieved FROG trace. (C) Retrieved spectral intensity (solid) and phase (dashed) profiles. (D) Retrieved temporal intensity profile.

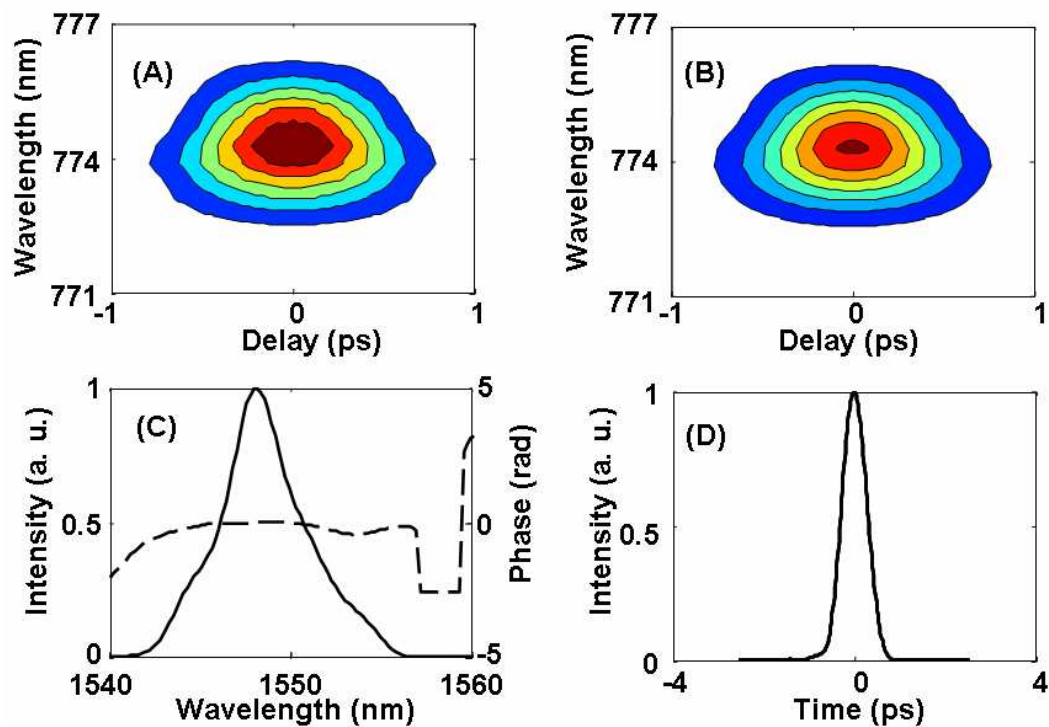


Fig. 3.22 FROG data of optical pulses after SOP and spectral phase correction. (A) Measured FROG trace. (B) Retrieved FROG trace. (C) Retrieved spectral intensity (solid) and phase (dashed) profiles. (D) Retrieved temporary intensity profile.

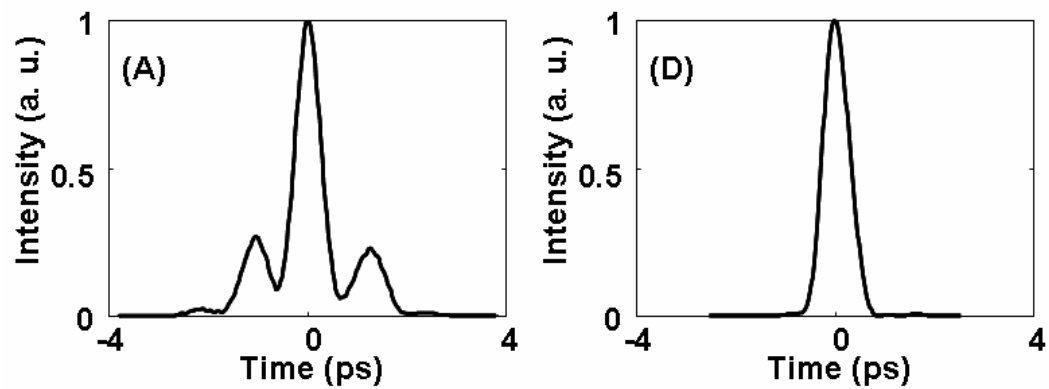


Fig. 3.23 Pulses before (A) and after (B) spectral phase correction.

4. ALL-ORDER PMD COMPENSATION VIA WAVELENGTH- PARALLEL JONES MATRIX SENSING AND CORRECTION

In the last chapter, we summarized the previous PMD compensation work, and reported our efforts to improve the performance of the previous PMD compensation system. However, the phase measurement remains a limit for the PMD compensation work. It generally takes several minutes and the measurement accuracy depends strongly on the complexity of the distorted pulses, which lacked the robustness that will be needed for real application. Furthermore, the compensation is dependent on the input SOP, which means that fluctuations of the input SOP will result in pulse distortion after the compensator is set, even the system PMD remains the same. In this chapter, we introduce a completely new PMD compensation idea, which is based on the wavelength-parallel Jones matrix sensing and correction. We report broadband all-order PMD compensation achieved by using a grating based transmission pulse shaper.

4.1 All-Order PMD Compensation Idea

In the absence of polarization dependent loss or gain (PDL or PDG), the frequency dependent Jones matrix of a fiber link are given in the Caley/Klein form [5], $U_f = \begin{bmatrix} \cos \theta e^{j\phi} & \sin \theta e^{j\psi} \\ -\sin \theta e^{-j\psi} & \cos \theta e^{-j\phi} \end{bmatrix}$, where θ , ϕ and ψ are frequency dependent angles. By measuring the output SOPs of two known input SOPs (for example 0° and 45°) with a wavelength-parallel polarimeter [19], one can solve for θ , ϕ and ψ analytically (The details of Jones matrices characterization have been discussed in chapter 2). The inverse of the Jones matrix can be written as the product of three elementary rotation matrices,

$$U_f^{-1} = \begin{bmatrix} \exp(-j\theta_3) & 0 \\ 0 & \exp(j\theta_3) \end{bmatrix} \begin{bmatrix} \cos \theta_2 & -j \sin \theta_2 \\ -j \sin \theta_2 & \cos \theta_2 \end{bmatrix} \begin{bmatrix} \exp(-j\theta_1) & 0 \\ 0 & \exp(j\theta_1) \end{bmatrix}, \quad (4.1)$$

where, $\theta_1 = (\phi + \psi)/2 + \pi/4$, $\theta_2 = -\theta$, and $\theta_3 = (\phi - \psi)/2 - \pi/4$. To realize wavelength-parallel Jones matrix correction, we apply pulse shaping (in a transmission geometry)

techniques to spread different frequency components spatially and use 4 LCM layers to apply the three elementary rotation matrices. Each LCM layer functions as a linear retarder array (128 pixels) with fixed fast axis and arbitrarily adjustable retardance. The orientations of the 4 LCM layers are 0° , 45° , 0° , and 90° , respectively. The Jones matrix of a 0 degree oriented LCM layer is $\begin{bmatrix} e^{j\varphi} & 0 \\ 0 & 1 \end{bmatrix}$. We operate the first three LCM layers (0° - 45° - 0°) to produce the three elementary rotation matrices on the right side of Eq. (4.1). After the operation for Jones matrix inversion, an isotropic spectral phase of $-(\theta_1 + \theta_2 + \theta_3)$ remains. To correct this residual phase, we apply an additional phase to the third and fourth LCM layers and program them in common-mode, which results in a polarization-insensitive phase-only modulation functionality. Note, the third LCM layer is programmed for the superposition of the differential phase from Eq. (4.1) for Jones matrix inversion and the common-mode residual phase correction. After the above operation, the frequency dependent Jones matrix is corrected to an identical matrix, and the PMD effects are compensated to all order.

4.2 Numerical Simulations of the New All-Order PMD Compensation Idea

We first study the new all-order PMD compensation idea by numerical simulations. Fig. 4.1 shows the scheme of the simulation work. 1-ps (FWHM) Gaussian optical pulses centred at 1550 nm are used as the optical source. The polarization states of the input pulses are switched between 0° and 45° linear. The PMD effects of the optical fiber is simulated as a concatenation of 100 birefringent segments with randomly oriented fast axes (uniform distribution between 0 and 2π). The DGDs of the birefringent segments form a uniform distribution between $1\pm 1\%$ the mean value. The frequency dependent output SOPs corresponding to the two input SOPs are calculated. Since in real experiments, there are errors in SOP sensing, we add random Gaussian noise with 0 mean and 5° standard deviation to the calculated output SOPs. The frequency dependent Jones matrix of the fiber link is estimated with the resulted output SOPs. The pulse shaper consists of a pair of 900 lines/mm gratings, a pair of lens with 1m focal length and a four-layer LCM with 0° , 45° , 0° , and 90° fast axes. The input beam diameter is 12.5 mm (at $1/e^2$). Each LCM layer has 128 independently controllable pixels with a pixel spacing of 100 μm . All the parameters of the pulse shaper are according to our experimental setup that will be introduced in the next section. With these parameters, the spectral resolution

(defined as the covered frequency range between the centre of two adjacent pixels) of the pulse shaper is 11.77 GHz. The pulse shaper is controlled by the algorithm described in the last section. The pulses before and after PMD compensation are calculated.

The performance of the all-order PMD compensation system is mainly limited by the spectral resolution. The main purpose of the simulation work is to study the relation between the maximum mean DGD that can be compensated for with high quality and the spectral resolution.

We firstly simulate PMD compensation of a piece of fiber with mean DGD of ~ 5.2 ps. Fig. 4.2 shows the PMD distorted output SOPs corresponding to the two input SOPs of one of the simulation trials. The SOP curves connected with red lines are calculated output SOPs and those connected with black lines are the output SOPs with Gaussian noise. Fig. 4.3 shows the initial pulse, the PMD distorted pulse and the pulse after PMD compensation, and the wavelength-dependent DGD profile. The irregular variation of DGD versus wavelength indicates strong all-order PMD effects. The pulse is corrected from ~ 10 ps to close to the initial pulse after PMD compensation, which indicates good performance of the PMD compensation algorithm. We carried out the simulation more than 50 times, every time, good PMD compensation is achieved. Figs. 4.4 and 4.5 show four other PMD compensation examples. In these simulations, the product of the mean DGD and the spectral resolution is 0.061.

We then simulate PMD compensation of a piece of fiber with mean DGD of ~ 10.4 ps. Fig. 4.6 shows the PMD distorted output SOPs corresponding to the two input SOPs of one of the simulation trials. Compared to Fig. 4.2, the variations of SOPs versus wavelength are much stronger. Fig. 4.7 shows the initial pulse, the PMD distorted pulse and the pulse after PMD compensation, and the wavelength-dependent DGD profile. In this example, the pulse is corrected from more than 15 ps to close to the initial pulse after PMD compensation, which indicates good performance of the PMD compensation algorithm. Figs. 4.8 and 4.9 show four other PMD compensation examples. When the mean DGD is ~ 10.4 ps, sometimes the PMD compensation system works well, but sometimes high quality PMD compensation can not be achieved. In these simulations, the product of the mean DGD and the spectral resolution is 0.12.

The simulations indicates that the new PMD compensation algorithm is robust. The performance is mainly limited by the spectral resolution. A rough estimate, consistent with very high quality compensation, is that mean DGD should remain below 1/16 of the inverse of the spectral resolution.

4.3 Broadband All-Order PMD Compensation Experiments with a Specified Input SOP

In this section, we report all-order PMD compensation results with a known input SOP (0° linear). Fig 4.10 shows the experimental setup. A passively mode-locked fiber ring laser followed by a bandpass filter (FWHM: ~ 4 nm) is used to produce ~ 800 fs pulses with 50 MHz repetition rate and 1550 centre wavelength. We use a PC followed by a polarizer to align the SOP of the initial pulses to the horizontally linear state. Then we use a ferroelectric liquid crystal (FLC) retarder to switch the input SOP between horizontally linear and RHC polarization states. The switchable FLC retarder (quarter wave plate at 1550 nm) has two stable optic-axis orientations separated by approximately 45° . The switching time between two axes is ~ 70 microseconds. After that the pulses are launched into a PMD module, consisting of 3 homemade PMD emulators connected via PCs. The 3 PMD emulators consist of 8, 15 and 8 PM fiber segments spliced at various angles, respectively. The total length of the PM fibers is ~ 21.1 meters and the birefringence is 3.47×10^{-4} . The estimated mean DGD of the PMD module is ~ 5.5 ps. The output light is connected to a fiber pigtailed transmission pulse shaper incorporating a 4-layer LCM. The orientations of the 4 LCM layers are 0° , 45° , 0° , and 90° , respectively. We use a broadband non-polarizing cube beamsplitter to integrate the wavelength-parallel polarimeter to the pulse shaper for SOP sensing. We use cross correlation (the FWHM of the reference pulse: ~ 100 fs) to measure pulses before and after PMD compensation. The chromatic dispersion of the whole setup is precompensated before PMD compensation.

Fig 4.11 depicts the distorted output SOP spectra of one of the experimental trials after PMD module for the horizontally linear and RHC input SOPs on the Poincare sphere. The strong and irregular variation of the output SOPs with wavelength is indicative of strong wavelength dependence feature of Jones matrix (or equivalently, significant all-order PMD effects). Since, PMD introduce wavelength dependent SOP spectra, the temporal intensity profiles of the distorted pulses are polarization dependent. We use a polarizer to select two orthogonal polarization spectral slices (0° linear and 90° linear) and measure the temporal intensity profiles of the two spectra by using cross-correlation, respectively. The sum of the two profiles gives the overall intensity profile. We keep the FLC retarder stable to generate 0° input SOP during the cross-correlation measurements. Fig 4.12 shows the distorted pulses (A) and the restored pulses (B) after PMD compensation. The peak intensity of the restored pulse at 0° linear SOP is normalized to 1. The pulse is distorted to more than 10 ps by all-order PMD effects and

the two polarization slices of the distorted pulse have close energy. After PMD compensation, the pulse is compressed dramatically to 856 fs (FWHM), close to bandwidth-limited. The pulse energy at 0° linear polarization state is far greater than that at 90° , which indicates that the restored pulse is close to single polarization and the PMD compensation algorithm reserves the input SOP.

Since the input SOP is switched for Jones matrix sensing, it is essential for the PMD compensator to work for any input SOP. To demonstrate it, we measure the intensity profile of the restored pulse (corresponding to Fig. 4.12 (B)) while keeping the FLC retarder switching at a rate of ~ 20 Hz. Since the cross-correlation measurement is polarization sensitive (in general the SHG is strongly polarization dependent) and the polarization switching period is on the order of the measurement integration time (30 ms in this experiment), it is necessary to employ polarization insensitive measurement technique, which is described in details in Chapter 3. We achieve polarization insensitive cross-correlation measurement by scrambling the SOP after the PMD compensation with a rate much faster than the measurement integration time by using a polarization scrambler (General Photonics Corporation, PCD-104, scrambling rate: 700 KHz). Fig. 4.13 shows the measurement results. The measured FWHM of the restored pulse is 868 fs. The high quality compensation indicates that our PMD compensation technique is compatible with simultaneous real-time sensing and compensation.

By adjusting the PCs among the PMD emulators, we tried the experiments with more than 20 independent PMD profiles. Each time, after PMD compensation, we can compress the pulses to below 900 fs in duration. Figs. 4.14 and 4.15 show four other PMD compensation examples.

4.4 Broadband All-Order PMD Compensation Experiments with an Arbitrary Input SOP

In the above section, all-order PMD compensation was achieved with a specified input SOP, which requires stable SOP before the polarizer in Fig. 4.10. In this section, we introduce a modified PMD compensation algorithm, which works for arbitrary input SOP. The key idea is to correct the PMD-related frequency-dependent Jones matrix to a frequency-independent constant Jones matrix (instead of correcting it to an identical matrix as in the above section).

Since PMD is only related to the frequency dependence of the Jones matrix, all-order PMD compensation can be achieved by correcting the Jones matrix to a constant,

frequency-independent matrix. To characterize the frequency dependence of the Jones matrix, we sequentially transform the arbitrary input SOP to four different SOPs, launch them into the fiber link, and measure the output SOPs using our fast wavelength-parallel polarimeter technology. Then we select the two output SOP spectra whose relative angle is closest to 90° on the Poincare sphere. By associating one of the selected output SOP spectra with the 0° linear input SOP, and the normalized cross product of the two selected output SOPs with the 45° linear input SOP, one gets frequency dependent Jones matrix $U'_f = U_f U$, where U is a frequency independent matrix and U^{-1} transforms one of the selected input SOP to 0° linear state and the normalized cross product of the two selected input SOPs to 45° linear states. Note, it is necessary to make sure the angle between the two selected SOPs is close to 90° to avoid enlarging errors through the cross product operation. The inverse of U'_f ($U'_f = \begin{bmatrix} \cos \theta' e^{j\phi'} & \sin \theta' e^{j\psi'} \\ -\sin \theta' e^{-j\psi'} & \cos \theta' e^{-j\phi'} \end{bmatrix}$) can be written as the

product of three elementary rotation matrices,

$$(U'_f)^{-1} = \begin{bmatrix} \exp(-j\theta_3) & 0 \\ 0 & \exp(j\theta_3) \end{bmatrix} \begin{bmatrix} \cos \theta_2 & -j \sin \theta_2 \\ -j \sin \theta_2 & \cos \theta_2 \end{bmatrix} \begin{bmatrix} \exp(-j\theta_1) & 0 \\ 0 & \exp(j\theta_1) \end{bmatrix}, \quad (4.2)$$

where, $\theta_1 = (\phi' + \psi')/2 + \pi/4$, $\theta_2 = -\theta'$, and $\theta_3 = (\phi' - \psi')/2 - \pi/4$ and each of these angles is frequency-dependent. To achieve wavelength-parallel Jones matrix correction, we apply the same pulse shaping technique and algorithm as in sections 4.1 and 4.2, except that the Jones matrix U'_f (instead of the Jones matrix of the fiber link U_f as in previous sections) is corrected to an identical matrix. After such Jones matrix correction, PMD effects are compensated to all order. The output Jones vector after PMD compensation is a frequency independent transformation of the input Jones vector, $\vec{E}_{out} = U^{-1} \vec{E}_{in}$.

The experimental setup is the same as in Fig. 4.10, except that we use two FLC retarders at the input side (as shown in Fig. 4.16) to replace the previously used one polarizer and one FLC retarder. The two FLC retarders are used to switch the arbitrary input SOP among 4 states. (Note, we do not need to know the input SOP prior to the FLCs, as long as it is constant during each measurement cycle of ~ 200 ms, which should be easy to achieve at the transmitter). The orientations of the axes of the two FLCs are 0° (state 0)- 45° (state 1) and 45° (state 0)- 90° (state 1), respectively. Consequently, the SOP transformations are denoted by the combination of the FLC states as 00, 01, 10, 11. Simulation shows that for any input SOP, there are at least two FLC states yielding output

SOPs separated by an angle in the range between 60° and 120° on the Poincare sphere. This guarantees that Jones matrix characterization will be accurate enough.

Fig. 4.17 shows an example of four Poincare sphere plots (corresponding to the four FLC states) of SOP spectra distorted by PMD. The strong and irregular variation of the output SOPs versus wavelength is indicative of significant all-order PMD effects. The average angles between states 00-01, 00-10, 00-11, 01-10, 01-11, 10-11 are 89.2° , 107.9° , 107.2° , 159.4° , 108.9° and 59.0° . We first select the data from 00-01 states for control of our PMD compensator. As in the last section, we use a polarizer to sequentially select two orthogonal polarization spectral slices (0° linear and 90° linear) and measure the temporal intensity profiles corresponding to each polarization. For now we keep the FLC retarders stable (00 state) during the cross-correlation measurement. Fig. 4.18 (A) and (B) show the PMD distorted pulses and the restored pulses after PMD compensation. The peak intensity of the restored pulse at 0° linear SOP is normalized to 1. After compensation, the pulse is compressed dramatically from more than 10 ps (10% intensity) to 826 fs (FWHM). The output SOP of state 00 is corrected to 0° linear state as predicted in theory. As evidence, the intensity of the 90° component in Fig. 4.18 (B) is almost zero. To demonstrate the robustness of our PMD sensing/compensation system, we now repeat the experiment with identical PMD but using the data from the 10-11 FLC sensing states (the angle between which is even out of the $60^\circ\sim 120^\circ$ range). We keep the FLC retarders stable at the 10 state during the cross-correlation measurement. Fig. 4.18 (C) and (D) show the distorted and restored pulses. Again the pulse is compressed to 811 fs and the output SOP of state 10 is corrected to 0° linear state.

By adjusting the PC before the FLCs and the PCs among the PMD emulators, we then repeat the experiments with more than 10 independent PMD profiles and input SOPs. Each time, we can compress the pulses to a comparable ~ 800 fs duration after PMD compensation. Fig. 4.19 shows the distorted and restored pulses from one of these additional trials. The pulse is compressed to 828 fs. Figs. 4.20 and 4.21 show four other examples.

Again, the PMD compensation technique is compatible with simultaneous real-time sensing and compensation. To demonstrate this, we measure the intensity profiles of the restored pulses while keeping the sensing FLC retarders switching at a rate of ~ 20 Hz during the experimental trials of Fig. 4.18 and 4.19. We again employ the polarization insensitive cross-correlation technique for the measurement. Fig. 4.22 (A) and (B) show the restored pulses corresponding to Fig. 4.18 (B) and Fig. 4.19 (B), respectively. The

measured pulse FWHMs are 811fs and 823 fs respectively, confirming that the PMD compensation process is insensitive to changes in input SOP.

The spectral resolution of the polarimeter and pulse shaper used in sections 4.3 and 4.4 is 11.6 GHz. The product of the compensated mean DGD and the spectral resolution is 0.0638. Compared to the old PMD compensation system, we improved the compensated mean DGD more than 3 times (from ~ 1.5 ps to ~ 5.5 ps), the responding time from several minutes to under 1 second. Another important advantage of the new PMD compensation system is that it is insensitive to the changes in the input SOP.

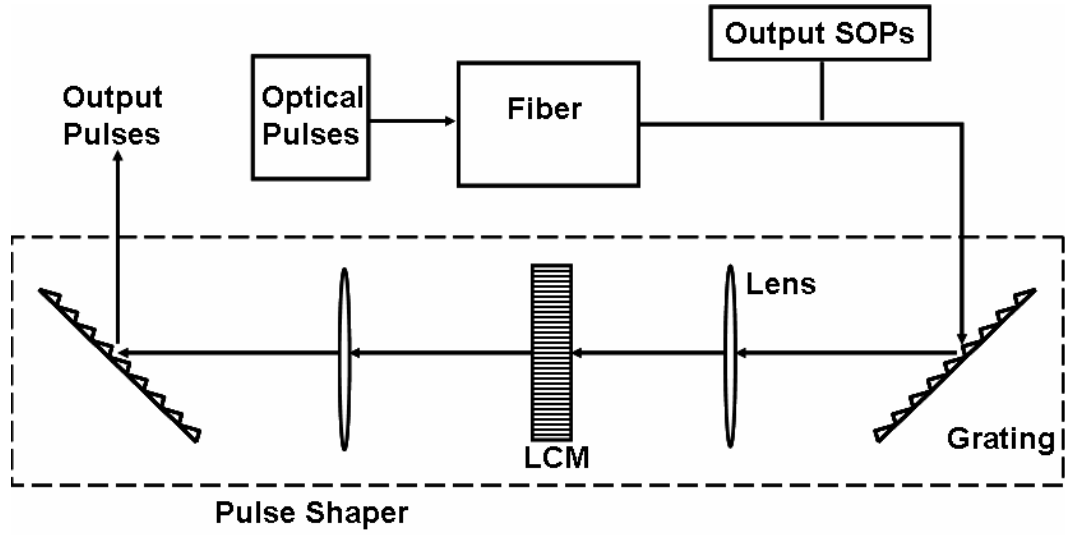


Fig. 4.1 Scheme for numerical simulations of all-order PMD compensation.

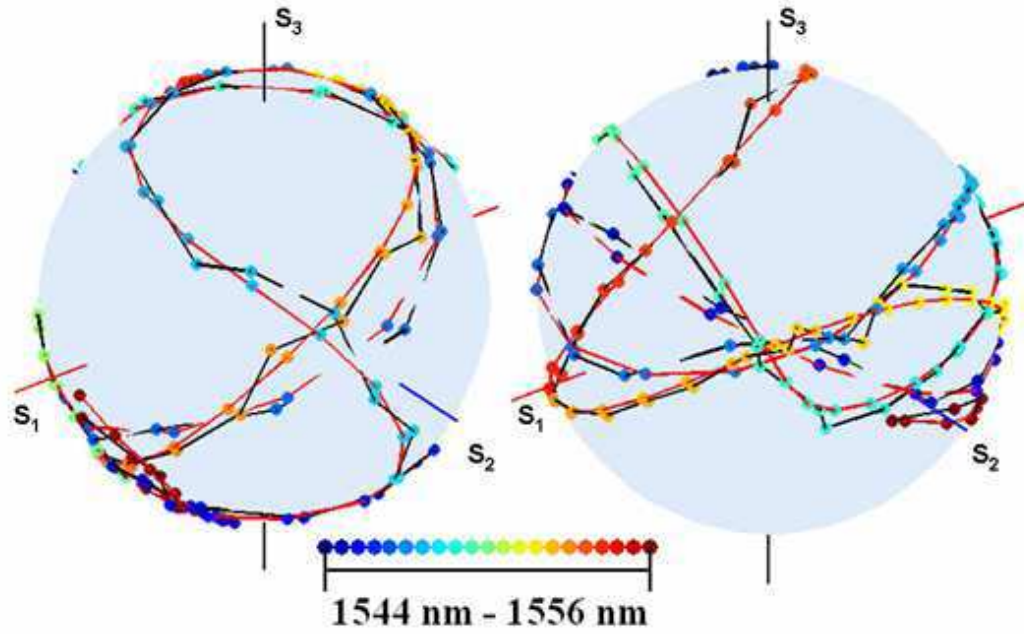


Fig. 4.2 Output SOPs corresponding to 0° (left) and 45° (right) linear input SOPs. Curves connected with red lines are calculated SOPs and curves connected with black lines are SOPs with random Gaussian noise.

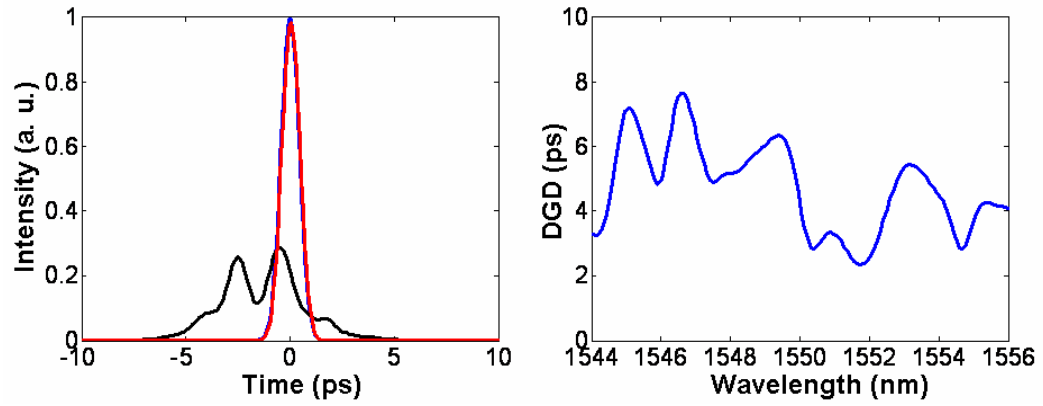


Fig. 4.3 Left: initial (blue), PMD distorted (black) and the restored after PMD compensation (red) optical pulses. Right: the wavelength dependent DGD profile.

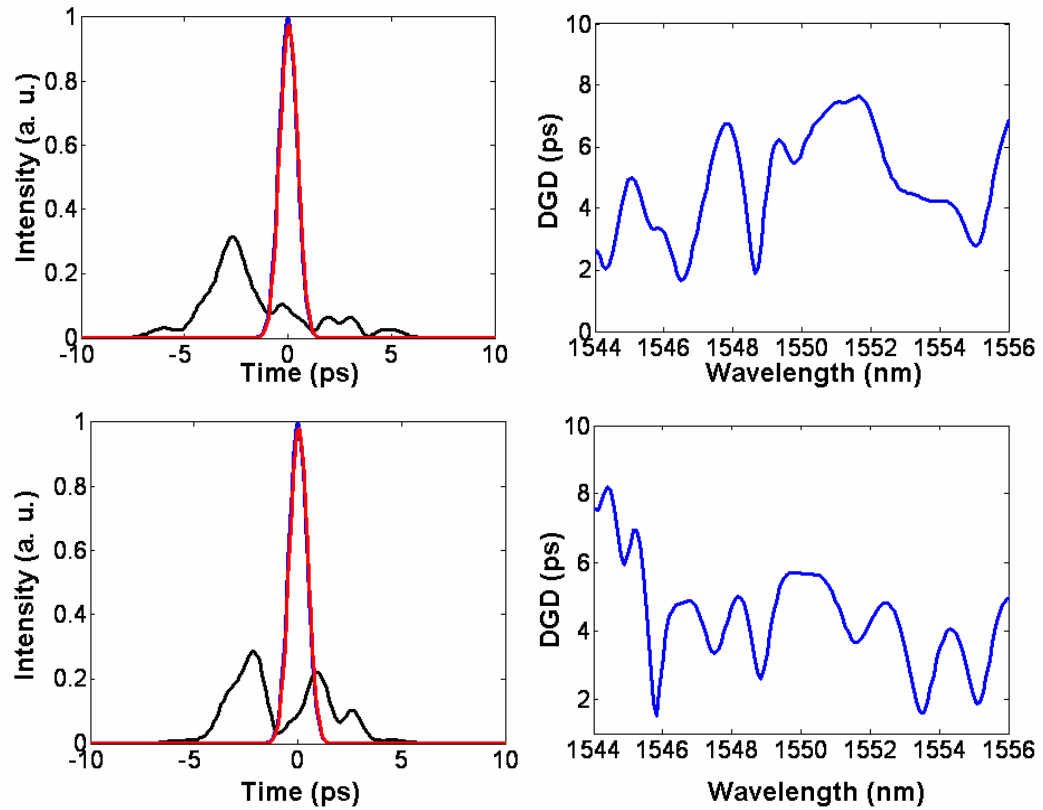


Fig. 4.4 Left: initial (blue), PMD distorted (black) and the restored after PMD compensation (red) optical pulses. Right: the wavelength dependent DGD profile.

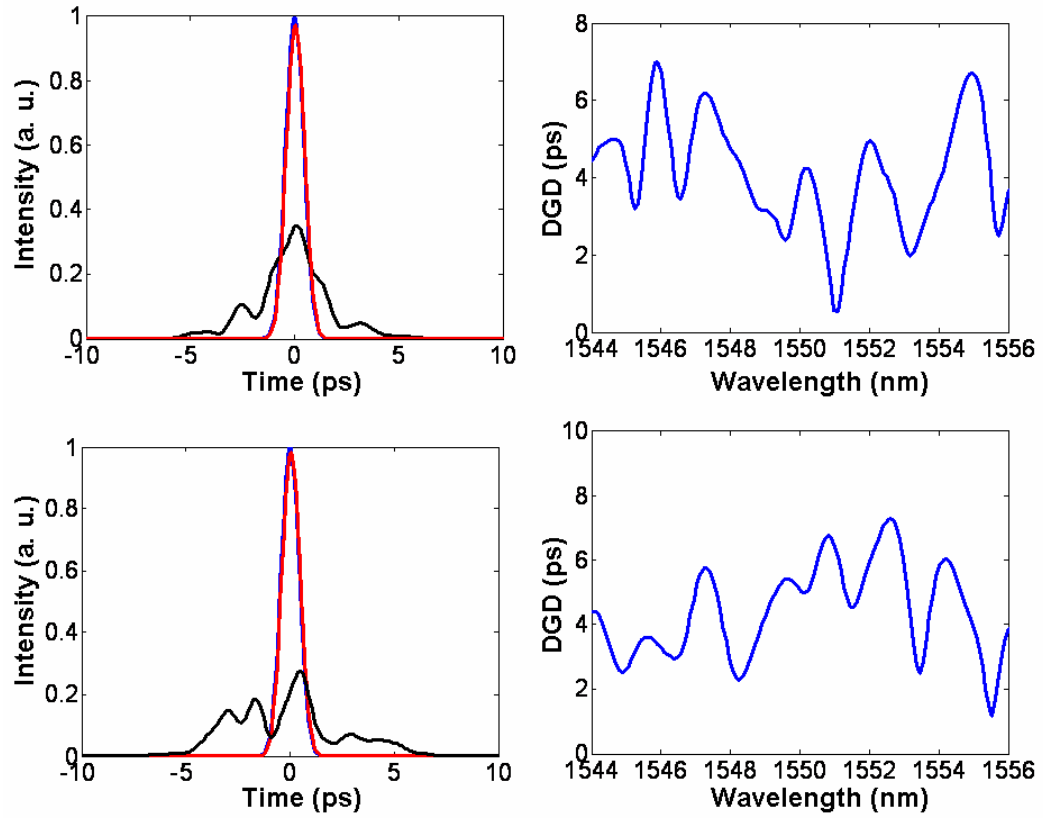


Fig. 4.5 Left: initial (blue), PMD distorted (black) and the restored after PMD compensation (red) optical pulses. Right: the wavelength dependent DGD profile.

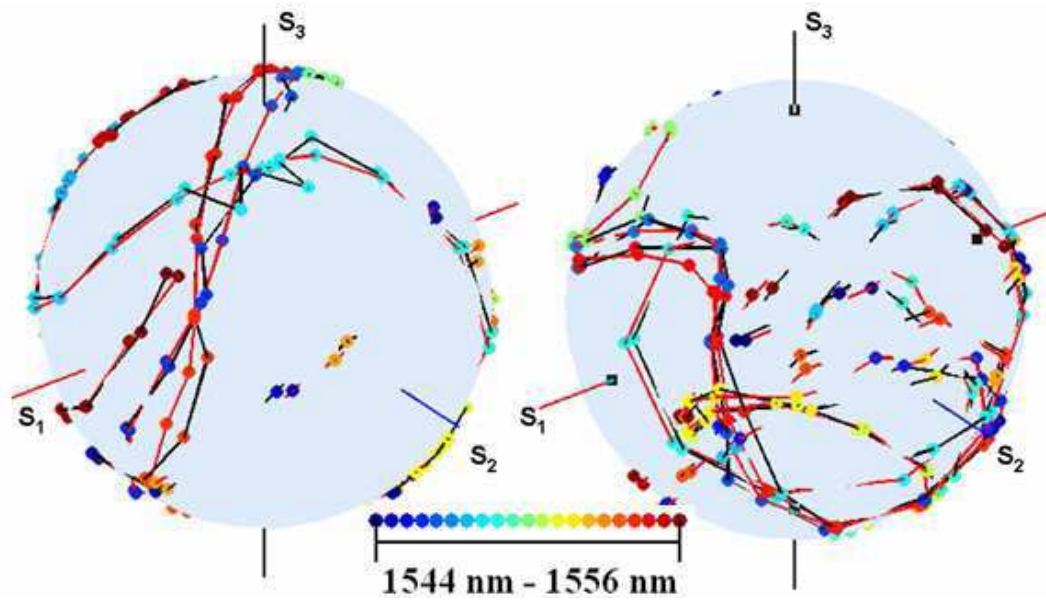


Fig. 4.6 Output SOPs corresponding to 0° (left) and 45° (right) linear input SOPs. Curves connected with red lines are calculated SOPs and curves connected with black lines are SOPs with random Gaussian noise.

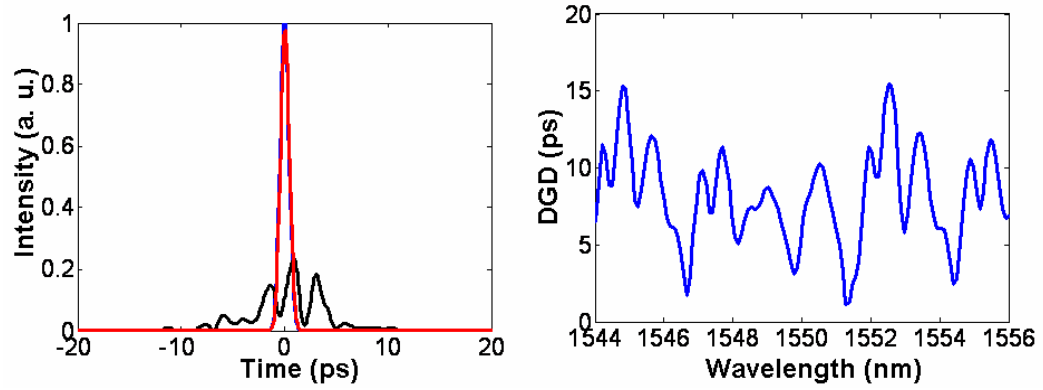


Fig. 4.7 Left: initial (blue), PMD distorted (black) and the restored after PMD compensation (red) optical pulses. Right: the wavelength dependent DGD profile.

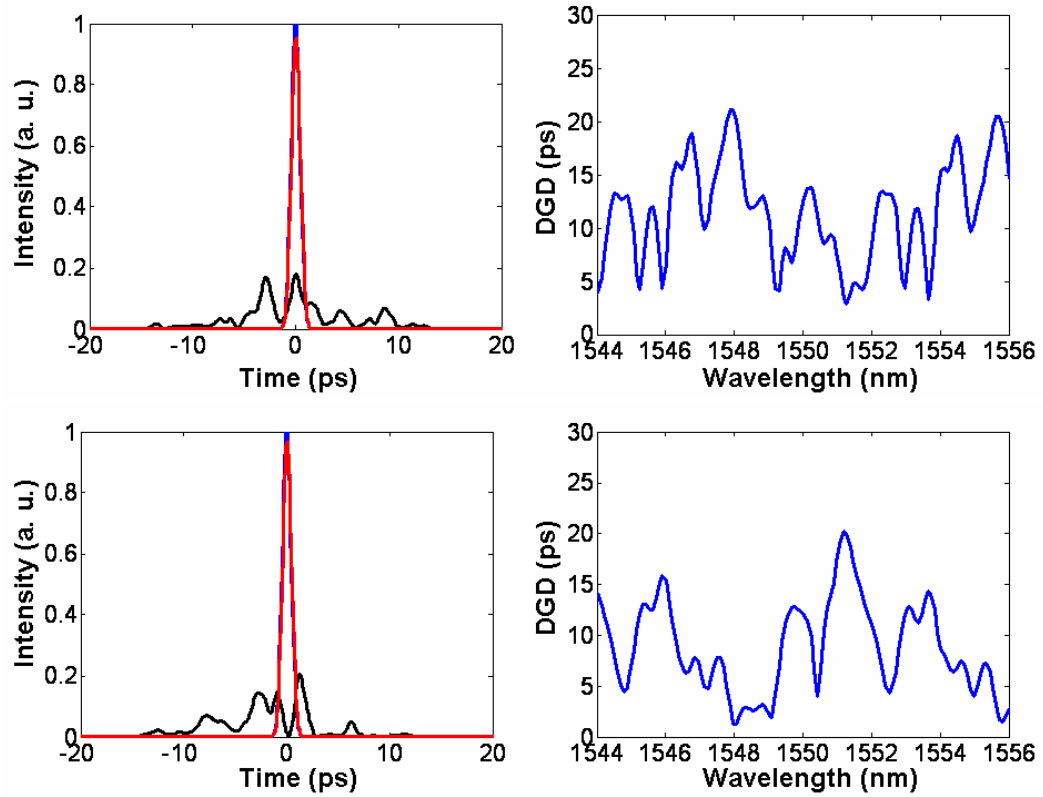


Fig. 4.8 Left: initial (blue), PMD distorted (black) and the restored after PMD compensation (red) optical pulses. Right: the wavelength dependent DGD profile.

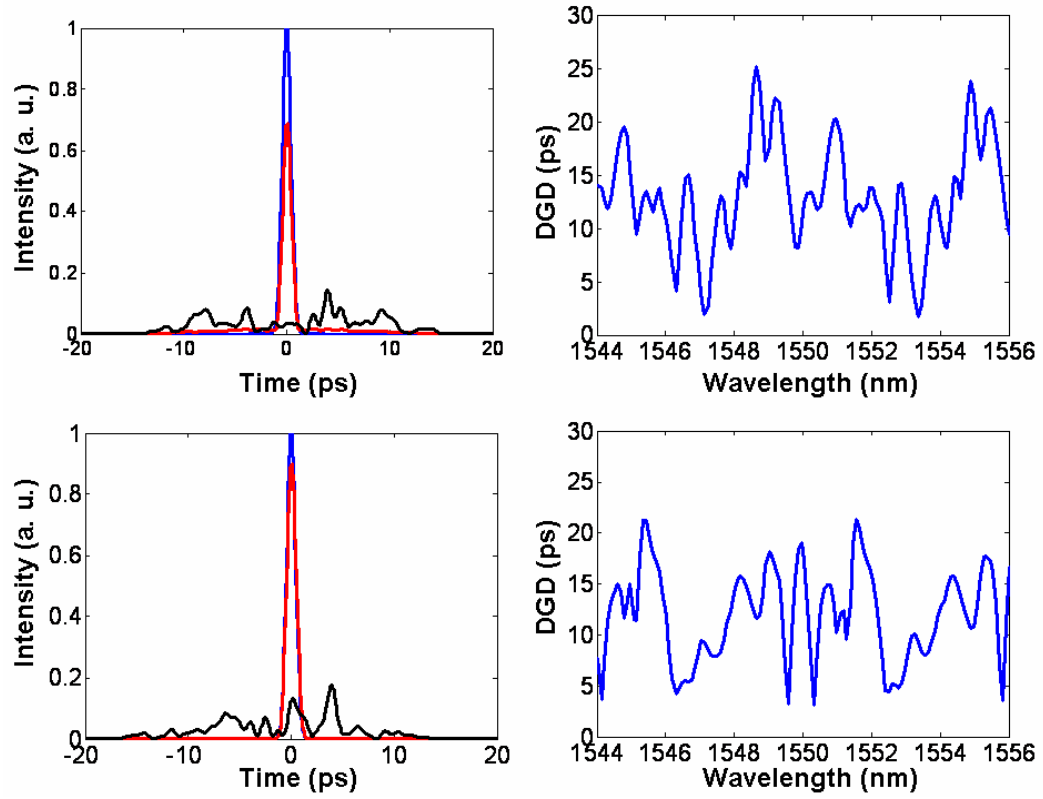


Fig. 4.9 Left: initial (blue), PMD distorted (black) and the restored after PMD compensation (red) optical pulses. Right: the wavelength dependent DGD profile.

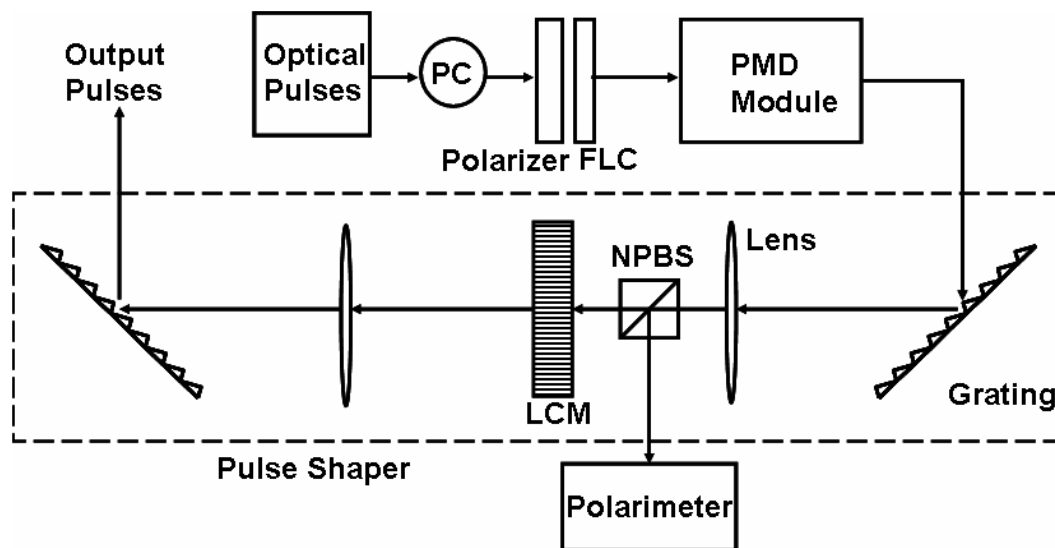


Fig. 4.10 Experimental setup for broadband all-order PMD compensation with a specified input SOP. PC: polarization controller; FLC: ferroelectric liquid crystal; NPBS: non-polarizing beam splitter; LCM: liquid crystal modulator.

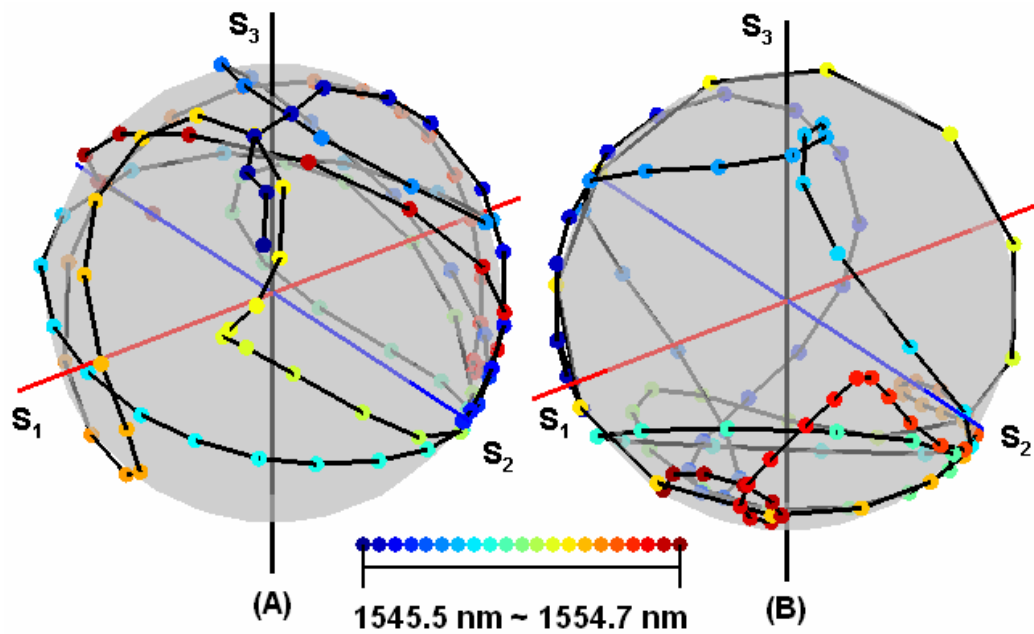


Fig. 4.11 (A) Output SOP spectrum for horizontally linear input SOP; (B) output SOP spectrum for RHC input. Each point corresponds to a measured SOP vector at a specified wavelength. Solid lines are used to connect SOP vectors at adjacent wavelength.

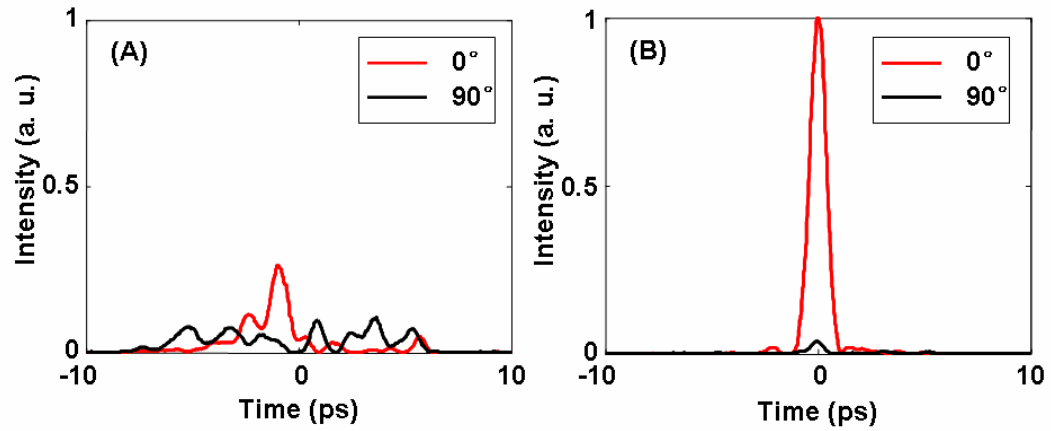


Fig. 4.12 (A) Distorted pulses measured at orthogonal polarization states. (B) Restored pulses after PMD compensation.

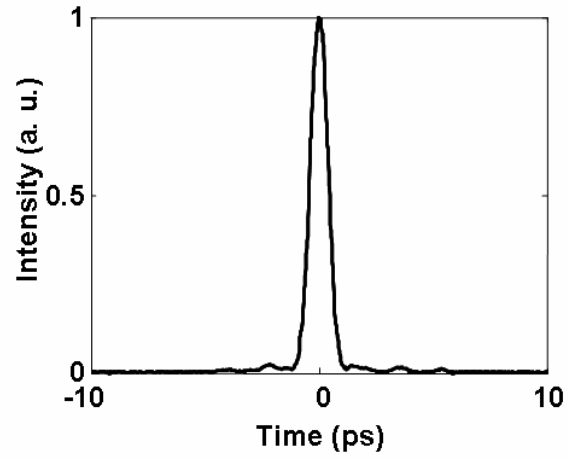


Fig. 4.13 Restored pulse (corresponding to Fig. 4.12. (B)) measured via polarization insensitive cross-correlation while keeping the input SOP switching.

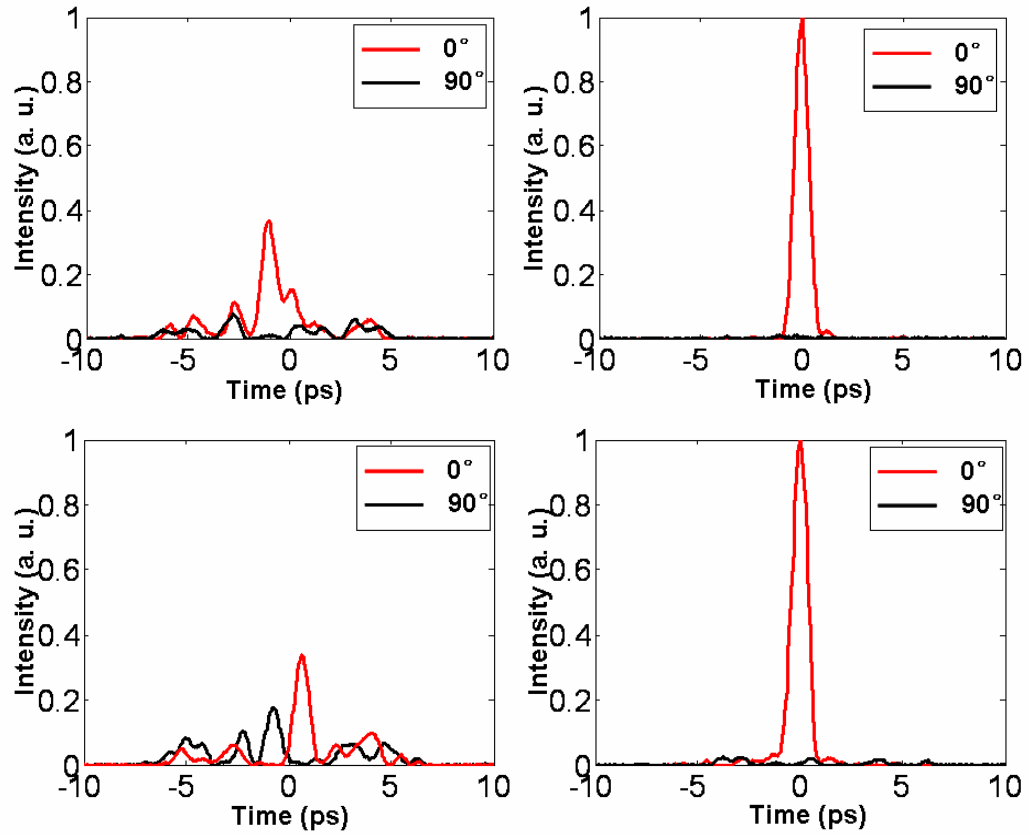


Fig. 4.14 Left Column: distorted pulses measured at orthogonal polarization states. Right column: Restored pulses after PMD compensation.

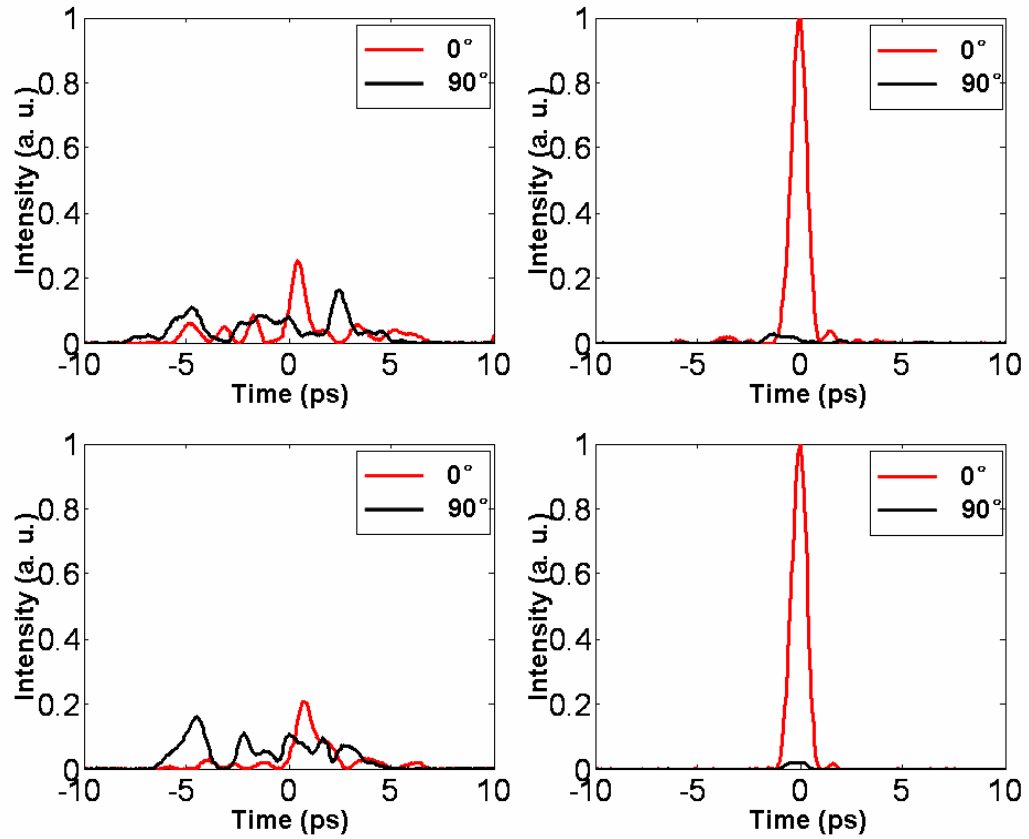


Fig. 4.15 Left Column: distorted pulses measured at orthogonal polarization states. Right column: Restored pulses after PMD compensation.

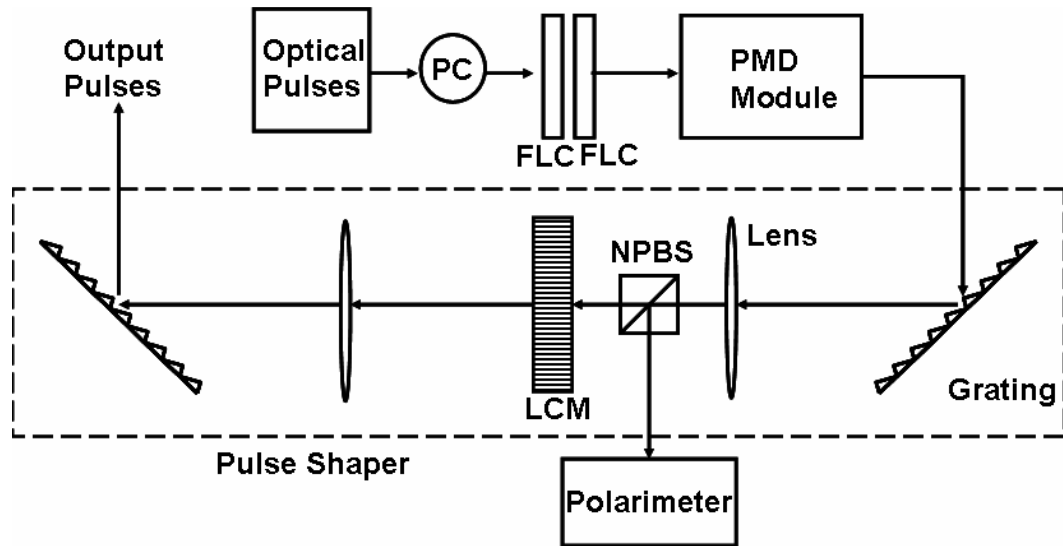


Fig. 4.16 Experimental setup for all-order PMD compensation with an arbitrary input SOP. PC: polarization controller, FLC: ferroelectric liquid crystal, NPBS: non-polarizing beam splitter, LCM: liquid crystal modulator.

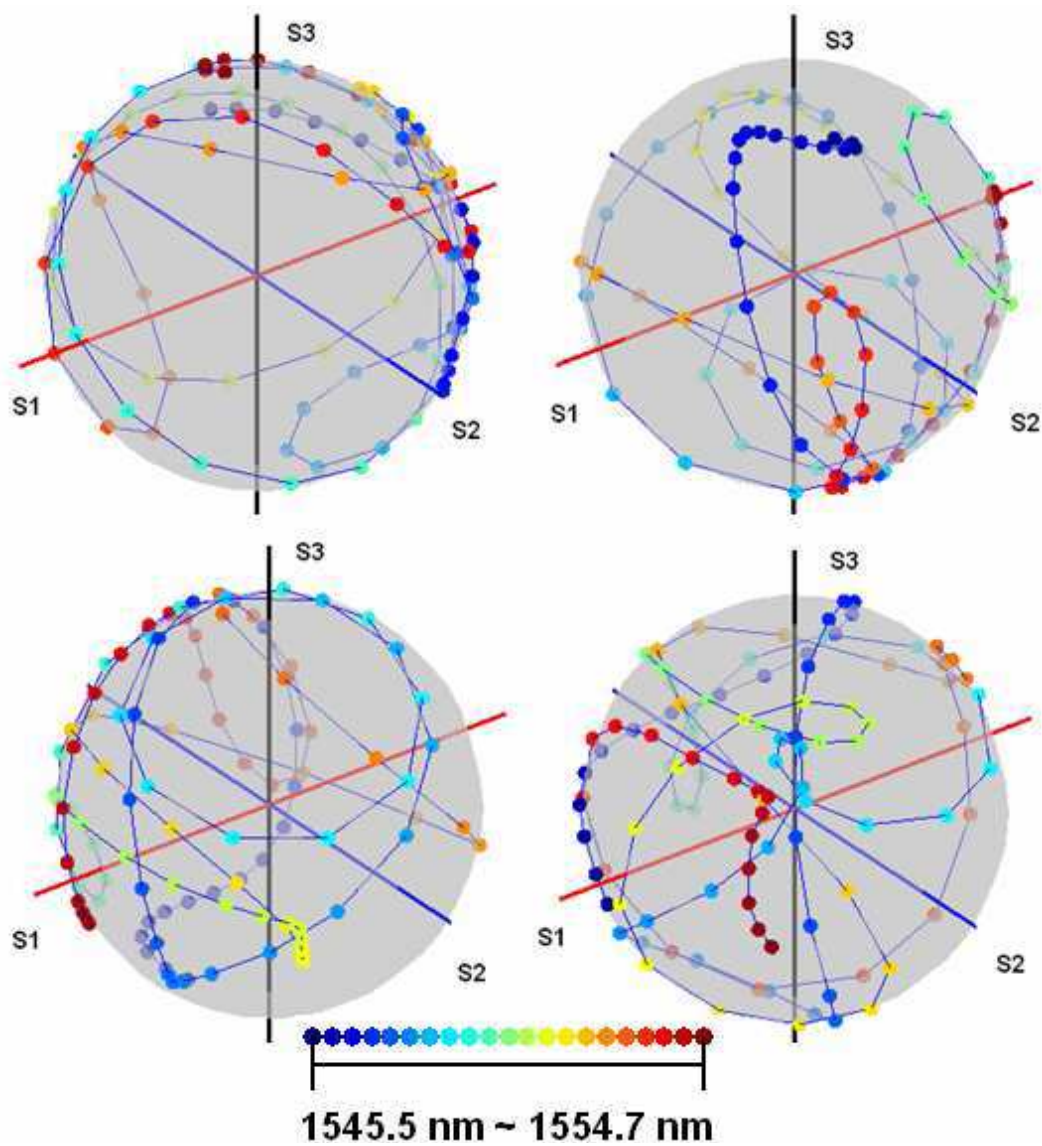


Fig. 4.17 Output SOP spectra corresponding to the 4 FLC states 00, 01, 10 and 11. Each point corresponds to a measured SOP vector at a specified wavelength, SOP vectors at adjacent wavelength are connected via solid lines.

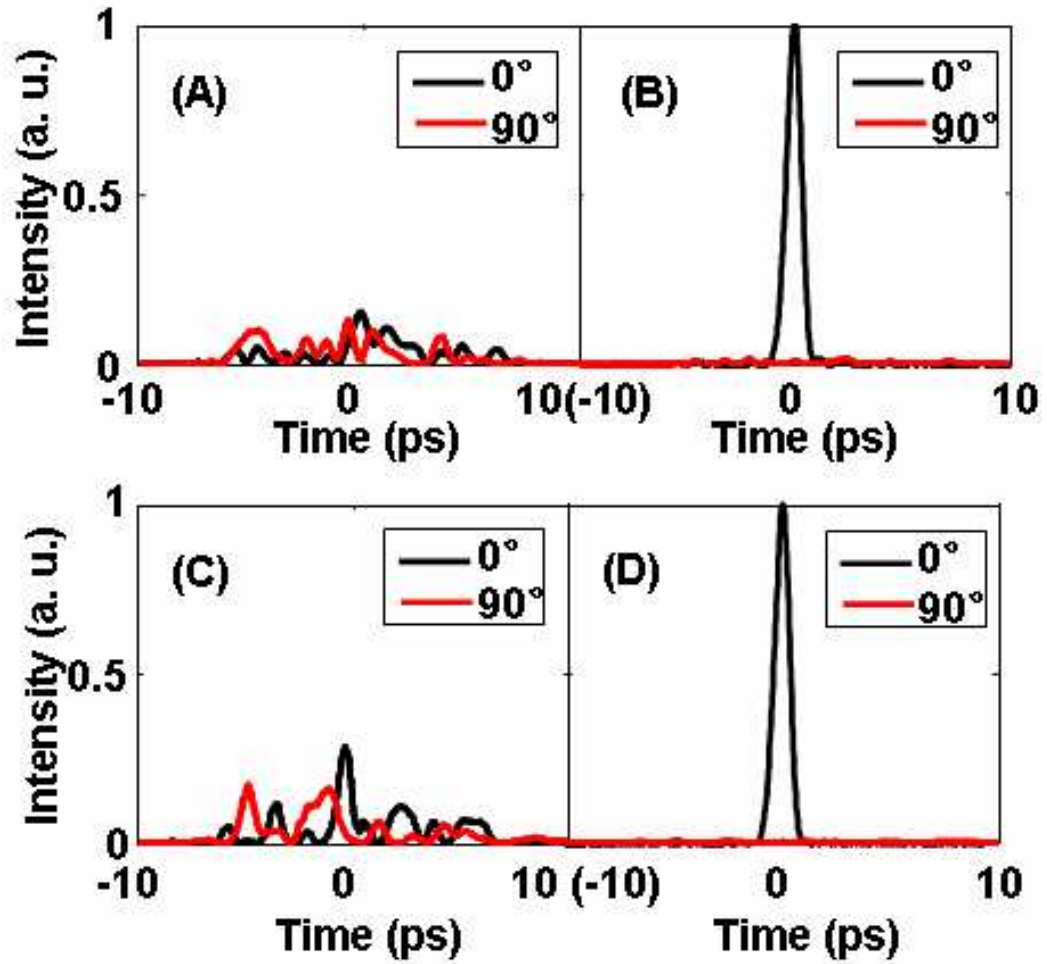


Fig. 4.18 (A) and (B) Distorted and restored pulses when 00-01 states are selected for PMD compensation process. (C) and (D) Distorted and restored pulses when 10-11 states are selected for PMD compensation process.

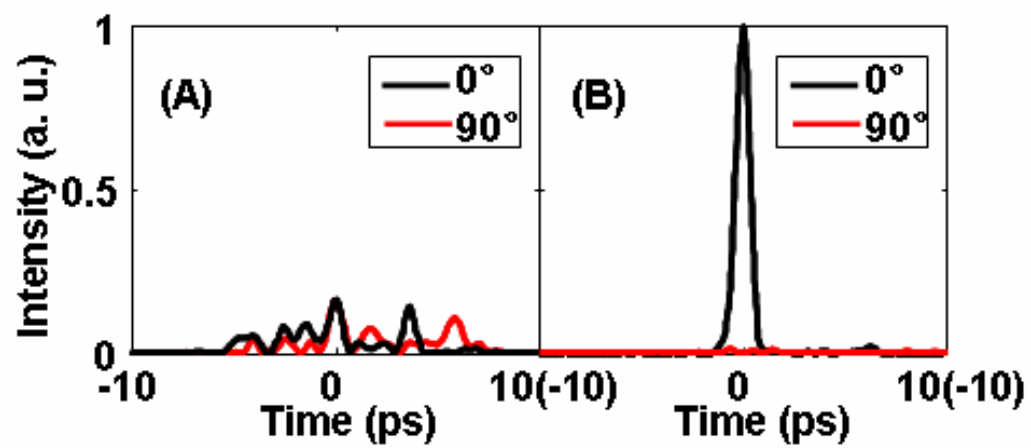


Fig. 4.19 Distorted and restored pulses.

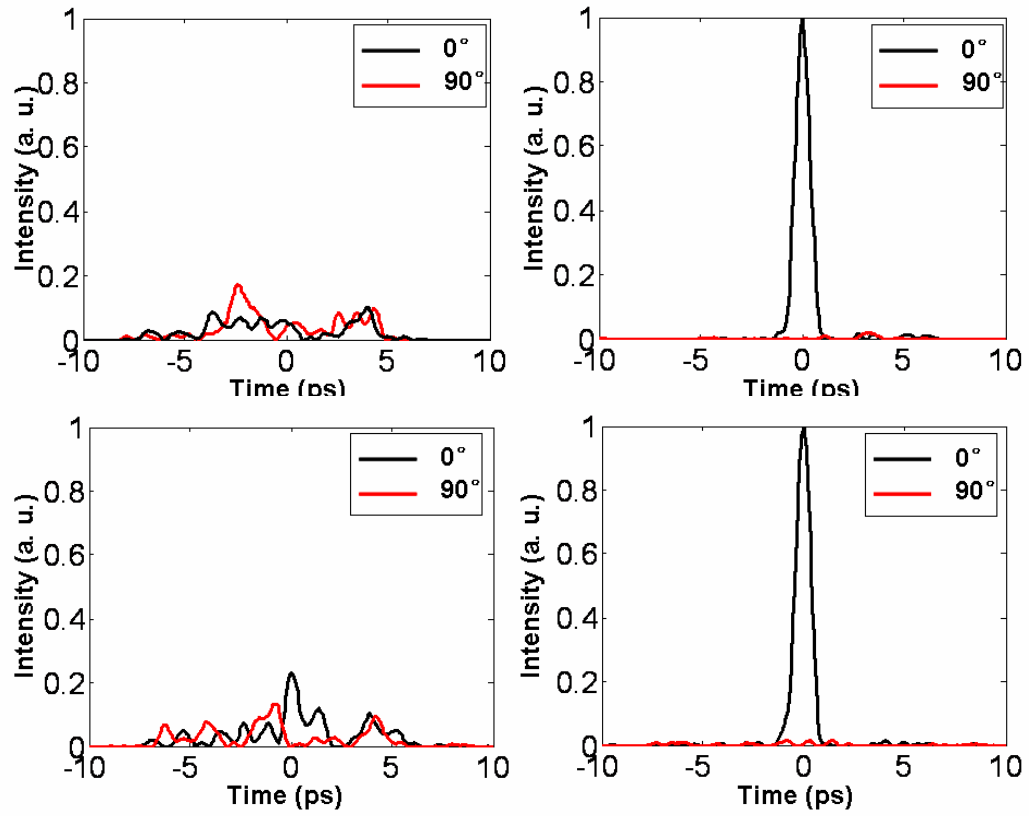


Fig. 4.20 Left Column: distorted pulses measured at orthogonal polarization states. Right column: Restored pulses after PMD compensation.

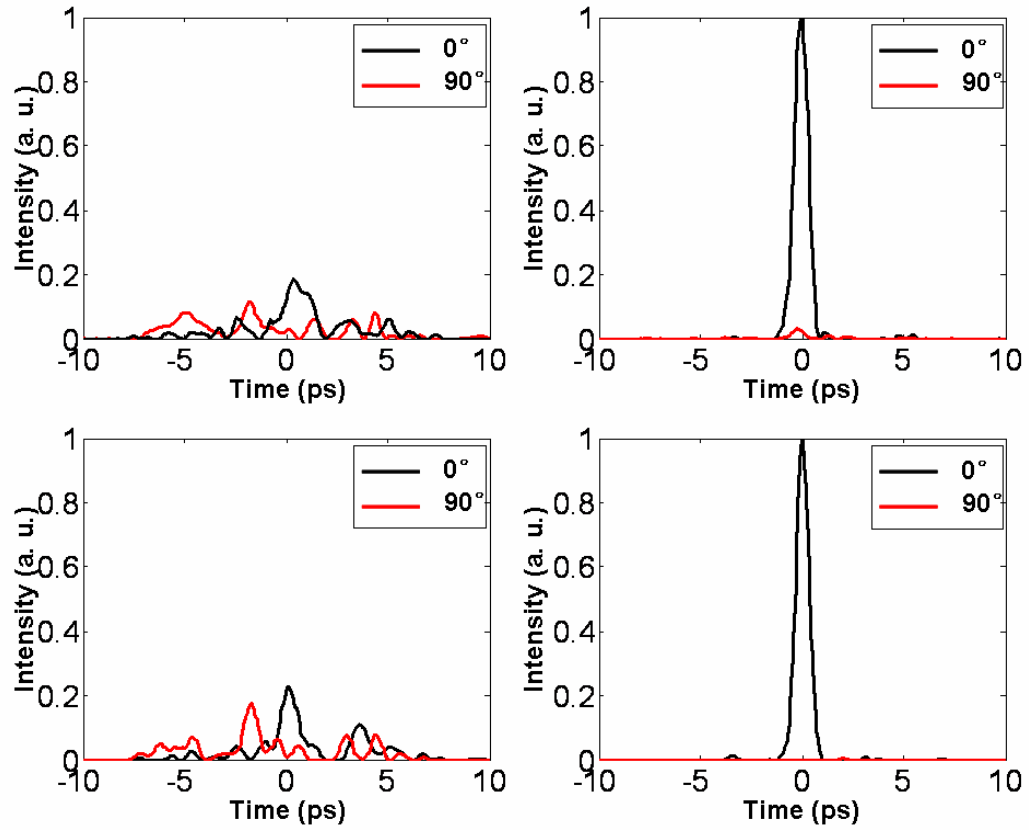


Fig. 4.21 Left Column: distorted pulses measured at orthogonal polarization states. Right column: Restored pulses after PMD compensation

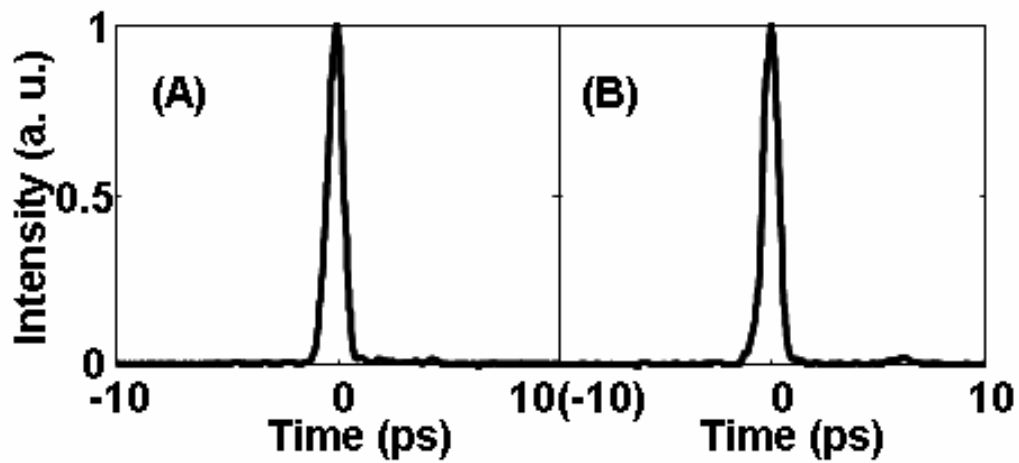


Fig. 4.22 Restored pulses corresponding to Fig. 4.18 (B) and Fig. 4.19 (B), measured with polarization insensitive cross correlation while the FLC retarders kept switching.

5. ALL-ORDER PMD COMPENSATION VIA A VIPA BASED PULSE SHAPER

In the last chapter, we reported broadband all-order PMD compensation results achieved with grating based wavelength-parallel polarimeter and pulse shaper. The mean DGD compensated in those experiments was ~ 5.5 ps, and the sensing element and control element spectral resolutions corresponded to ~ 11.6 GHz. These parameters are appropriate for future high bit rates systems (e.g., 640 Gb/s), but not for 40 Gb/s systems where we are interested in mean DGDs of several tens of picoseconds for all-order compensation experiments. In this chapter, we introduce VIPA based polarimeter and pulse shaper with control element spacings corresponding to only 1.6 GHz for wavelength-parallel Jones matrix sensing and correction. We demonstrate full compensation of ~ 15 ps optical pulses, distorted by all-order PMD effects to more than 100 ps, by using a VIPA based transmission pulse shaper. The results demonstrate the feasibility of scaling our all-order PMD compensation concept to optical bandwidths consistent with near-term lightwave communications rates.

The PMD compensation concept here is the same as that in section 4.4. Fig. 5.1 shows the experimental setup. A passively mode-locked fiber ring laser followed by a bandpass filter (~ 40 -GHz FWHM) and an EDFA is used to produce ~ 15 ps pulses with 50 MHz repetition rate and 1550.7 nm center wavelength. Another bandpass filter with 4-nm FWHM is used to filter out the ASE noise introduced by the EDFA. Although its use is not required, a PC is available for arbitrary adjustment of the input SOP. We use two switchable FLC retarders to switch the input SOP among 4 different SOP states (same as in Chapter 4.3). The orientations of the axes of the two FLCs are 0° (state 0)- 45° (state 1) and 45° (state 0)- 90° (state 1), respectively. Consequently, the SOP transformations are denoted by the combination of the FLC states as 00, 01, 10, 11. The signal is then connected to the PMD module consisting of 3 homemade PMD emulators connected via PCs. The 3 PMD emulators consist of 5, 8 and 6 PM fibers spliced at various angles, with an overall estimated mean DGD of 42 ps. The distorted signal is launched into a VIPA

based transmission pulse shaper incorporating a 4-layer LCM for PMD compensation. The orientations of the LCM layers are $0^\circ - 45^\circ - 0^\circ - 90^\circ$, respectively. The free spectral ranges (FSR) of the VIPAs are 200 GHz and the incident angle to the VIPA is $\sim 2.5^\circ$. A flipper mirror is used to integrate the wavelength-parallel polarimeter to the pulse shaper. For simultaneous SOP sensing and PMD compensation, one can use a non-polarizing beam splitter to direct part of the light into the polarimeter as demonstrated in Chapter 4. A 50 GHz fast photo detector and a sampling oscilloscope are used to directly observe the distorted and restored pulses.

Fig. 5.2 shows an example of four Poincare sphere plots (corresponding to the four FLC states) of SOP spectra distorted by PMD. The average angles between states 00-01, 00-10, 00-11, 01-10, 01-11, 10-11 are 10.9° , 100.2° , 111.8° , 105.4° , 101.4° and 120.2° . We first select the data from 00-10 states for control of our PMD compensator. Fig. 5.3 shows the temporal intensity profiles (average trace over 128 data sets) of the optical pulses before and after PMD compensation. The peak intensity of the pulse after compensation is normalized to 1. The pulse without PMD effects is plotted with the restored pulse in Fig. 5.3 (B) for comparison. After compensation, the pulse is compressed from more than 100 ps (10% intensity) to ~ 15 ps (FWHM). Compared to the initial pulse, almost perfect compensation has been achieved. To demonstrate the robustness of our PMD sensing/compensation system, we now repeat the experiment with identical PMD but using the data from the 10-11 FLC sensing states (the angle between which is $\sim 120^\circ$). Fig. 5.4 shows the restored pulse together with the initial pulse (the distorted pulse is the same as in Fig 5.3 (A)). Again, perfect compensation has been achieved. During the above measurement, the FLC retarders at the input side are held in a stable state.

By adjusting the PC at the input side and the PCs among the PMD emulators, we tried the experiments with more than 10 independent PMD profiles. Each time, after PMD compensation, we can compress the pulses to ~ 15 ps in duration, without any apparent distortion. Fig. 5.5 shows the distorted and restored pulses of another PMD compensation trial. Figs. 5.6 and 5.7 show four other examples.

As in Chapter 4, the PMD compensation technique is compatible with simultaneous real-time sensing and compensation because once the compensator is set, it works for any input SOP. Here we more critically study the transient effects of the FLC retarders by looking at persistent traces of the distorted and restored pulses while keeping the FLCs switching. Fig. 5.8 shows the measured persistent traces corresponding to Fig. 5.3. Fig. 5.8 (A) shows the initial pulse while the FLC is kept stable. Fig. 5.8 (B) shows

the PMD distorted pulse while the FLC is switching at a rate of 20 Hz. Two stable states are clearly depicted. Fig. 5.8 (C) shows the distorted pulse while the FLC switching at a rate of 2 kHz. Transient effects between the two stable states are clearly displayed. Fig. 5.8 (D) shows the restored pulse after PMD compensation (corresponding to Fig. 5.3 (B)) while the FLC kept switching at a rate of 2 kHz. The restored pulse is very close to the initial pulse, except that there is a $\sim 5\%$ power fluctuation at the peak. We attribute this fluctuation to transient loss introduced by the FLC retarders (we see the same fluctuation for the initial undistorted pulse when the FLC retarders are kept switching). Based on ~ 10 experimental trials, we did not see any other degradation induced by FLC switching except these small power fluctuations. These data provide evidence of the feasibility of continuous in-line sensing based on switching of the launching polarization.

Note, the amount of PMD that can be accurately sensed and fully compensated is only limited by the resolution of the polarimeter and of the pulse shaper. A rough estimate (section 4.2), consistent with very high quality compensation, is that mean DGD should remain below $1/16$ of the inverse of the spectral resolution. In the current experiment with ~ 42 ps mean DGD, we are approximately at this limit, which should be sufficient to handle most long haul systems.

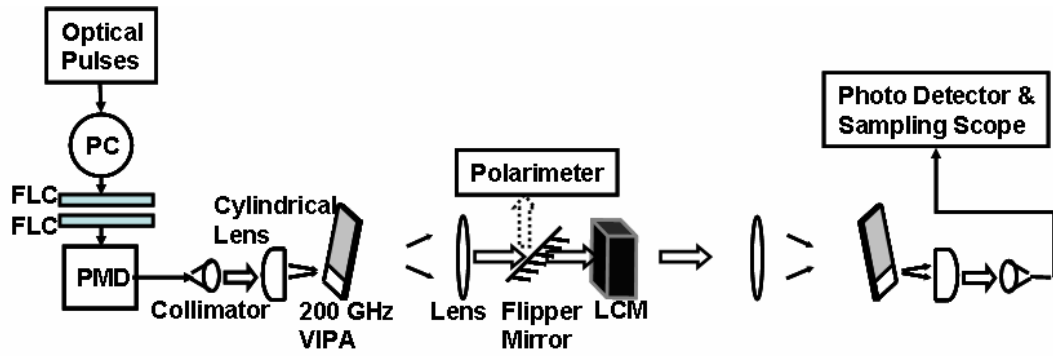


Fig. 5.1 Experimental setup for PMD compensation via a VIPA based pulse shaper. PC: polarization controller; FLC: ferroelectric liquid crystal; VIPA: virtually imaged phased-array; LCM: liquid crystal modulator. The polarimeter consists of a pair of FLC retarders, a polarizer and a 256-pixel linear InGaAs detector array. The block arrows indicate the direction of the signal flow.

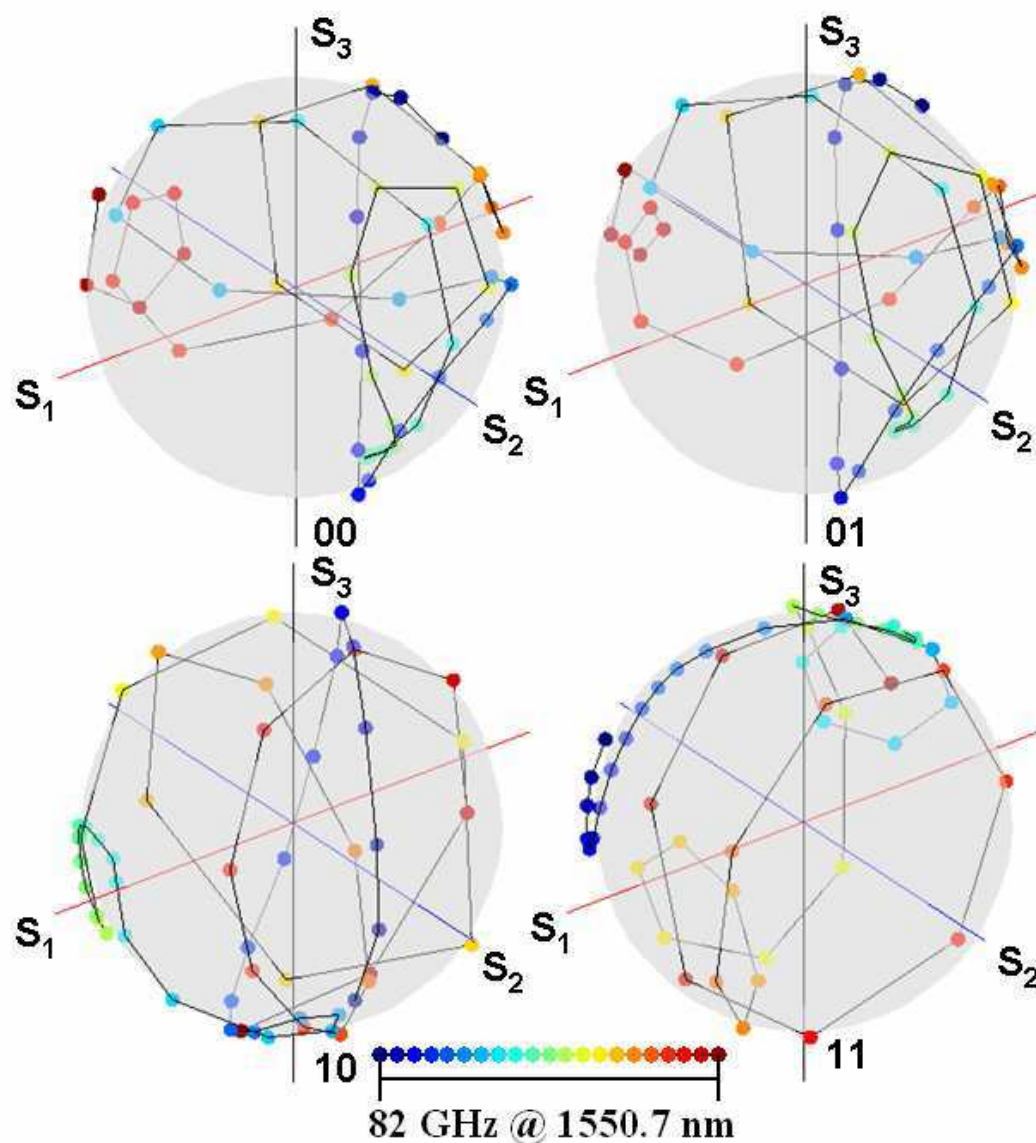


Fig. 5.2 Output SOP spectra corresponding to the 4 FLC states: 00, 01, 10, 11. Each point corresponds to a measured SOP vector at a specified pixel of the detector array (corresponding to a wavelength component).

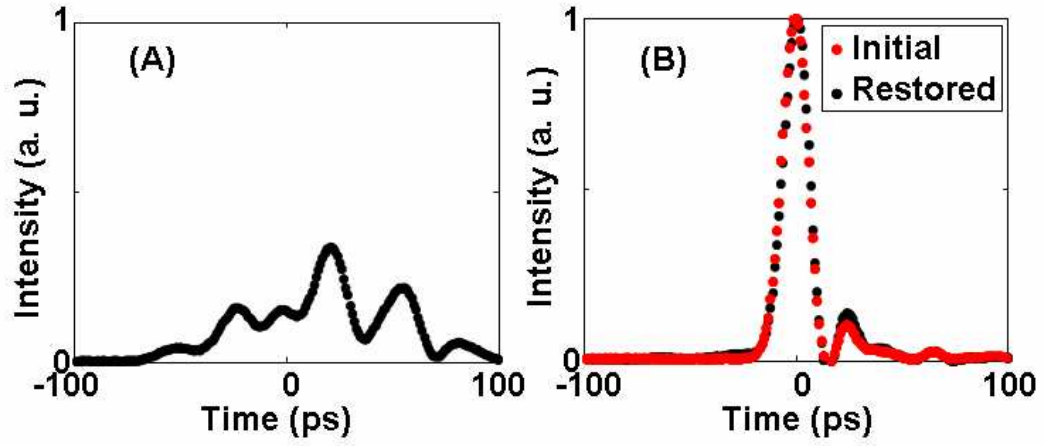


Fig. 5.3 PMD compensation results. (A) Distorted pulse; (B) restored and initial pulses.

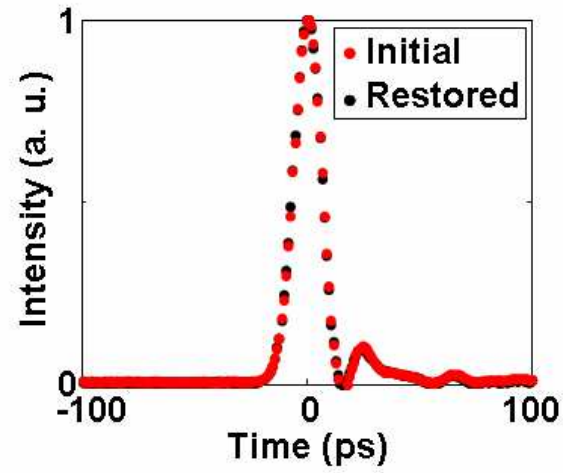


Fig. 5.4 PMD compensation result with 10-11 FLC states selected.

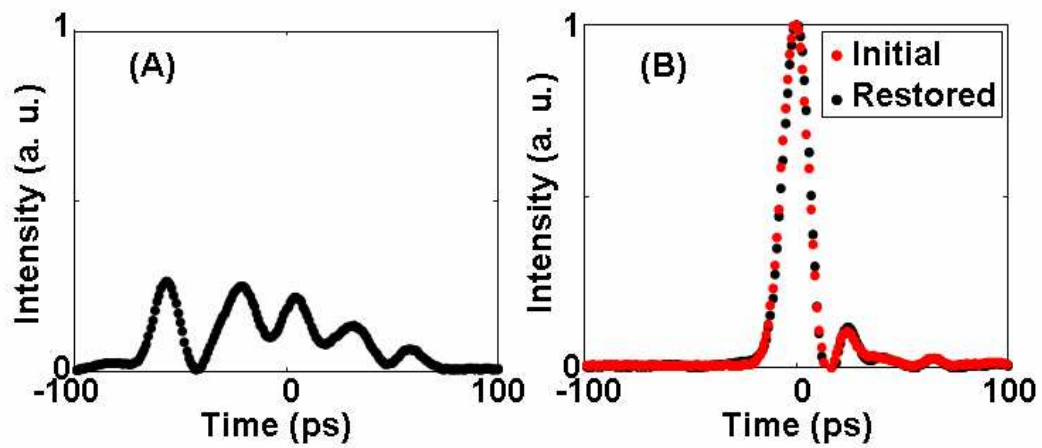


Fig. 5.5 Distorted (A) and restored pulses (B).

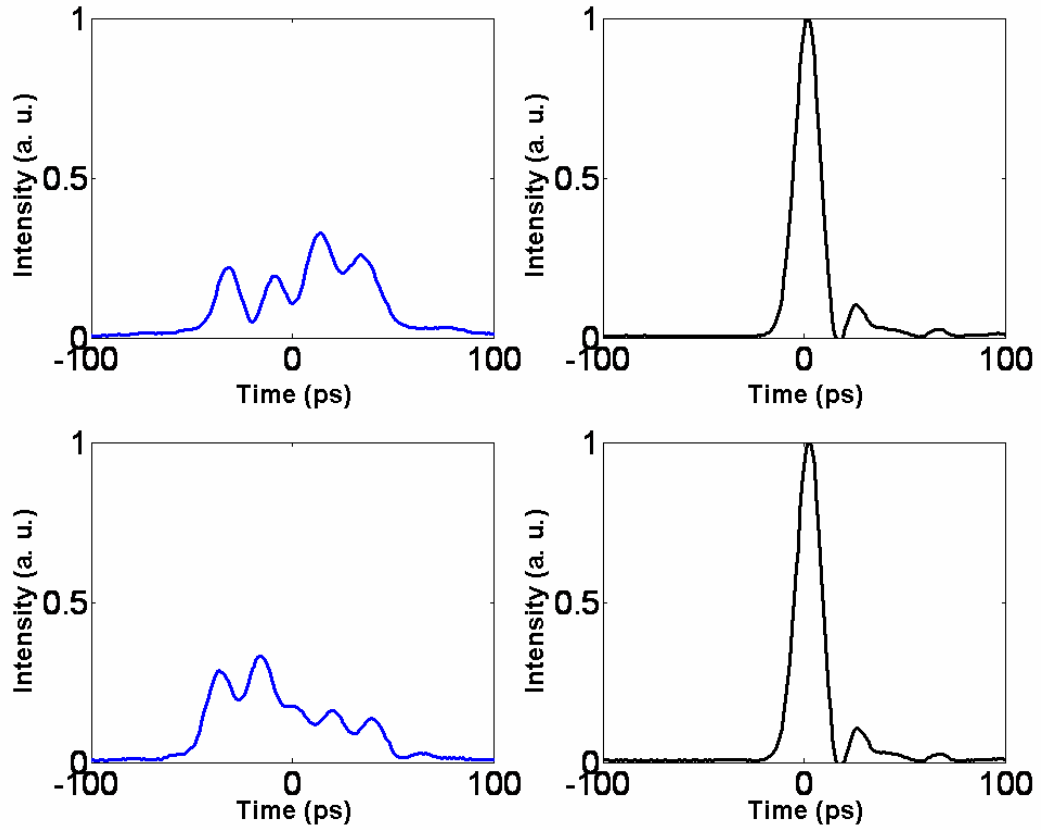


Fig. 5.6 Left Column: distorted pulses. Right column: Restored pulses after PMD compensation.

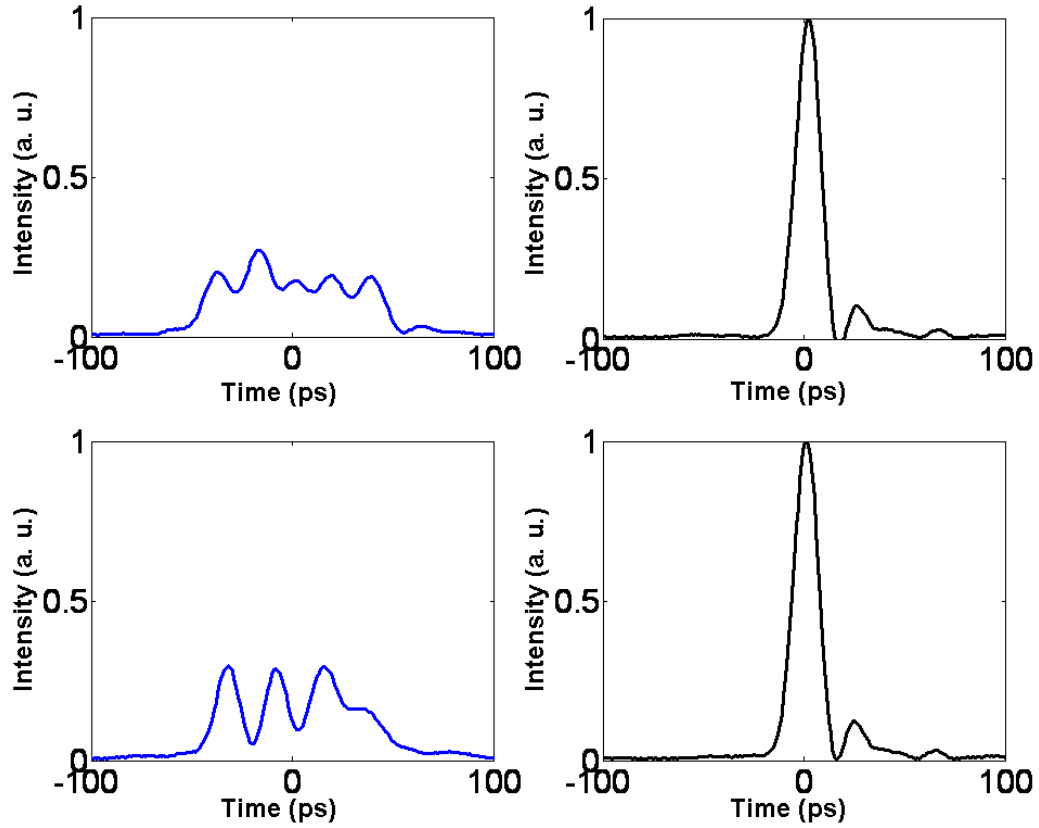


Fig. 5.7 Left Column: distorted pulses. Right column: Restored pulses after PMD compensation.

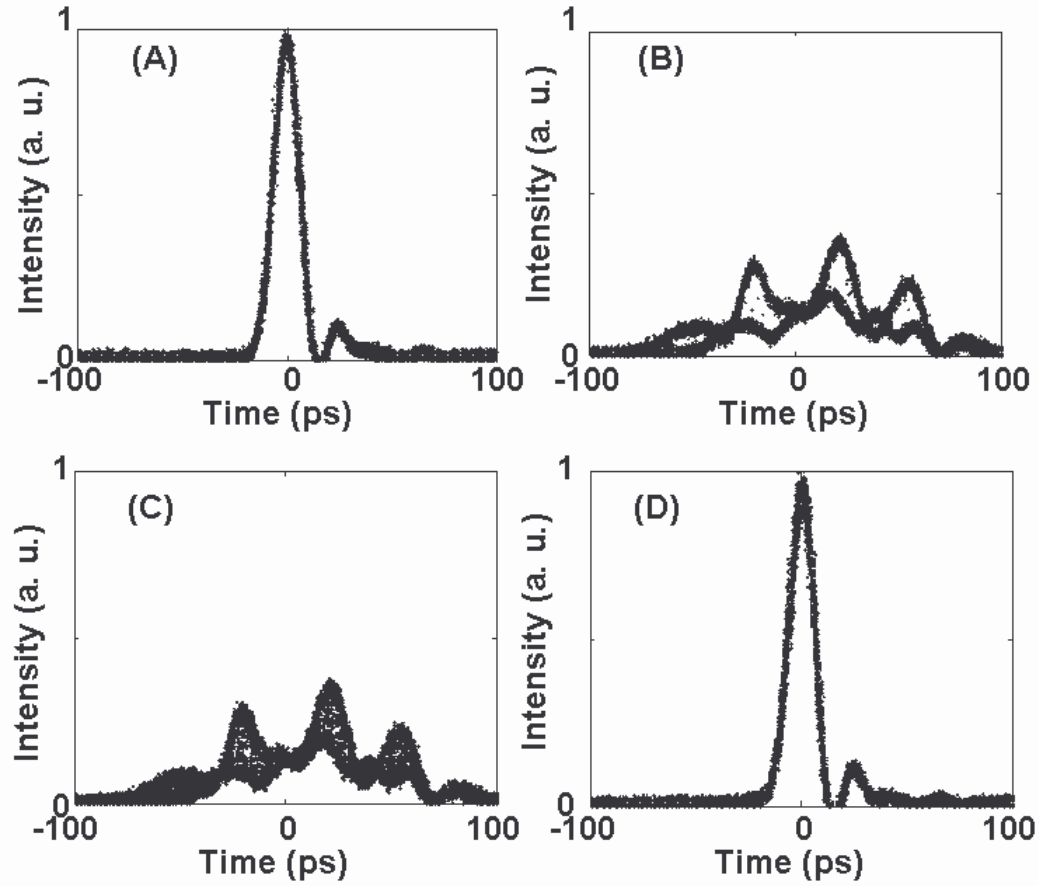


Fig. 5.8 Persistent traces of the initial pulse (A), PMD distorted pulse with the FLC retarders switching at a rate of 20 Hz (B), distorted pulse with the FLC retarders switching at 2 kHz (C) and the restored pulse with the FLC retarders switching at 2 kHz (D).

6. SUMMARY AND FUTURE DIRECTIONS

In this Ph. D. thesis work, my main contribution is that I proposed the concept of all-order PMD compensation via wavelength-parallel Jones matrix sensing and correction, and experimentally demonstrated the idea by applying wavelength-parallel polarimetry and pulse shaping techniques. My personal suggestions for the future directions are as follows:

- Since PMD is a key factor limiting the upgrade of current optical communication systems, to apply the proposed PMD compensation technique to lightwave system experiments is of particular interest. My experiments are all based on compensation of optical pulses from a mode locked fiber ring laser with 50 MHz repetition rate. My colleague, L. Xu, is currently working in this direction.
- Since multiple FSRs overlap in space in a VIPA based pulse shaper configuration, the experimental setup with 200 GHz VIPAs is only suitable for PMD compensation of two 40 Gb/s WDM channels with 100 GHz channel spacing or for one 100 Gb/s channel with 200 GHz channel spacing. In the future, wideband PMD compensation of tens of WDM channels may be possible in a single apparatus by using new pulse shaper geometries based on spectral dispersion in two dimensions. Such two dimensional spectral dispersion has been demonstrated using a combined grating-VIPA arrangement, which allows simultaneous realization of broad spectral coverage and high spectral resolution. And one of my colleagues is currently working on 2-D pulse shaping. The biggest challenge is that there is still no such 4-layer 2-D LCM available.

LIST OF REFERENCES

LIST OF REFERENCES

- [1] I.P. Kaminow, and T.L.Koch, *Optical Fiber Telecommunications IIIA*, Academic Press, 1997.
- [2] H. Kogelnik, R.M. Jopson, L.E. Nelson, “Polarization Mode Dispersion” in *Optical Fiber Telecommunications IVB-Systems and Impairments*, I.P. Kaminow and T.Li, ed., Academic Press, 2002.
- [3] G.J. Foschini, and C.D. Poole, “Statistical Theory of Polarization Dispersion in Single Mode Fibers”, *Journal of Lightwave Technology*, vol. 9, pp. 1439-1455, 1991.
- [4] C.D. Poole, and R.E. Wagner, “Phenomenological Approach to Polarisation Dispersion in Long Single-Mode Fibers”, *Electronics Letters*, vol. 22, pp. 1029-1030, 1986.
- [5] J. P. Gordon, and H. Kogelnik, “PMD Fundamentals: Polarization Mode Dispersion in optical fibers”, *Proceedings of the National Academy of Sciences*, vol. 97, pp. 4541-4550, 2000.
- [6] H. Bülow, “System Outage Probability Due to First- and Second-Order PMD”, *IEEE Photonics Technology Letters*, vol. 10, pp. 696-698, 1998.
- [7] P. Ciprut, B. Gisin, N. Gisin, R. Pass, J.P. Von der Weid, F. Prieto, and C.W. Zimmer, “Second-Order Polarization Mode Dispersion: Impact on Analog and Digital Transmissions”, *Journal of Lightwave Technology*, vol. 16, pp. 757-771, 1998.
- [8] H. Taga, M. Suzuki, and Y. Namihira, “Polarization mode dispersion tolerance of 10Gbit/s NRZ and RZ optical signals”, *Electronics Letters*, vol. 34, pp. 2098-2100, 1998.
- [9] A. E. Willner, “PMD in Optical Communication Systems”, Invited talk, presented at *LEOS Summer Topical Meetings*, Session MB1.1, 2003.
- [10] C. Xie, “Comparison of PMD Sensitivity for Different Modulation Formats”, Invited talk, presented at *LEOS Summer Topical Meetings*, Session MB2.3, 2003.

- [11] B. L. Heffner, "Automated Measurement of Polarization Mode Dispersion Using Jones Matrix Eigenanalysis", *IEEE Photonics Technology Letters*, vol. 4, pp. 1066-1069, 1992.
- [12] B. L. Heffner, "Accurate, Automated Measurement of Differential Group Delay Dispersion and Principal State Variation Using Jones Matrix Eigenanalysis", *IEEE Photonics Technology Letters*, vol. 5, pp. 814-1817, 1992.
- [13] R.M. Jopson, L.E. Nelson, and H. Kogelnik, "Measurement of Second-Order Polarization-Mode Dispersion Vectors in Optical Fibers", *IEEE Photonics Technology Letters*, vol.11, pp. 1153-1155, 1999.
- [14] H. Kogelnik, L.E. Nelson, and J.P. Gordon, "Emulation and Inversion of Polarization Mode Dispersion", *Journal of Lightwave Technology*, vol. 21, pp. 482-495, 2003.
- [15] P. B. Phua, H. A. Haus and E. P. Ippen, "All-frequency PMD compensator in feedforward scheme," *Journal of Lightwave Technology*, vol. 22, pp. 1280-1289, 2004
- [16] M. Akbulut, A. M. Weiner, P. J. Miller, "Wideband all-order polarization mode dispersion compensation via pulse shaping," *Optics Letters*, vol. 30, pp. 2691-2693, 2005.
- [17] M. Akbulut, A. M. Weiner and P. J. Miller, "Broadband All-Order Polarization Mode Dispersion Compensation Using Liquid-Crystal Modulator Arrays," *Journal of Lightwave Technology*, vol. 24, pp. 251-261, 2006.
- [18] A. M. Weiner, "Femtosecond pulse shaping using spatial light modulators", *Review of Scientific Instruments*, vol. 71, pp. 1929-1960, 2000.
- [19] S. X. Wang and A. M. Weiner, "A complete spectral polarimeter design for lightwave communication systems," *Journal of Lightwave Technology*, vol. 24, pp. 3982-3991, 2006.
- [20] M. Akbulut, A. M. Weiner, P. Cronin, P. J. Miller, "Broadband polarization correction with programmable liquid-crystal modulator arrays," *Optics Letters*, vol. 29, pp. 1129-1131, 2004.
- [21] R. Trebino, *Frequency-resolved optical gating: the measurement of ultrashort laser pulses*, Kluwer Academic Publishers, 2000.

- [22] R. Trebino and D. J. Kane, "Using phase retrieval to measure the intensity and phase of ultrashort pulses: frequency-resolved optical gating," *Journal of the Optical Society of America A*, vol. 10, pp. 1101-1111, 1993.
- [23] K. W. DeLong, D. N. Fittinghoff and R. Trebino, "Practical issues in ultrashort-laser-pulse measurement using frequency resolved optical gating," *IEEE Journal of Quantum Electronics*, vol. 32, pp. 1253-1264, 1996.
- [24] J. N. Sweetser, D. N. Fittinghoff and R. Trebino, "Transient-grating frequency-resolved optical gating," *Optics Letters*, vol. 22, pp. 519-521, 1997.
- [25] H. Miao, A. M. Weiner, L. Mirkin and P. J. Miller, "Broadband all-order polarization mode dispersion compensation via wavelength-by-wavelength Jones matrices correction," *Optics Letters*, vol. 32, pp. 2360-2362, 2007.
- [26] M. Shirasaki, "Large angular dispersion by a virtually imaged phased array and its application to a wavelength demultiplexer," *Optics Letters*, vol. 21, pp. 366-368, 1996.
- [27] G.-H. Lee, S. Xiao and A. M. Weiner, "Optical dispersion compensator with >4000-ps/nm tuning range using a virtually imaged phased array (VIPA) and spatial light modulator (SLM)," *IEEE Photonics Technology Letters*, vol. 18, pp. 1819-1821, 2006.
- [28] H. Miao, A. M. Weiner, L. Mirkin and P. J. Miller, "All-Order Polarization Mode Dispersion Compensation (PMD) via Virtually Imaged Phased-Array (VIPA) Based Pulse Shaper," to appear in *IEEE Photonics Technology Letters*.
- [29] R.C. Jones, "A new Calculus for the Treatment of Optical Systems, VI. Experimental Determination of the Matrix", *Journal of the Optical Society of America*, vol. 31, pp. 110-112, 1947.
- [30] W.A. Shurcliff, "Modern Description of Polarized Light" in *Polarized Light, Production and Use*, Harvard University Press, 1996.
- [31] Agilent Technologies 8509-1 Application note, <http://cp.literature.agilent.com/litweb/pdf/5091-2879E.pdf>, Internet link, 2005.
- [32] M. Duelk and P. Winzer, "Polarization mode dispersion aspects for parallel and serial PHY," *IEEE 802. 3 High Speed Study Group*, Nov. 2006

- [33] M. Akbulut, "Broadband all order polarization mode dispersion compensation using liquid-crystal modulator arrays," Ph. D. thesis, Department of Electrical and Computer Engineering, Purdue University, 2005.
- [34] R.D. Nelson, D.E. Leaird, and A.M. Weiner, "Programmable polarization-independent spectral phase compensation and pulse shaping", *Optics Express*, vol. 11, pp.1763-1769, 2003.
- [35] C. Iaconis and I. A. Walmsley, "Self-referencing spectral interferometry for measuring ultrashort optical pulses," *IEEE Journal of Quantum Electronics*, vol. 35, pp. 501-509, 1999.
- [36] P. Baum and E. Riedle, "Design and calibration of zero-additional-phase SPIDER," *Journal of the Optical Society of America B*, vol. 22, pp. 1875-1883, 2005
- [37] E. M. Kosik, A. S. Radunsky, I. A. Walmsley and C. Dorrer, "Interferometric technique for measuring broadband ultrashort pulses at the sampling limit," *Optics Letters*, vol. 30, pp. 326-328, 2005.
- [38] A. S. Wyatt, I. A. Walmsley, G. Stibenz and G. Steinmeyer, "Sub-10 fs pulse characterization using spatially encoded arrangement for spectral phase interferometry for direct electric field reconstruction," *Optics Letters*, vol. 31, pp. 1914-1916, 2006.
- [39] J. R. Birge, I. Ell and F. X. Kartner, "Two-dimensional spectral shearing interferometry for few-cycle pulse characterization," *Optics Letters*, vol. 31, pp. 2063-2065, 2006.
- [40] S. Yang, A. M. Weiner, K. R. Parameswaran and M. M. Fejer, "Ultrasensitive second-harmonic generation frequency-resolved optical gating by aperiodically poled LiNbO₃ waveguides at 1.5 μm ", *Optics Letters*, vol. 30, pp. 2164-2166, 2005.
- [41] H. Miao, A. M. Weiner, S. Yang, C. Langrock, R. V. Roussev, M. M. Fejer, "Ultrasensitive Second-Harmonic Generation Frequency-Resolved Optical Gating Using a Fiber-Pigtailed Aperiodically Poled Lithium Niobate Waveguide at 1.55 μm ," presented at the *15th International Conference on Ultrafast Phenomena*, WC2, August, 2006.

- [42] H. Miao, S. Yang, C. Langrock, R. V. Roussev, M. M. Fejer and A. M. Weiner, "Ultra-low-Power Second-Harmonic Generation Frequency-Resolved Optical Gating Using Aperiodically Poled Lithium Niobate Waveguides (Invited)," to appear in *Journal of the Optical Society of America B*.
- [43] S. -D. Yang, H. Miao, Z. Jiang, A. M. Weiner, K. R. Parameswaran and M. M. Fejer, "Ultrasensitive nonlinear measurements of femtosecond pulses in the telecommunications band by aperiodically poled LiNbO₃ waveguides," *Applied Optics*, vol. 46, pp. 6759-6769, 2007.
- [44] H. Miao, A. M. Weiner, C. Langrock, R. V. Roussev, M. M. Fejer, "Sensing and compensation of femtosecond waveform distortion induced by all-order polarization mode dispersion at selected polarization states," *Optics Letters*, vol. 32, pp 424-426, 2007.
- [45] H. Miao, A. M. Weiner, C. Langrock, R. V. Roussev, M. M. Fejer, "Polarization insensitive ultralow-power second-harmonic generation frequency-resolved optical gating," *Optics Letters*, vol. 32, pp. 874-876, 2007.
- [46] M. M. Fejer, G. A. Magel, D. H. Jundt and R. L. Byer, "Quasi-phase-matched second harmonic generation: tuning and tolerances," *IEEE Journal of Quantum Electronics*, vol. 28, pp. 2631 – 2654, 1992.
- [47] G. D. Miller, R. G. Batchko, W. M. Tulloch, D. R. Weise, M. M. Fejer and R. L. Byer, "42%-efficient single-pass CW second-harmonic generation in periodically poled lithium niobate," *Optics Letters*, vol. 22, pp. 1834-1836, 1997.
- [48] J. Huang, X. P. Xie, C. Langrock, R. V. Roussev, D. S. Hum and M. M. Fejer, "Amplitude modulation and apodization of quasi-phase-matched interactions," *Optics Letters*, vol. 31, pp. 604-606, 2006.